Master Thesis

Detecting irrigation of potato parcels in the Northern Netherlands using remotely sensed SAR images

Roel Marijn Vos

Student number: 4391489
E-mail address: roelmarijn@gmail.com

Delft University of Technology
Department of Applied Mathematics

Thesis committee:

Prof. dr. ir. Arnold Heemink,	TU Delft, supervisor
Dr. ir. Jakob Söhl,	TU Delft
Frederike de Visser-Bleijenberg, MSc.,	Witteveen+Bos, supervisor

April, 2022

Preface

This thesis project combines four different fields of research: plant growth modelling, crop cultivation practices, remote (SAR) sensing, and mathematics. I had some basis in remote sensing and I enjoyed a great education in mathematics. Furthermore, plant growth modelling is closely related to my background in modelling in general. However, the practice of crop cultivation practices was a new and interesting subject for me. My thesis project has given me the challenging opportunity to learn about and combine all four aspects. My supervisors, Frederike de Visser-Bleijenberg and prof. Arnold Heemink, each had an expertise in one or two of the four subjects. They dived deeply into the part of my thesis that coincides with their area of expertise, identifying weaknesses and points of improvement in that aspect. Their encouragement has helped me to take each aspect of this project to the next level. At the same time, juggling these different demands has occasionally been quite a challenge. Nevertheless, I am quite proud of the final result.

In this thesis, I developed a model for RVI evolution during the growth season of a crop. As far as I could tell, this model has no similar precedent in literature. I believe that this model and the corresponding calibration methodology are the main contributions of this thesis to science. Yet, I am also quite proud of the more practical contributions. Firstly, in the very last phase of my project, I put exceptional effort into explaining different clusterings of parcels in terms of RVI behaviour and possible real-world causes. This was quite challenging as this dipped mostly into the field of crop cultivation that I was least familiar with. Secondly, I believe the code base I developed during the project is well-structured and straightforward to use and maintain. This should make it easy for successors working on this project to continue where I left off.

Yet none of this would have been possible without the many people that supported me during the process. Firstly, I would like to thank Witteveen+Bos for giving me the opportunity to work on this project in the first place. I would like to thank my supervisor from Witteveen+Bos Frederike for taking the time to meet with me twice a week. These meetings were a good moment to look at the bigger picture, preventing me from diving too deeply into side-tracks. In addition, she gave useful guidance on my weak area of crop cultivation and pushed me in the right direction when I could no longer see a way forward. I would also like to thank the colleagues from my little team at Witteveen+Bos Léon, Elke, Wesley, Zelda, and of course Fredrike for making my time there enjoyable. Next, I would like to thank prof. Arnold Heemink for supervising the project and his useful tips on my thesis report. I would also like to thank my friends Rutger, Olav, Joris, Weronika, and Eva for keeping me company on many long thesis days at the university. Rutger in particular made many days enjoyable and has been a great partner for many in-depth discussions and brainstorms. Lastly, I would like to thank my family and my mother in particular for providing some input on the ways of scientific research, and for reading a large part of my thesis.

Abstract

As a response to the dry summer of 2018, Witteveen+Bos developed a model for water demand prediction to improve insight into water demands. Validation by water board "Hunze en Aas" has revealed the predictive power of the irrigation model to be very limited. For this thesis project, we developed a methodology for the detection of irrigation of crop parcels based on the radar vegetation index (RVI) derived from remote SAR images. This methodology can be used to improve the existing irrigation model.

To achieve this, we developed a novel model to describe the evolution of a vegetation index (such as RVI) during the growth season. Unlike existing models, the model presented in this thesis includes the effect of precipitation deficit, both as a temporary inhibitor of a vegetation index, and as a long-term influence on the crop growth. The model is non-linear in many of its model parameters. Therefore, heuristic calibration methods are unavoidable. We show that the standard calibration methods non-linear least squares and differential evolution are outperformed by a hybrid of both methods that we specifically designed for this application.

After calibrating the model to time series of 1167 potato parcels in the north-east of the Netherlands, we investigate different ways to cluster the model parameters. We propose explanations for three important clusterings through their RVI time series (speculative) environmental factors. Comparison with information on irrigated parcels for the years 2018-2020 reveals a statistically significant correlation between some of the clusters and irrigation. However, the variation in irrigation rate never exceeded a factor two. Therefore, no accurate classifier can be built based on these clusters.

We recommend two important ways to improve the current implementation. Firstly, the baseline RVI is consistently overestimated, resulting in mostly negative normalized RVI. Because of this, the model cannot properly describe precipitation deficit-driven fluctuations in the RVI. These fluctuations are an important part of system behaviour, so improving the estimation of the baseline RVI should be the first priority for future research.

Secondly, the exact irrigation dates of a set of parcels will be very useful. Comparing these dates to the corresponding RVI time series will make it possible to uncover features of the RVI evolution that are indicators of irrigation. The model parameterization can then be tuned to optimize sensitivity to these features.

Contents

Nomenclature **v**

1 Introduction and background **1**
1.1 Water boards and the watervraagprognosetool 1
1.2 Irrigation model of the Landelijk Hydrologisch Model (LHM) 1
1.3 Basisregistratie Gewaspercelen (BRP) 2
1.4 Predictive power of the irrigation model 3
1.5 Crop monitoring with remote sensing 3
1.6 Research questions 4
1.7 Reader's guide 4

2 Generating radar vegetation index (RVI) time series using Sentinel-1 SAR images **5**
2.1 Raw SAR data 5
  2.1.1 SAR imaging technology 5
  2.1.2 Sentinel-1 GRD images 6
2.2 SAR image preprocessing 7
  2.2.1 Orbit calibration 7
  2.2.2 Border noise removal 7
  2.2.3 Thermal noise removal 8
  2.2.4 Radiometric calibration 8
  2.2.5 Geometric correction 8
  2.2.6 Speckle filtering 9
2.3 Selecting image pixels within a parcel 9
  2.3.1 Raster ray tracing algorithm 9
  2.3.2 Validating geolocation and pixel selection 10
2.4 Radar vegetation index (RVI) 11
2.5 Validation data 12
2.6 Single image irrigation detection 13
2.7 Generating RVI time series 14

3 Mathematical modelling of vegetation indices during the growth phase **16**
3.1 Plant growth model 16
3.2 Mapping growth stage to vegetation index 17
3.3 Simplifications and model parameterizations 20

4 Calibration methods for the vegetation index model **23**
4.1 Formulation of the optimization problem 23
4.2 Non-linear least squares 24
  4.2.1 Algorithm 24
  4.2.2 Limitations and use case 25
4.3 Differential evolution 25
  4.3.1 Algorithm 25
  4.3.2 Parameter choices and use case 26
4.4 The hybrid method 27
  4.4.1 Algorithm 27
  4.4.2 Parameter configuration 28

5 Validation and optimization of the calibration methodology **29**
5.1 Comparison between calibration methods 29
5.2 Consistency of the hybrid calibration method 32
5.3 Validating the parameter configuration of the hybrid method 34

6 Assessing to what extend model features reflect the behaviour of the RVI 38
6.1 Average behaviour all parcels . . . 38
6.2 Comparison between model parameterizations . . . 40

7 Clustering parcels 43
7.1 Clusters based on C_1^{crop} and C_3^{crop} . . . 43
7.2 Clusters based on h_{min}^{crop} . . . 46
7.3 Clusters based on $t_0^{parcel} + \Delta t_1^{crop}$ and C_2^{crop} . . . 48

8 Discussion 55
8.1 Behaviour of RVI during the growth season . . . 55
  8.1.1 Correlation with rain deficit . . . 55
  8.1.2 Lack of growth of the RVI . . . 56
  8.1.3 Correlation with irrigation data . . . 57
8.2 Calibration . . . 58
  8.2.1 Two-phase model parameterizations . . . 58
  8.2.2 Quadratic model parameterization . . . 59
8.3 The vegetation index model . . . 60
  8.3.1 Normalization of RVI . . . 60
  8.3.2 Modelling growth of RVI . . . 61
  8.3.3 Scatter modifier h^{crop} . . . 61
  8.3.4 End of growth season Δt_2^{crop} . . . 62
8.4 Parcel clustering . . . 62
  8.4.1 Correlation with irrigation data . . . 62
  8.4.2 Employment in the watervraagprognosetool . . . 63

9 Conclusion 65

References 66

Appendices 70

A Additional figures for model and calibration method validation 70
A.1 Method comparison for the basic fit functions . . . 70
A.2 Hybrid parameter configuration validation . . . 72
A.3 Comparison between fit functions . . . 75

B Additional time series 77
B.1 Time series of potato parcels separated by irrigation . . . 77
B.2 Average time series of corn parcels . . . 79

C Additional clustering investigations 81
C.1 Analysis of clusters based on C_1^{crop} and C_3^{crop} in 2019 and 2021 . . . 81
  C.1.1 2019 . . . 81
  C.1.2 2021 . . . 83
C.2 clusters based on $t_0^{parcel} + \Delta t_1^{crop}$ and C_2^{crop} in 2018 and 2021 . . . 85
C.3 Parameters with less meaningful clusters . . . 86

Nomenclature

Abbreviations

RVI	Radar vegetation index. See section 2.4.
SAR	Synthetic-aperture radar. Imaging technique used to create the remote sensing image used in this thesis.
BRP	Basisregistratie Gewaspercelen. See section 1.3
VV and VH	Vertically transmitted Vertically received and Vertically transmitted Horizontally received. The two polarisations in a Sentinel-1 SAR image.
GRD image	Ground Range Detected image. The preprocessed Sentinel-1 product that was used in this project, see section 2.1.2.
S1A and S1B	Sentinel-1A and Sentinel-1B. The two satellites that acquire the SAR images used in this project.
asc and dsc	Ascending and descending orbit.
Linear (model)	Model with g and p^{crop} linear.
Bilinear (model)	Model with g linear and p^{crop} bilinear.
Exponential (model)	Model with g linear and p^{crop} exponential.
Quadratic (model)	Model with g quadratic and p^{crop} linear.
nllsq	The non-linear least squares calibration algorithm.
difev	The differential evolution calibration algorithm.
Q1, Q2, Q3	The three research questions of this thesis project, see section 1.6.

Symbols related to the model

C_1^{crop}	days^{-1}	Model parameter. Can be interpreted as the growth constant of the first (and in some models only) phase.
C_2^{crop}	days^{-1}	Model parameter. Can be interpreted as the growth constant of the second (and in some models only) phase.
C_3^{crop}	mm	Model parameter. Determines the slope of precipitation deficit dependent growth inhibitor $i_g^{crop}(rd)$.
C_4	-	Constant defining the linear mapping $g(p^{crop})$.
C_4^{crop}	-	Model parameter in the exponential model. Multiplication of C_4 and the growth constant C_1^{crop}.
C_5 and C_6	-	Constants defining respectively the quadratic and linear parts of the quadratic mapping $g(p^{crop})$.
C_5^{crop}	days^{-2}	Model parameter in the quadratic model, defined as $C_5^{crop} = C_5(C_1^{crop})^2$.
C_6^{crop}	days^{-2}	Model parameter in the quadratic model, defined as $C_6^{crop} = (C_6 C_1^{crop})^2$.
CC	-	Canopy cover in leaf area per unit ground area.
CC_t	-	Canopy cover at the start of the leave senescence phase.
$g(p)$		Mapping $g : \mathbb{R} \to \mathbb{R}$ that maps crop abundance p to influence on vegetation index $v_i - v_0$ in the absence of precipitation deficit.
$i_g^{crop}(rd)$	-	Growth inhibitor as a result of precipitation deficit. $i_g^{crop}(rd) \in [0, 1]$

$h^{crop}(rd)$	-	Rain deficit dependent factor in $[h^{crop}_{min}, 1]$ that reduces the estimate of $v_i - v_0$ by accounting for temporary influences such as crop water saturation.
$h_g^{crop}(p, rd)$		Mapping of the crop abundance p to influence on vegetation index $v_i - v_0$ accounting for temporary influences such as crop water saturation.
h^{crop}_{min}	-	Model parameter. Minimum value of the rain deficit-dependent scaling factor $h^{crop}(rd)$. $h^{crop}_{min} \in [0, 1]$.
$p^{crop}(t)$	-	Measure for vegetation abundance that can be interpreted as ”SAR-responsivity” of the vegetation.
p_0^{crop}	-	Constant defined by the exponential growth phase in the model for plant growth. Can be interpreted as the initial crop abundance at the start of the growth season t_0^{crop}.
$p_{g,0}^{crop}$	days^{-1}	Model parameter in the exponential model. Multiplication of the ”initial crop abundance” $p_0^{crop}(t)$ and the growth constant C_1^{crop}.
$rd(t)$	mm	The cumulative precipitation deficit (rain deficit). Defined with a 6-day memory in this project.
rd^{crop}_{max}	mm	Model parameter. The maximum rain deficit at which the crop experience no hinder in growth.
$s^{parcel}(t)$	days^{-1}	The predicted derivative crop abundance p^{crop} when $rd = 0$. In the full model, $s^{parcel}(t) = C_1^{crop} p^{crop}(t)$ in the first phase and $s^{parcel}(t) = C_2^{crop}$ in the second phase.
t_0^{crop}	days	Model parameter. Signifies the start of the growth season.
t_1^{parcel}	days	Parcel-dependent start of the second growth phase.
t_2^{crop}	days	End of the growth season or time of harvest.
Δt_1^{parcel}	days	Model parameter. Number of days between the start of the growth season t_0^{parcel} and the start of the second phase t_1^{parcel}.
Δt_2^{crop}	days	Model parameter. Number of days between the start t_0^{crop} and the end t_2^{crop} of the growth season.
t_i	days	Time of the vegetation index measurement v_i ($i \in \{1, 2, .., n\}$).
$t_{i,k}$	days	Times between t_{i-1} and t_i at which there is a measurement of the rain deficit, $k \in \{0, 1, ..., n_i\}$. By definition, $t_{i,n_i+1} = t_i$ and $t_{i,-1} = t_{i-1}$.
t_{b1}	days	Time of the vegetation index measurement v_{b1}.
v_0	-	Vegetation index for a given parcel in the absence of vegetation. In this thesis, it is estimated for each orbit separately by averaging the first three measurements.
v_i	-	Vegetation index measurement of a parcel at time t_i ($i \in \{1, 2, .., n\}$). In principle, any vegetation index could be used, but the RVI is used in this project.
v_{b1}	days	Observation before the first observation of the time series v_1, i.e. the last of the three observations used in the calculation of v_0.
ζ_i^{crop}	-	Random variable accounting for measurements uncertainties in v_i.
$\zeta_i^{'crop}$	-	Random variable accounting for uncertainties $v_i - v_0$, combining both measurements uncertainties and integrated uncertainty in growth.
$\xi^{crop}(t)$	days^{-1}	Random variable encompassing uncertainties in crop growth.
σ_ζ^{crop}	-	Standard deviation in ζ_i^{crop}.
σ_ξ^{crop}	m^{-2}	Standard deviation in $\int_{t_{i-1}}^{t_i} \xi^{crop}(t)dt$.
σ^0_{VV}	m^{-2}	Backscatter of the VV polarisation.
σ^0_{VH}	m^{-2}	Backscatter of the VH polarisation.

Symbols related to the calibration

$\mathbf{C}$	-	Vector of length M containing the model parameters.
$\mathbf{C^0}$	-	Initial guess of the optimum $\mathbf{C}$ in the non-linear least squares algorithm.
C_j	-	Element j of $\mathbf{C}$.
$\mathbf{C^k}$	-	Estimation of optimal $\mathbf{C}$ at iteration k of the non-linear least squares algorithm.
$\mathbf{C}_{opt}$	-	Optimal $\mathbf{C}$ that minimizes the error statistic $E(\mathbf{C})$.
$\mathbf{C}_{both}$	-	Collection of model parameters that are fitted by both the second step (differential evolution) and the third step (non-linear least squares) of the hybrid calibration method.
$\mathbf{C}_{difev}$	-	Collection of model parameters that are fitted by both the second step (differential evolution) but not the third step (non-linear least squares) of the hybrid calibration method.
$\mathbf{C}_{nllsq}$	-	Collection of model parameters that are fitted by the third step (non-linear least squares) but not the second step (differential evolution) of the hybrid calibration method.
CR	-	The recombination constant of the differential evolution algorithm, see section 4.3.2.
E	-	Linear least squares error statistic of a fit.
f	-	(Vectorized) fit function as defined in section 3.3.
F	-	The mutation constant of the differential evolution algorithm, see section 4.3.2.
$\mathbf{J}(\mathbf{C})$	-	$N \times M$ Jacobian Matrix of f in $\mathbf{C}$.
M	-	Number of model parameters.
M	-	Number of observations in $\mathbf{v}$.
$\mathbf{t}$	days	Vector containing the observation time of the observations in $\mathbf{v}$.
$\mathbf{t_{-1}}$	days	Vector containing the observation time of the previous observation.
$\mathbf{v}$	-	Vector the observations.
$\mathbf{v_{-1}}$	-	Vector containing the previous observation, i.e. $v_{-1,i} = v_{i-1}$.
$\nabla_{\mathbf{C}}$		Nabla operator with respect to $\mathbf{C}$

1 Introduction and background

1.1 Water boards and the watervraagprognosetool

Extreme weather conditions are occurring increasingly frequently and more intensely as a result of climate change. One of its manifestations is the increasing intensity of droughts, both in the Netherlands and elsewhere. These droughts hamper yields from agriculture and damage fragile nature reserves, leading to decreased biodiversity. Insight in water demands for its various applications can support educated prioritization of water supply and investments into infrastructure, minimizing the damage caused by droughts.

In the Netherlands, the surface water and groundwater levels are managed by 21 institutions called water boards ("waterschappen"). They need to make decisions on investments in infrastructure and prioritization of the various sources of water demand. To support this decision making, accurate estimates of the water demand for its diverse applications can be a huge benefit. Following the summer of 2018, several water boards engaged Witteveen+Bos to build a tool to predict water demand. This tool came to be called the "watervraagprognosetool".

1.2 Irrigation model of the Landelijk Hydrologisch Model (LHM)

In the watervraagprognosetool, water demand is split up into several categories, which are modelled separately. One of these categories is water demand by irrigation. The existing irrigation model estimates future water demands as a function of the predicted precipitation deficit. This model is defined as

$$wd_{est} = \begin{cases} c_4 & \text{for } rd_{30} \leq b_1 \\ c_2 rd_{30}^2 + c_1 rd_{30} + c_0 & \text{for } b_1 < rd_{30} \leq b_2 \\ c_5 & \text{for } rd_{30} > b_2, \end{cases} \tag{1.1}$$

where wd_{est} ($\mathrm{m^3s^{-1}}$) is the estimated water demand from irrigation per unit area of land, rd_{30} (mm) is the cumulative precipitation deficit over the past 30 days, and c_0 ($\mathrm{m^3s^{-1}}$), c_1 ($\mathrm{m^3mm^{-1}s^{-1}}$), c_2 ($\mathrm{m^3mm^{-2}s^{-1}}$), c_4 ($\mathrm{m^3mm^{-1}s^{-1}}$), c_5 ($\mathrm{m^3mm^{-1}s^{-1}}$), b_1 (mm) and b_2 (mm) ($b_1 < b_2$) are model parameters calibrated using data from the Landelijk Hydrologisch Model [1].

The accessibility to water supplies suitable for irrigation varies between areas, and so does the susceptibility to dehydration during dry periods. Therefore, the area of interest was divided into 23 regions according to their hydrological character. The model parameters have been estimated for each region separately. This division is shown in figure 1. As not all water boards participated, only part of the Netherlands is included in the area of interest.

The Landelijk Hydrologisch Model contains simulation-derived data from precipitation deficits and irrigation from the 101 year period between 1911 and 2011 [2]. This data was used to fit the parameters of the assumed model of equation (1.1). To this end, land use was divided into 10 categories. These categories can be roughly understood as different crop types. The model was calibrated separately for each of the 10 types of land use. Together with the 23 distinct regions, the land is split up into 230 distinct groups. The model is calibrated to each of these groups separately. Many of these calibrations were later improved upon with data from the water boards and Rijkswaterstaat [2].

The model of equation (1.1) does not take into account that not all parcels are irrigated. In reality, many parcels are not irrigated, for various (mostly economical) reasons. The Landelijk Hydrologisch Model provides an estimation of the percentage of area being irrigated for each of the 230 region and land use combinations [2]. The watervraagprognosetool combines this with recent land use data from the "Basisregistratie Gewaspercelen" (BRP) to obtain a present-day estimation for irrigated area [2]. The BRP is a source of data that will be described in the next section.

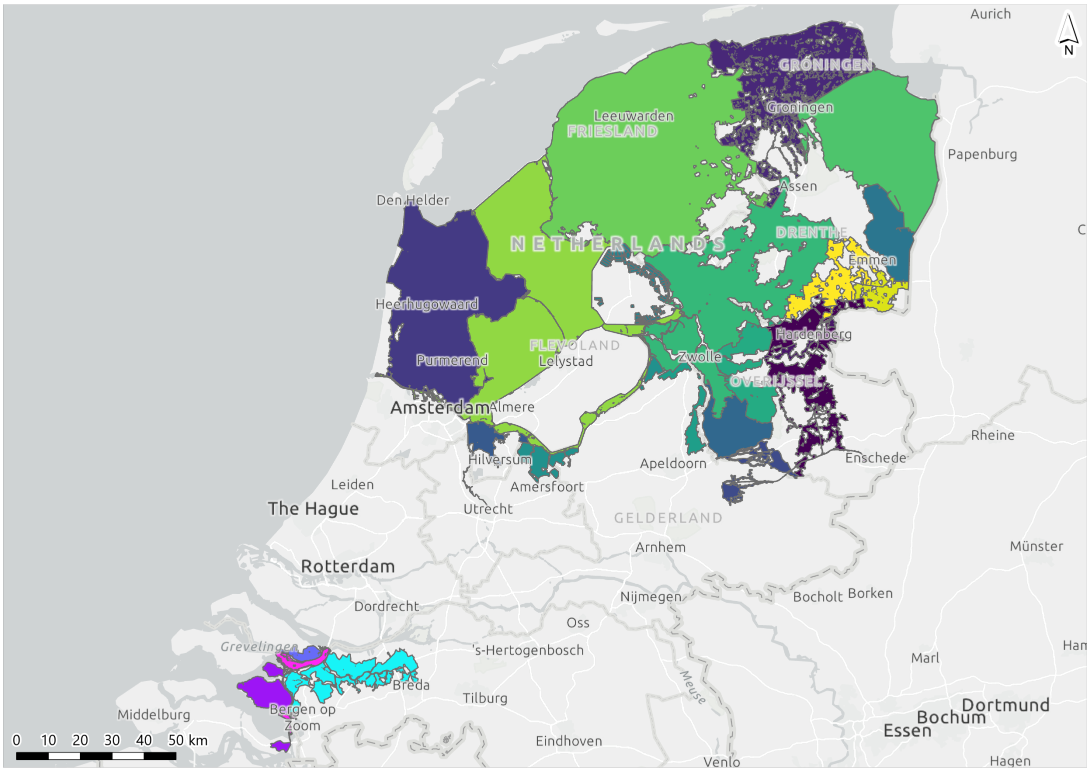

Figure 1: Area of interest, split up into 23 regions according to their hydrological character.

1.3 Basisregistratie Gewaspercelen (BRP)

The "Basisregistratie Gewaspercelen" (BRP) is a governement-managed data set containing information on the shape, location and usage of agricultural parcels in the Netherlands. Every crop field owner is required to record each parcel into the BRP, including, among other things, the crop being cultivated. Every year, on 15 May, a new data set is produced. As a result, a BRP data set is freely available for every year since 2009 [3].

In the current watervraagprognosetool, the BRP is only used for calculating the area of land utilized by different land use types in each region. During this project, the role of the BRP will become much more important. We will attempt to measure irrigation levels for each parcel separately using remote sensing images. Hence, the location and shape information from the BRP will be very important. In addition, different crops are expected to have a different backscatter behaviour, so the crop type recorded in the BRP will be required to categorize the parcels.

For the year 2019, there are a total of 259883 parcels with a centroid within the area of interest show in figure 1. Therefore, efficiency will be an important focus in the algorithms used in this project. For this thesis, we limit the parcels to only the two most common (other than grass) crop types: potatoes and corn. The frequency of these crop types is shown in table 1.

Table 1: The number of parcels and total area in the 2019 Basisregistratie Gewaspercelen (BRP) for the parcels within the area of interest.

crop type	# of parcels	total area (km^2)
All crops	259883	7234.3
Potatoes	19727	809.5
Corn	18507	568.1

1.4 Predictive power of the irrigation model

The watervraagprognosetool makes daily updates of its water demand estimates. Past precipitation deficits are obtained from precipitation and evaporation data imported from the KNMI. Weather forecasts from the ECMWF (European Centre for Medium-Range Weather Forecasts) are used to obtain estimations of the precipitation deficit 46 days into the future. Combining these, water demand by irrigation is estimated for both the past and 46 days into the future. [2]

The water board Hunze en Aas has collected irrigation data from field measurements and questionnaires and compared these with the results of the watervraagprognosetool. Unfortunately, this assessment has revealed that the predictive power of the irrigation model is rather low. Hence, Witteveen+Bos has been actively searching for methods to improve the tool. This thesis is a first step in that direction.

The lack of predictive power of the current irrigation model is likely due to limitations of the irrigation data in the Landelijk Hydrologisch Model (LHM). The LHM estimates irrigation through hydrological simulations [4]. These simulations make use of key figures (”kengetallen”) for irrigation that originate from an investigation by the Landbouw Economisch Instituut (LEI) [5]. These figures were based on actual irrigated area of the years 1995, 1997 and 1999, and can therefore be considered rather outdated. Even though the simulations of the LHM do take into account changing circumstances such as precipitation and greater availability of irrigation equipment [4], a certain margin for error is still to be expected. In addition, the LEI calculated key figures to estimate relative contributions of different crops based on a data set from 1997 that involved only 600 out of 90000 agricultural companies of significant size [5]. As such, the LEI warns that these key figures have very limited reliability [5].

Therefore, it is unlikely that significant improvements to the predictive power can be made using only the current sources of information. Even though more recent updates of the irrigation data produced by the LEI exists [6], the data only contains information on total irrigated area and water usage on the municipality scale over an entire growth season, and no distinction between crops is made. Therefore, utilizing this data in the watervraagprognosetool would require hydrological simulations similar to the ones performed in the LHM. Even then, it is quite uncertain this would improve predictive power, mostly due to the low spatial and temporal resolution of the data.

Instead, to improve upon the current methodology, it was proposed to integrate estimates of irrigation levels from remote sensing images. Irrigation behaviour can be assumed to have some degree of temporal correlation; if a field is irrigated at some point in time, we can assume it will continue to be irrigated as long as the rain deficit does not decrease. Hence, it should be possible to improve the predictive power of the current model by continuously assimilating remotely sensed irrigation levels.

1.5 Crop monitoring with remote sensing

Remote sensing has increasingly been applied to monitor crop development on large scales [7,8]. Optical images show promising correlations for this purpose. However, they are hindered by atmospheric effects, most notably clouds [9]. On the other hand, synthetic-aperture radar (SAR) measurements experience very little hinder from atmospheric effects, which allows one to obtain more consistent time series [10]. As a result, the body of research on harnessing remote SAR imagery for this purpose is quickly growing [11,12].

Various papers have explored the link between SAR backscatter measurements and water content or water stress in plants. Han et al. [13] and El-Shirbeny and Abutaleb [10] obtained high correlation when fitting SAR backscatter measurement to crop water content measurements and Crop Water Stress Index respectively. Furthermore, a SAR image consists of multiple polarisation channels that can be combined to obtain vegetation indices that have been used to monitor, among others, biomass [14,15] and crop growth [16,17]. These results clearly show the potential of using SAR backscatter to estimate crop water content and crop water stress.

1.6 Research questions

This thesis investigates the use of remote SAR imagery to estimate irrigation levels in the Netherlands. Because of the requirement of practical application, freely available Sentinel-1 SAR images have been used. Thus, the main research question is:

Q. How can Sentinel-1 SAR images be used to estimate irrigation levels of parcels in the Netherlands?

This thesis focuses on using a time series of SAR images to estimate irrigation. Therefore, the main research question can be divided into three sub-questions:

Q1. How can the evolution of Sentinel-1 SAR measurements during the growth phase of a crop be modelled in the presence of rain deficits?

Q2. How can the model be efficiently and reliably calibrated to a large number of parcels?

Q3. How do the values of the calibrated model parameters correlate with irrigation?

1.7 Reader's guide

This thesis is structured as follows. In section 2, we give a description of the Sentinel-1 SAR data used for this project, and how this data is preprocessed to obtain a time series that can be used to calibrate the model. With this basis, we answer the first two research questions in sections 3 and 4. In section 3, we develop a novel methodology to model SAR measurements as a function of crop type, time and rain deficit. This is achieved by combining existing research on plant growth modelling and remote SAR-based crop monitoring. In section 4, we propose three methods to calibrate the model: the standard methods non-linear least squares and differential evolution, and a hybrid of both methods that we customly designed for this problem.

Subsequently, two sections are dedicated to the optimization and validation of the calibration method and the model. In section 5, we compare calibration methods and optimize the performance of the hybrid method. In section 6, we investigate the importance of each model feature in the modelling of system behaviour. Finally, we answer the last research question in section 7, where we analyze several of the most informative clusters in the model parameters.

Next, in section 8, the system behaviour, methodology and results are discussed in more depth. In section 8.1, we propose explanations for some of the unexpected behaviour of the SAR measurements during the growth season. In addition, we make some suggestions on how the understanding of the relation between reality and measurements can be improved in future research. The subsequent two sections give an overview of limitations and possible room for improvement for the calibration (section 8.2) and the modelling (section 8.3). In the final section of the discussion, section 8.4, we discuss the clustering results and give some suggestions on how this research can be used to improve the watervraagprognosetool. The main conclusions are then summarized in chapter 9.

2 Generating radar vegetation index (RVI) time series using Sentinel-1 SAR images

At the root of this project lie the Sentinel-1 SAR images. Remote sensing images are a powerful method to gain access to enormous amounts of data. However, they are inherently noisy (speckle, see section 2.1.1) and prone to biases due to, among others, sidelobes and topographical variations in the terrain. Therefore, they should be treated with care. In this section, we will explain SAR imagery and how a time series of the radar vegetation index can be derived from SAR images. In addition, we will describe the validation data and use that to show that irrigation detection using a single image is infeasible.

2.1 Raw SAR data

2.1.1 SAR imaging technology

A satellite making synthetic-aperture radar (SAR) measurements sends out radio waves and measures the amplitude (intensity) and phase of the returning signal. It makes these measurements in large swaths, measuring along an axis parallel to the ground, perpendicular to the satellite's flight path. This measurement direction is called the ground range, or range for short, see figure 2. The direction of the flight path, and therefore the direction of sequential swaths, is called azimuth.

SAR Measurements are split into up to four parts: VV, VH, HV and HH. These are the result of the different polarisations of a radar wave. VH stands for Vertically transmitted, Horizontally received, and similarly for the other three. The strength of the signal in one of the polarisation channels of an image channel depends on the surface type being observed. The Sentinel-1 images that will be used in this project only contain the VV and VH channels. VV is most sensitive to rough surfaces, whereas VH is most sensitive to volume scatters, such as the canopies of trees [18]. This suits this project well, as we want to measure the abundance of greenery against a rough-surface background.

In our application, we are only interested in the amplitude and not the phase, as that represents how well a certain location reflects the radio wave. The reflective properties of a plant-filled area depend on the water content in the plants [19]. Hence, in a dry period, it should be possible to distinguish crops that are regularly irrigated from crops that are not.

One of the challenges in working with SAR data, is that the amplitudes are inherently subjected to a noise-like effect called speckle. Speckle is the result of constructive and destructive interference from multiple distributed scatters within a resolution cell [20]. Because of its importance, several steps in the preprocessing of SAR imagery aim to reduce the speckle noise, as described in sections 2.1.2 and 2.2.6.

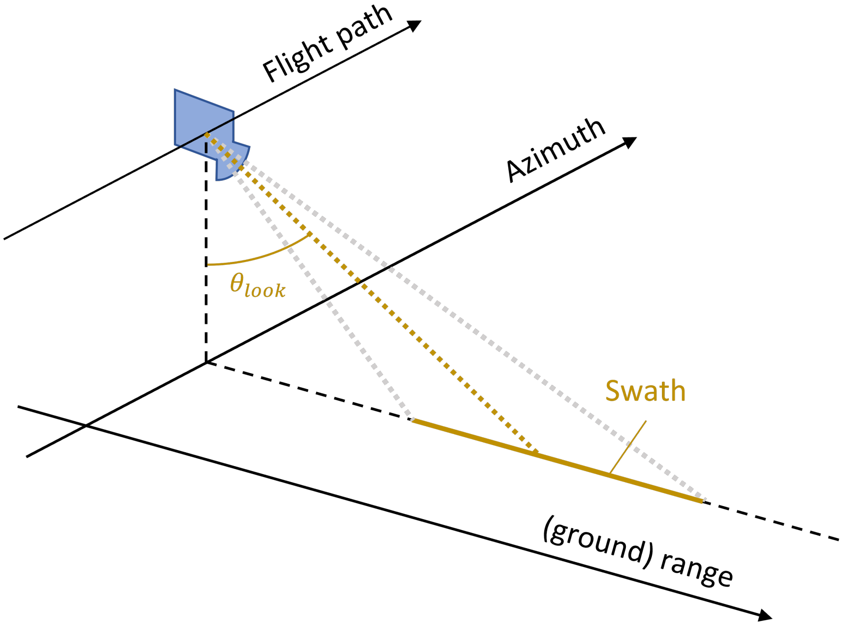

Figure 2: Schematic of satellite observation direction and corresponding range and azimuth coordinate system.

2.1.2 Sentinel-1 GRD images

For this project, European Space Agency's Sentinel-1 data was used, mostly because it is freely available. An additional advantage of Sentinel-1 imagery is their high revisit time. There are two separate Sentinel-1 satellites, Sentinel-1A (S1A) and Sentinel-1B (S1B). Each satellite revisits any point on the equator twice every 12 days, once in an ascending orbit (asc) and once in a descending orbit (dsc). Combined, they form 4 different orbits, one for each direction per satellite. Hence, a single location in the Netherlands is covered by either 4 or 8 images every 12 days, depending on whether the point happens to be positioned in an overlapping area of two different parts of the orbit [21]. Figure 3 shows the coverage of the 12 different stacks that cover part of the Northern Netherlands.

A downside of Sentinel-1 imagery is that their spatial resolution is somewhat low. Senintel-1 has a spatial resolution of 2.7 m to 3.5 m (range, depends on looking angle) by 22 m (azimuth) [21] compared to, for instance, a 1 m resolution for the paid images from TerraSAR-X [22]. An additional downside of lower spatial resolution is that the interference from speckle becomes more dominant, as speckle scales with resolution cell size.

The European Space Agency offers several different kinds of Sentinel-1 products, all derived from the same raw image. For this project, Ground Range Detected (GRD) images were used. GRD data is derived from the amplitude of the raw image (the phase is discarded), which suits our application well. Two preprocessing steps have been performed on the raw images to generate the GRD images: multilooking and projection to ground range using an Earth ellipsoid model [21]. Projection to ground range is used to estimate the geolocation of the satellite image, and will be described in more detail in section 2.2.5.

Multilooking is a relatively simple operation. It downsamples the image by averaging adjacent pixels to reduce the speckle noise [23]. In GRD images, multilooking is also used to create an approximately square pixel spacing. After multilooking, the pixel spacing is 10 m by 10 m, whereas the spatial resolution is 20.4 m by 22.5 m (range by azimuth; note that multilooking reduces spatial resolution) [21]. The multilooking is anisotropic: 5 looks are taken in range (i.e. blocks of 5 pixels are averaged), whereas only 1 look is taken in azimuth.

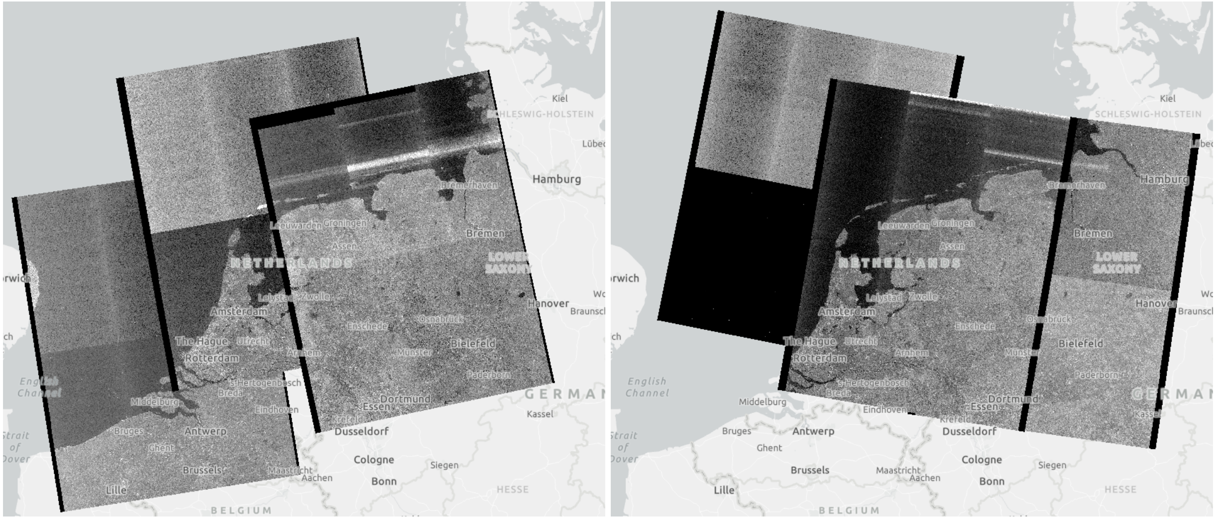

(a) Ascending images

(b) Descending images

Figure 3: Coverage of the Sentinel-1 stack of the area of interest (Northern Netherlands). Note that each rectangle consists of two adjacent images, for a total of twelve separate images, six ascending and six descending.

2.2 SAR image preprocessing

To improve the quality of the data, the SAR images will be subjected to several preprocessing steps. The preprocessing procedures used in literature vary. Filipponi (2019) made an overview of common preprocessing steps for GRD data [24]. These steps mostly overlap with those (occasionally) used by literature on crop monitoring. Each of these steps will be explained in more detail in the subsections below. They are: orbit calibration [13,25], thermal noise removal [13,25], calibration towards β_0, σ_0, γ_0 or the DN (radiometric calibration) [10,13,25,26], speckle noise removal [13,26] (explicitly skipped by Kaplan et al. [25] "to retain spatial resolution"), and geometric correction [13,25,27]. The specific type of geometric correction was specified only by Kaplan et al. [25] (Range Doppler Terrain Correction). Lastly, the only step suggested by Filipponi but not reflected in literature is border noise removal.

In this project, we will apply orbit calibration, thermal noise removal, border noise removal, calibration towards σ_0, and geometric correction. Speckle noise removal will be skipped. In the subsections below, every preprocessing step is described, along with an explanation why we chose (not) to use it. All preprocessing steps will be applied using version 8.0.0 of the SNAP toolbox of the European Space Agency (via the python package snappy).

2.2.1 Orbit calibration

Remote sensing images usually have a corresponding file containing their orbit state vector information. This is used to estimate the incidence angle and geolocation of the measurements. However, the orbit file initially included in a Sentinel-1 product is not very accurate. A few days to weeks after the product has been made available, a more precise orbit file is made available. In the orbit calibration step, these improved orbit files are downloaded so that they can be used in subsequent processing steps [23].

2.2.2 Border noise removal

During some of the initial processing performed to generate the GRD product, "no-value" artefacts can be produced near the edges of the image, especially in the range direction. Pixels in these artefacts are filled with (near) zero values instead of a "no-value" (like null) [23]. Our Area of interest is so large that there will inevitably be some polygons near the border of many images. Hence, it is important to mask the erroneous pixels to avoid the zeros from affecting our results. The border noise removal preprocessing step implements the algorithm designed in [28] which does exactly this.

2.2.3 Thermal noise removal

The measurements contain a constant additive noise from two sources: thermal noise on the sensor itself and standard emission from the surface of the earth. The additive noise gives a positive bias to the signal. That is to say, measured values will on average be higher than the noiseless signal. Therefore, a correction needs to be performed to remove the bias from the measurements. [29]

The magnitude of the noise becomes range and azimuth dependent during corrections for the variation in instrument gain. Hence, the noise in the final product is both range and azimuth dependent. The magnitude of the noise over the image can be modeled and validated with images over regions with very low backscatter such as oceans. The European Space Agency provides such noise predictions with each product. These values are used in the Thermal Noise Removal preprocessing step to subtract the expected noise field from the image. [29]

2.2.4 Radiometric calibration

The raw GRD data comes in a 16-bit data representation called ”Digital Numbers” (DN). The DN is a scaling of the original measurements that was applied to make optimal use of the 16-bit data representation [30]. The radiometric calibration step reverts this scaling and optionally applies a new scaling to obtain one of three products: β_0 (beta-nought), σ_0 (sigma-nought) or γ_0 (gamma-nought) [23].

β_0 is the product if no new scaling is applied [30], and is therefore a direct measurement of the radar brightness. It can be useful if terrain effects are handled separately (for example with the SNAP terrain flattening operator), which is usually the better approach when there is a lot of topography in the region of interest [23].

σ_0 is a correction on β_0 given by $\sigma_0 = \beta_0 \sin(\theta_{x,y})$, where $\theta_{x,y}$ is the local incidence angle [30]. The larger the incidence angle, the larger the projection of a SAR beam onto the earths surface, resulting in a lower illumination per square meter. Transformation to σ_0 appropriately scales the β_0 image to account for the illumination area.

γ_0 is a correction on β_0 given by $\gamma_0 = \beta_0 \tan(\theta_{x,y})$. This scales with the distance travelled by the beam through some layer above the earth. Therefore, γ_0 is most suitable for volume scatters (scatterers that scatter the signal as the beam travels through it), such as the dense foliage in a rainforest [30].

There is no great foliage to be expected on farmland, so γ_0 is not very suitable for this project. Furthermore, we do not separately correct for terrain effects as the area of interest (the Netherlands) does not have a lot of topography. Therefore, σ_0 is the most appropriate calibration.

2.2.5 Geometric correction

Initially, SAR measurements are projected on the ellipsoid approximation of the earth's surface. This means that location estimation will be distorted when there are topographical variations in the terrain [23], see figure 4. This distortion can be corrected by using terrain height information from a digital elevation model.

Over land, the most accurate method for geometric correction is the Range Doppler Terrain Correction developed by Small and Schubert [31]. This algorithm works as follows. Points in the digital elevation model are selected within a region of interest (possibly resampling them to an appropriate density). For each point, the corresponding azimuth time and slant range are calculated using information on the orbit. The azimuth time and slant range are mapped to pixel coordinates (I_a, I_r) within the image. Finally, a new image is created by resampling values in the image to the derived points (I_a, I_r).

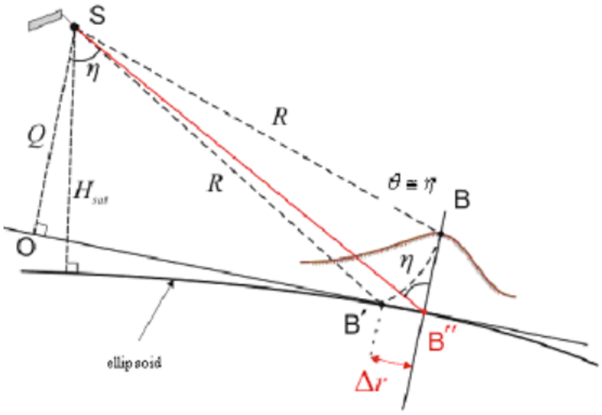

Figure 4: Schematic of distortion to geolocation caused by topographical variations. During ellipsoid projection, point B will be estimated at B' instead of B". Taken from [23]

2.2.6 Speckle filtering

SAR images inherently posses an approximately multiplicative noise called speckle. Speckle is caused by interference from separate scatterers within an observation cell. These scatterers can add either destructively or constructively, leading to the dark and light spotted pattern in SAR images [32].

Speckle filtering is a preprocessing step that aims to reduce the speckle by means of one of four filters. The most commonly applied are the boxcar filter and refined Lee filter [23]. The boxcar filter is especially useful for homogeneous regions, but it blurs sharp edges and point scatterers [23]. On the other hand, the refined Lee filter uses an adaptive, non-square window to preserve edges in the image. Hence, this filter is most practical when the image is used for pattern or object detection [33].

In this project, the location of parcel edges is a given (see section 1.3). In addition, only the average vegetation density over a parcel is of interest. This averaging step compensates for speckle, so there is no need to introduce blur or bias by applying a speckle filter in an earlier step.

2.3 Selecting image pixels within a parcel

In order to fit the evolution of SAR measurements over a parcel to a model, the set of images during the growth season needs to be reduced to a single value per parcel per image. In section 2.3.1, we will develop our own variation of a ray tracing algorithm, to efficiently select pixels within a polygon from an image. In section 2.3.2, we will validate the ray tracing algorithm, as well as the geolocalization estimated by the geometric correction preprocessing step (section 2.2.5).

2.3.1 Raster ray tracing algorithm

Existing Python packages for selecting points contained in a polygon, such as matplotlib.path.mplPath.Path.contains_points and shapely.geometry.Polygon.contains, seemed inadequate as they make no use of the raster format of the SAR images. These methods use a ray tracing algorithm, which loops over all edges for each point in the image. Therefore, they are at least $\mathcal{O}(P_i)\mathcal{O}(E_p)$, where P_i is the number of points in the image, and E_p is the number of edges in the polygon. We can crop the image to around the polygon first, so realistically, this will reduce to $\mathcal{O}(x_p)\mathcal{O}(y_p)\mathcal{O}(E_p)$, where x_p and y_p are the x and y dimension of the polygon.

Making use of the raster format of SAR images, we developed our own variation to the ray tracing algorithm that reduces this to $\mathcal{O}(x_p)(\mathcal{O}(E_p) + \mathcal{O}(y_p))$. This goes as follows. First, the polygons are transformed into the row, column coordinates of the raster image. Then the pseudocode in algorithm 1 finds all integer points within the polygon. Note that in this pseudocode, some edge cases were left out for brevity, such as vertical edges (x1 = x2 so roc = ∞) and a vertex with an integer x-coordinate (which could count for 0 or 1 crossings).

Algorithm 1 Raster ray tracing algorithm

```
for edge in edges do
    x1, x2, y1, y2 ← edge.vertices
    roc ← (y2 - y1) / (x2 - x1)
    for integer x between x1, x2 do
        y ← roc * (x - x1) + y1
        edge_crossings[x].insert(y)
    end for
end for
for x, crossings in edge_crossings do
    crossings.sort()
    i ← 0
    while i < length(crossings) do
        for integer y between crossings[i], crossings[i+1] do
            interior_points.insert([x, y])
        end for
        i ← i + 2
    end while
end for
```

2.3.2 Validating geolocation and pixel selection

The validity of the geolocation of SAR images calculated by the geometric correction preprocessing step (section 2.2.5) and the ray tracing algorithm (section 2.3.1) is paramount. Hence, they need proper validation. This is relatively straightforward: select a parcel that is somewhat visible in the satellite image, and use the ray tracing algorithm on the polygon of that parcel. Plot the selected pixels and compare this to validate that (roughly) the correct pixels were selected. The result is shown in figure 5.

Recognizing the parcel in figure 5b, it is clear that the pixel selection in generated by the ray-tracing algorithm in figure 5a is near ideal. Hence, we can conclude that the ray-tracing algorithm works as expected, and that the geolocation generated by the geometric correction is close to perfect. In contrast, the positioning projected by ArcGis Pro [34] is off by about 20 pixels, or 200 meters (resolution 10x10 meters), see figure 5c. This can be explained by the absence of the orbit calibration and geometric correction steps in the raw GRD image (see section 2.1.2) that was used to generate this figure. In addition, ArcGis Pro itself might not be able to make perfect use of the Ground Control points that are used to define the georeferencing in the raw GRD image.

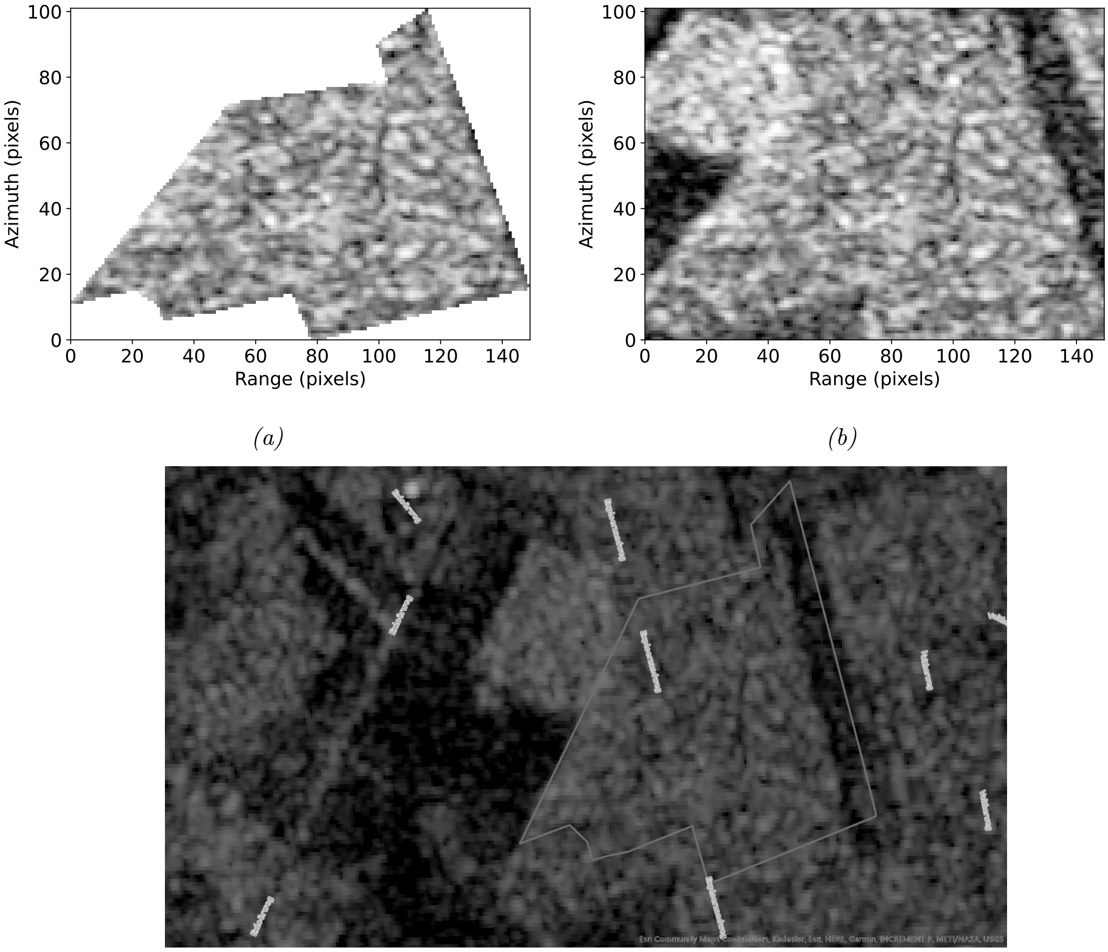

(a) *(b)*

(c)

Figure 5: (a) Pixels selected by the ray tracing algorithm after geometric correction and (b) the same plot in the context of the surrounding pixels. The polygon and the raw GRD image as displayed in ArcGIS Pro [34] is shown in (c). From the shape visible in the SAR image, we can tell that the geolocation determined by the python script is very close to perfect, even though ArcGis Pro is off by around 20 pixels.

2.4 Radar vegetation index (RVI)

There are many different combinations of the polarisation channels of a SAR image that give some measure of the "abundance" of foliage [12]. Researchers have investigated the potential of backscatter ratio [14, 17], radar vegetation index (RVI) [12, 35] and more complicated constructions such as the dual-pol radar vegetation index (DpRVI) [36]. The RVI is particularly well-established [37], and has the advantage that (unlike e.g. the optical NDVI) it increases linearly with crop growth throughout the entirety of the growth phase [38]. This is useful, because a natural decay in growth can be difficult to distinguish from influence of precipitation deficits.

It would be interesting to compare the performance of different vegetation indices for our application. However, in this thesis, there are already plenty of dimensions for optimization, as we will see in the next two sections on modelling and calibration. Therefore, we will limit ourselves to the RVI. Note that though we will only use the RVI in our data analysis, the modelling and calibration methodology we develop in later sections is generic and should work for any vegetation index.

The RVI is defined for the VH and VV polarisations as [39, 40]

$$\mathrm{RVI} = \frac{4\sigma^0_{VH}}{\sigma^0_{VV} + \sigma^0_{VH}}, \tag{2.1}$$

where σ^0_{VH} (m^{-2}) and σ^0_{VV} (m^{-2}) are the backscatter for VH and VV polarisation respectively. Note that RVI is unitless. In this project, the RVI will be calculated pixel-wise and subsequently averaged over each parcel.

2.5 Validation data

The water board Hunze en Aas has kindly provided validation data for this project. For a region of the Netherlands, outlined in the left of figure 6, they provided shapefiles for the dry summers of 2018, 2019 and 2020 describing all areas that were irrigated at least once during that summer. This is depicted in the right of figure 6. There are a decent set of parcels falling both within and outside the irrigated regions (as defined by the location of their centroid), as shown in table 2.

Note that, though useful, this validation data is fairly limited as an "irrigated" parcel could have been irrigated only once, or every few days throughout the summer. We cannot expect to distinguish a time series of a parcel that has been irrigated only once from one that has not been irrigated at all. In fact, each of the dry years had a period of irrigation prohibition where most of the irrigated parcels probably received limited irrigation. These were defined as follows:

- 16-07-2018 up to and including 12-08-2018: irrigation only allowed at night from 19:00 until 7:00
- 30 and 31 July 2019: no irrigation allowed
- 07-08-2020 up to and including 12-08-2020: irrigation only allowed at night from 19:00 until 7:00.

These prohibitions might cause anomalies in the data that confuses our models. For this reason, we will be using data from 2019, which only had a very short irrigation prohibition, to optimize and validate our calibration procedure and model parameterization (see sections 5 and 6). On the other hand, the prohibition periods could provide a source of information if the irrigation prohibition periods turn out to be identifiable in the remote sensing data. However, we will not go investigate that in this thesis.

Table 2: The number of parcels and total area in the 2019 Basisregistratie Gewaspercelen (BRP) for the parcels within the validation region.

crop type	# irrigated parcels	irrigated area (km^2)	# unirrigated parcels	unirrigated area (km^2)
All crops	1033	65.71	2922	140.83
Potatoes	349	25.62	818	47.54
Corn	66	4.07	208	11.08

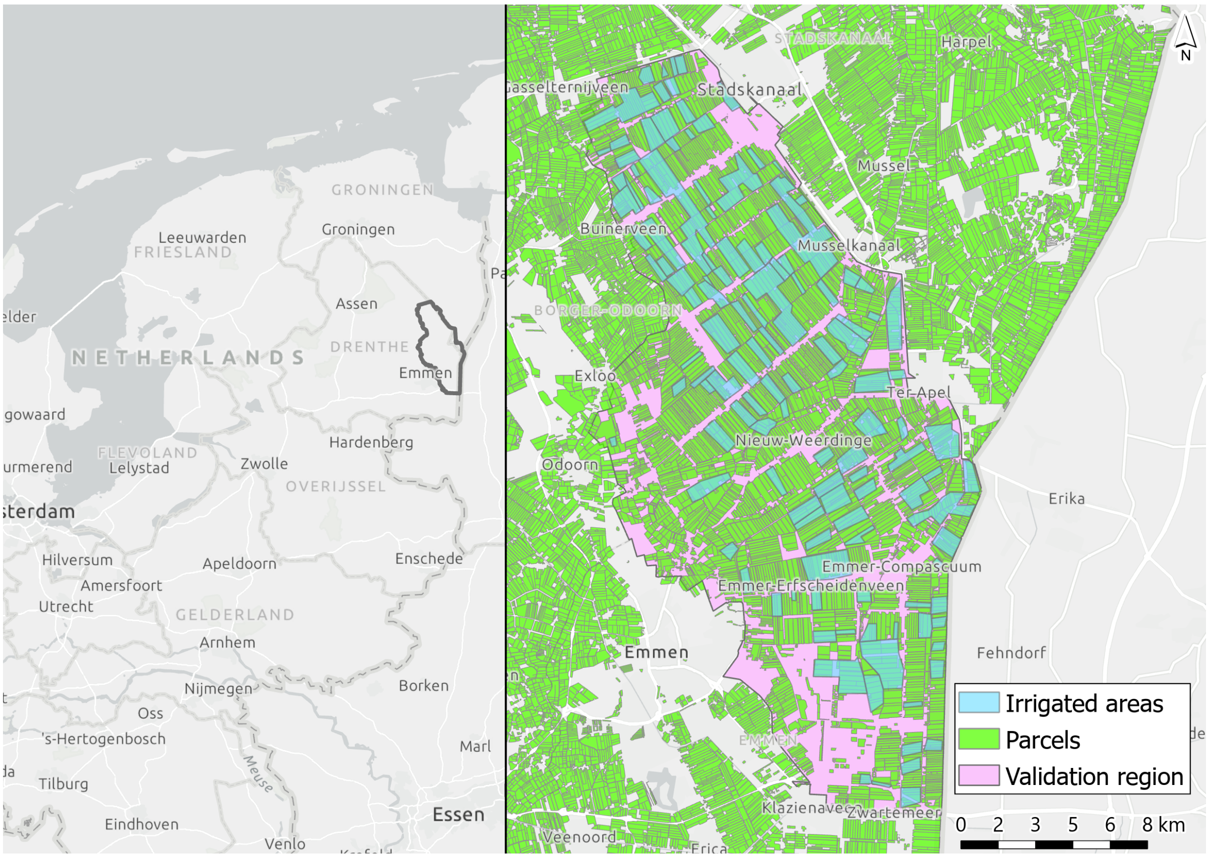

Figure 6: Left: location of the validation region provided by Hunze en Aas. Right: the irrigated areas for the summer of 2019 along with the parcels according to the BRP. Note that we only have information on irrigation about parcels inside the validation region.

2.6 Single image irrigation detection

Ideally, a classifier would be able to distinguish irrigated from unirrigated parcels within a single image. Using multiple images will almost inevitably cause a delay in irrigation detection. One might expect a single-image classifier to feasibly achieve decent performance in extremely dry periods, as irrigated parcels should have a far greater crop abundance. We can very simply verify this for the validation data (see section 2.5) by plotting the average and standard deviation of the RVI (radar vegetation index) over irrigated and unirrigated parcels respectively. This is shown for potato parcels in the dry months of July and August 2018, 2019 and 2020 in figure 7.

Noteworthy is that the irrigated parcels of 2018 seem to consistently surpass the unirrigated parcels from around half July onwards. However, even then, the difference between average RVI of irrigated and unirrigated parcels is only a fraction of the standard deviation. This is even more pronounced in the early images of 2018 and the images of the other years. Clearly, it will be impossible to create a classifier that is capable of reproducing the validation data reasonably well based on only this information. Therefore, in the remainder of this thesis, we will develop a methodology to classify parcels based on a time series of SAR images.

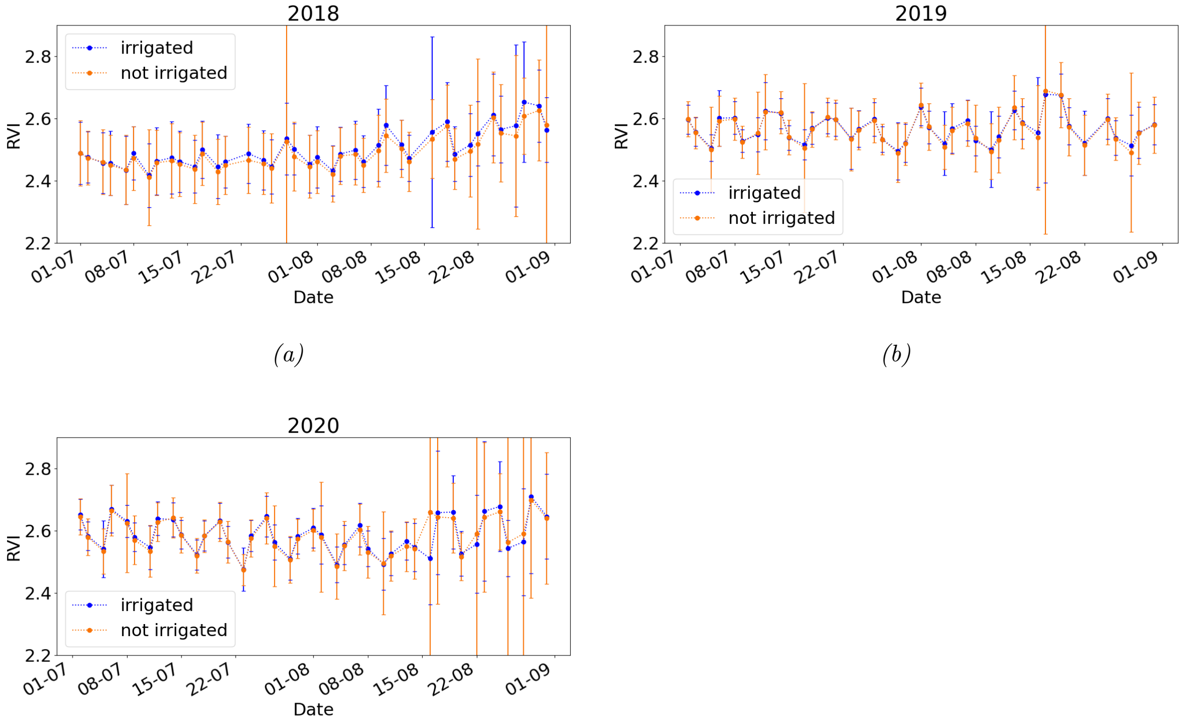

(a) *(b)* *(c)*

Figure 7: Average (dots) and standard deviation (bars) of the radar vegetation index (RVI) over parcels in the validation region for the dry months of July and August of the years 2018, 2019 and 2020. Every dot represents a single image. Note that the average RVI over irrigated parcels of 2018 seems to consistently surpass that of their counterparts for the latter part of 2018. Yet, the difference between the average RVI of irrigated and unirrigated parcels is still insignificant compared to their standard deviation.

2.7 Generating RVI time series

We have built a processing chain that downloads Sentinel-1 GRD images, preprocesses them, selects the pixels contained in each polygon and calculates the average RVI. Finally, these values are written to a database to await further analysis. To determine which part of the year is relevant for the project, we will look at the typical growth season of potatoes and corn.

In the Netherlands, most potatoes are sown in April and harvested in September or October [41]. Similarly, corn is usually sown near the end of April and has to be harvested (by law) before the first of October [42]. To avoid having to take into account the abrupt disappearance of the signal after the harvest, we will end our data analysis at the first of September. Hence, the time series we will use to fit the models will start at the beginning of April and end at the first of September. In addition, a one-month buffer of images before the start of the growth season will be used to generate a baseline measurement (more details in section 3.2).

Therefore, with the processing chain described above, all images over the Netherlands for the years 2018-2021 between March 1 and September 1 were processed. This yielded 4 time series (one per year) for each parcel, where each time series consists of a single value for each image covering the relevant parcel. We will develop a model to describe these time series in the next section. An example of a time series is shown in figure 8.

Each time series consists of images from four different orbits. In figure 8, the time series of each orbit is plotted separately. Notice that there are clear differences between the orbits. For instance, the S1A and S1B ascending orbits (blue and green lines) are fairly consistently above the other two. A large part of the differences between orbits is the result of difference incidence angles. The projection to ground range and geometric correction steps of the preprocessing (sections 2.1.2 and 2.2.5) apply a correction for incidence angle, but these are clearly not perfect. As the time series of the four orbits are clearly distinct, they will cause an important distortion if not treated properly. In the next section, we will develop a methodology that allows us to model the four orbits as a single time series.

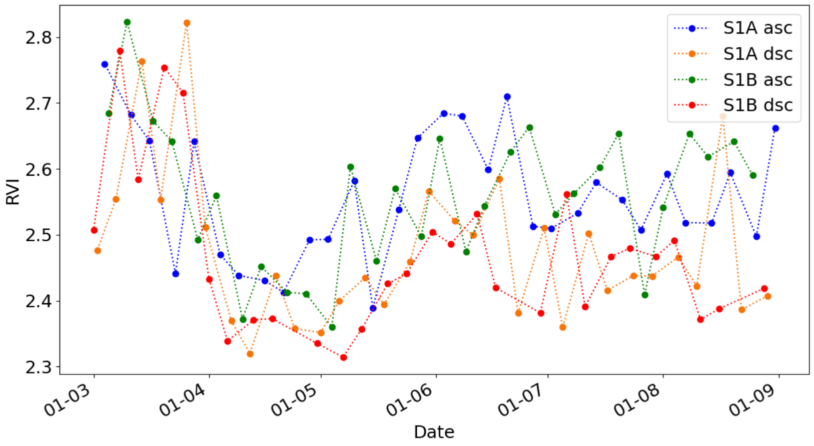

Figure 8: Example of a time series of the RVI of a single parcel during the year 2019. The four orbits are plotted separately.

3 Mathematical modelling of vegetation indices during the growth phase

In this section, we will develop a model that characterizes the behaviour of SAR-derived vegetation indices as a function of rain deficits and moment in the growth phase. As far as we can tell, there is no precedent in literature for a model that describes the behaviour of SAR-derived vegetation indices as a function of rain deficits and growth phase. Hence, we will construct a novel model by combining and expanding upon existing research in related fields. The hypothesis is that the calibration of this model to measurements over unirrigated and (regularly) irrigated parcels will yield distinct clusters in the model parameters. A classifier can then be built based on these clusters.

The derivation of the model consist of two parts. Firstly, in section 3.1, a model for plant growth will be derived based on existing plant growth models from literature. Secondly, in section 3.2, a model to map a state of plant growth to an expected vegetation index will be proposed. Finally, we will formulate several parameterizations of the model with varying degrees of complexity in section 3.3. All parameter units will be left out for brevity, but they can be found in the nomenclature.

3.1 Plant growth model

A large volume of research has shown correlation between SAR-derived vegetation indices and multiple vegetation characteristics like biomass [15, 43] vegetation water content [16, 36, 37] and canopy cover or leaf area index [37]. Hence, the growth model described in this section is not for any of these vegetation characteristics in particular, but rather an unspecified combination of all that one can interpret as the "SAR-responsitivity" of the vegetation. This will be labeled as time-dependent parameter $p^{crop}(t)$.

Plant growth models that assume ideal circumstances generally consist of two phases. The first phase is an exponential phase which can be described as [44, 45]

$$p^{crop}(t)\big|_{rd=0} = p_0^{crop} e^{C_1^{crop}(t-t_0^{parcel})}, \tag{3.1}$$

where t_0^{parcel} is the parcel-dependent start of the growth season, and p_0^{crop} and C_1^{crop} are crop-dependent constants. rd is the rain deficit, so $rd = 0$ (or $rd \leq 0$) signifies ideal circumstances in terms of precipitation. This model will be developed for any definition of the rain deficit. However, in this thesis, we will be using the cumulative rain deficit with a 6-day memory. This was visually estimated from RVI time series like figure 8 and visualisations of the different length rain deficits.

The second phase varies between model types. Biomass can be modelled with linear growth after the exponential phase [44]. On the other hand, the canopy cover $CC(t)$ enters an exponentially decreasing phase due to leaf senescence [45]. The latter can be described by [45]

$$CC(t)\big|_{rd=0} = CC_{t_1}\left(1 - 0.05\left(e^{C(t-t_1)} - 1\right)\right), \tag{3.2}$$

where CC_{t_1} is the canopy cover at the start of the senescence phase t_1, and C is some constant. However, the canopy cover is only one contributor to p^{crop}, and equation (3.2) can be reasonably approximated as linear for $C(t - t_1) \sim 1$. Therefore, we will use a linear approximation to describe the second phase. Thence, an idealized expression for p^{crop} is given by

$$p^{crop}(t)\big|_{rd=0} = \begin{cases} p_0^{crop} e^{C_1^{crop}(t-t_0^{parcel})} & \text{for } t_0^{parcel} \leq t \leq t_0^{parcel} + \Delta t_1^{crop} \\ p_0^{crop} e^{C_1^{crop}\Delta t_1^{crop}} + C_2^{crop}(t - t_0^{parcel} - \Delta t_1^{crop}) & \text{for } t_0^{parcel} + \Delta t_1^{crop} \leq t \leq t_0^{parcel} + \Delta t_2^{crop}, \end{cases} \tag{3.3}$$

where t_0^{parcel} is the start and $t_0^{parcel} + \Delta t_2^{crop}$ (harvest) is the end of the growth season, $t_0^{parcel} + \Delta t_1^{crop}$ is the start of the linear phase, and p_0^{crop}, C_1^{crop} and C_2^{crop} are constants. Here and later, any constants, functions or distributions of random variables marked "*crop*" are assumed to be crop-dependent and parcel-independent. Similarly, the marking "*parcel*" indicates the parameter is assumed to vary per parcel. To derive a more accurate description of p^{crop} that includes adverse circumstances (which will be limited to water deficits in this case), we will first write the above as a differential equation. Including a random variable $\xi^{crop}(t)$ to encompass uncertainties in crop growth, we obtain

$$\left.\frac{dp^{crop}}{dt}\right|_{rd=0} = \begin{cases} C_1^{crop} p^{crop}(t) + \xi^{crop}(t) & \text{for } t_0^{parcel} \leq t \leq t_0^{parcel} + \Delta t_1^{crop} \\ C_2^{crop} + \xi^{crop}(t) & \text{for } t_0^{parcel} + \Delta t_1^{crop} < t \leq t_0^{parcel} + \Delta t_2^{crop}. \end{cases} \tag{3.4}$$

The relationship between crop growth and water supply has mostly been explored with a focus on yield. The Food and Agriculture Organization of the United Nations (FAO) demonstrated that yield influence of water deficits is growth phase dependent [46]. They differentiated five growth phases, establishment, vegetative, flowering, yield formation and ripening. The yield is usually a fruit-like part of the plant, which makes the phases related to fruit formation relatively important. In our project, mostly biomass and canopy formation are relevant, and hence, this phase distinction does not make much sense. Therefore, we will use the commonly applied [46] simplification that water deficit has a linear influence on the differential equation of p^{crop}. Furthermore, we assume that water deficit does not influence the moment of transition to the linear phase nor the distribution of $\xi^{crop}(t)$. This results in

$$\frac{dp^{crop}}{dt} = \begin{cases} i_g^{crop}(rd(t)) C_1^{crop} p^{crop}(t) + \xi^{crop}(t) & \text{for } t_0^{parcel} \leq t \leq t_0^{parcel} + \Delta t_1^{crop} \\ i_g^{crop}(rd(t)) C_2^{crop} + \xi^{crop}(t) & \text{for } t_0^{parcel} + \Delta t_1^{crop} < t \leq t_0^{parcel} + \Delta t_2^{crop}, \end{cases} \tag{3.5}$$
$$p^{crop}(0) = p_0^{crop}$$

where growth inhibitor $i_g^{crop} : \mathbb{R} \to [0,1]$ is given by

$$i_g^{crop}(rd(t)) = \begin{cases} 1 & \text{for } rd(t) \leq rd_{max}^{crop} \\ 1 - \frac{rd(t) - rd_{max}^{crop}}{C_3^{crop}} & \text{for } rd_{max}^{crop} < rd(t) < rd_{max}^{crop} + C_3^{crop} \\ 0 & \text{for } rd(t) \geq rd_{max}^{crop} + C_3^{crop}. \end{cases} \tag{3.6}$$

Here, rd_{max}^{crop} is the maximum rain deficit at which plant growth is uninhibited and C_3^{crop} is a crop-dependent constant.

3.2 Mapping growth stage to vegetation index

In the absence of irrigation, a vegetation index measurement v_i at time t_i ($i \in \{1, 2, .., N\}$) can be modeled as

$$v_i = \begin{cases} v_0 & \text{for } t_i \leq t_0^{parcel} \\ v_0 + h_g^{crop}\left(p^{crop}(t_i), rd(t_i)\right) + \zeta_i^{crop} & \text{for } t_0^{parcel} < t_i \leq t_0^{parcel} + \Delta t_2^{crop} \\ v_0 & \text{for } t_i > t_0^{parcel} + \Delta t_2^{crop}, \end{cases} \tag{3.7}$$

where v_0 is the vegetation index before the start of the growth season t_0^{parcel} and after the end $t_0^{parcel} + \Delta t_2^{crop}$; $p^{crop}(t_i)$ describes the plant growth as per equation (3.5); $h_g^{crop}(p, rd) : \mathbb{R}^2 \to \mathbb{R}$ maps the growth stage p to the expected influence on vegetation index $v_i - v_0$, accounting for temporary influences such as crop water saturation; and ζ_i^{crop} is a random variable encompassing measurement uncertainties. In the rest of this section, the cases before and after the growth season will be left out to ease notation.

Under the assumption that crop-dependent differences in SAR response to crop growth can be captured within the crop abundance $p^{crop}(t)$, crop-independent $g : \mathbb{R} \to \mathbb{R}$ can be defined as

$$g(p) \equiv h_g^{crop}(p, 0). \tag{3.8}$$

We will assume that h_g^{crop} can be separated as $h_g^{crop}(p, rd) = h^{crop}(rd) g(p)$. Here, the precipitation deficit dependent factor $h^{crop}(rd) : \mathbb{R} \to [h_{min}^{crop}, 1]$ monotonously decreases from 1 at $rd = 0$ to some factor $0 \leq h_{min}^{crop} \leq 1$ as $rd \to \infty$. Hence, equation (3.7) reduces to

$$v_i = v_0 + h^{crop}(rd(t_i)) g(p^{crop}(t_i)) + \zeta_i^{crop}. \tag{3.9}$$

We will take two steps to allow us to combine the measurements from the four different orbits (see figure 8). Firstly, the offset v_0 will be defined separately for each orbit. To reduce noise, v_0 will be estimated as the average of the first three measurements of each orbit. This is also the reason we processed an additional month before the start of the growth season (see section 2.7). Since every orbit visits at least once every 12 days, it will take at most 36 days of measurements to define each v_0.

Secondly, the differences between the orbits can be further reduced by expressing v_i in terms of v_{i-1}. Here, v_{i-1} is the previous measurement from the same orbit. As additional benefits, this also reduces the influence from outliers and the accumulation of error from (orbit-dependent) drift.

The difference between two subsequent measurements can be written as

$$\begin{gathered} v_i - v_{i-1} = (h^{crop}(rd(t_i)) - h^{crop}(rd(t_{i-1})))g(p(t_{i-1})) + \\ h^{crop}(rd(t_i))(g(p(t_i)) - g(p(t_{i-1}))) + \zeta_i^{crop} - \zeta_{i-1}^{crop}. \end{gathered} \tag{3.10}$$

where we define $t_0 = t_0^{parcel}$. Note that the expected growth of the first measurement is therefore dependent on the exact location of the start of growth season t_0^{parcel}. We can write equation (3.9) for v_{i-1} as

$$g(p^{crop}(t_{i-1})) = \frac{1}{h^{crop}(rd(t_{i-1}))}(v_{i-1} - v_0 - \zeta_{i-1}^{crop}). \tag{3.11}$$

Substituting this into equation (3.10)

$$\begin{gathered} v_i - v_{i-1} = \left(\frac{h^{crop}(rd(t_i))}{h^{crop}(rd(t_{i-1}))} - 1 \right) (v_{i-1} - v_0 - \zeta_{i-1}^{crop}) + \\ h^{crop}(rd(t_i))(g(p(t_i)) - g(p(t_{i-1}))) + \zeta_i^{crop} - \zeta_{i-1}^{crop}, \end{gathered} \tag{3.12}$$

or

$$\begin{gathered} v_i - v_0 = \frac{h^{crop}(rd(t_i))}{h^{crop}(rd(t_{i-1}))}(v_{i-1} - v_0) + \\ h^{crop}(rd(t_i))(g(p(t_i)) - g(p(t_{i-1}))) - \frac{h^{crop}(rd(t_i))}{h^{crop}(rd(t_{i-1}))}\zeta_{i-1}^{crop} + \zeta_i^{crop}. \end{gathered} \tag{3.13}$$

We can write

$$g(p(t_i)) - g(p(t_{i-1})) = \int_{t_{i-1}}^{t_i} g'(p^{crop}(t)) \frac{dp^{crop}}{dt}(t) dt. \tag{3.14}$$

Substituting equation (3.5),

$$g(p(t_i)) - g(p(t_{i-1})) \approx \begin{cases} \displaystyle\int_{t_{i-1}}^{t_i} g'(p^{crop}(t)) \left(C_1^{crop} i_g^{crop}(rd(t)) p^{crop}(t) + \xi^{crop}(t) \right) dt \\ \qquad\qquad \text{for } t_0^{parcel} \leq t_i \leq t_0^{parcel} + \Delta t_1^{crop} \\ \displaystyle\int_{t_{i-1}}^{t_i} g'(p^{crop}(t)) \left(C_2^{crop} i_g^{crop}(rd(t)) + \xi^{crop}(t) \right) dt \\ \qquad\qquad \text{for } t_0^{parcel} + \Delta t_1^{crop} < t_{i-1} \leq t_0^{parcel} + \Delta t_2^{crop}. \end{cases} \tag{3.15}$$

For the edge case $t_{i-1} < t_0^{parcel} + \Delta t_1^{crop} < t_i$ we have

$$\begin{gathered} g(p(t_i)) - g(p(t_{i-1})) \approx \int_{t_{i-1}}^{t_0^{parcel} + \Delta t_1^{crop}} g'(p^{crop}(t)) \left(C_1^{crop} i_g^{crop}(rd(t)) p^{crop}(t) + \xi^{crop}(t) \right) dt + \\ \int_{t_0^{parcel} + \Delta t_1^{crop}}^{t_i} g'(p^{crop}(t)) \left(C_2^{crop} i_g^{crop}(rd(t)) + \xi^{crop}(t) \right) dt \end{gathered} \tag{3.16}$$

To ease notation, we define $s^{parcel}(t) : \mathbb{R} \to \mathbb{R}$ as

$$s^{parcel}(t) = \begin{cases} C_1^{crop} p^{crop}(t) & \text{for } t_0^{parcel} \leq t \leq t_0^{parcel} + \Delta t_1^{crop} \\ C_2^{crop} & \text{for } t_0^{parcel} + \Delta t_1^{crop} < t \leq t_0^{parcel} + \Delta t_2^{crop}. \end{cases} \tag{3.17}$$

Equation (3.13) can be written as

$$\begin{gathered} v_i - v_0 = \frac{h^{crop}(rd(t_i))}{h^{crop}(rd(t_{i-1}))} (v_{i-1} - v_0) + \\ h^{crop}(rd(t_i)) \int_{t_{i-1}}^{t_i} g'(p^{crop}(t)) \left(i_g^{crop}(rd(t)) s^{parcel}(t) + \xi^{crop}(t) \right) dt - \frac{h^{crop}(rd(t_i))}{h^{crop}(rd(t_{i-1}))} \zeta_{i-1}^{crop} + \zeta_i^{crop}, \end{gathered} \tag{3.18}$$

In the integral over t_{i-1} to t_i, we can approximate $p^{crop}(t) \approx p^{crop}(t_{i-1})$. This results in

$$\begin{gathered} v_i - v_0 = \frac{h^{crop}(rd(t_i))}{h^{crop}(rd(t_{i-1}))} (v_{i-1} - v_0) + \\ h^{crop}(rd(t_i)) g' \left(p^{crop}(t_{i-1})\right) \left(s_d^{parcel}(t_{i-1}) \int_{t_{i-1}}^{t_i} i_g^{crop}(rd(t)) dt + \int_{t_{i-1}}^{t_i} \xi^{crop}(t) dt \right) - \frac{h^{crop}(rd(t_i))}{h^{crop}(rd(t_{i-1}))} \zeta_{i-1}^{crop} + \zeta_i^{crop}, \end{gathered} \tag{3.19}$$

where, to cover the edge case from equation (3.16)

$$s_d^{parcel}(t_{i-1}) = \begin{cases} \left(t_0^{parcel} + \Delta t_1^{crop} - \ t_{i-1} \right) s^{parcel}(t_{i-1}) + \left(t_i - \left(t_0^{parcel} + \Delta t_1^{crop} \right) \right) s^{parcel}(t_i) \\ \qquad\qquad\qquad\qquad\qquad \text{for } t_{i-1} < t_0^{parcel} + \Delta t_1^{crop} < t_i \\ s^{parcel}(t_{i-1}) \qquad \text{for all other } i. \end{cases} \tag{3.20}$$

Let $t_{i,k}$ for $k \in \{0, 1, ..., n_i\}$ with $t_{i-1} \leq t_{i,0} < t_{i,1} < .. < t_{i,n_i} \leq t_i$, be the times between t_{i-1} and t_i at which we have a measurement of the rain deficit. The integral over i_g^{crop} can then be estimated as

$$\int_{t_{i-1}}^{t_i} i_g^{crop}(rd(t)) dt \approx \sum_{k=0}^{n_i} \frac{1}{2} (t_{i,k+1} - t_{i,k-1}) i_g^{crop}(rd(t_{i,k})), \tag{3.21}$$

where we define $t_{i,n_i+1} = t_i$ and $t_{i,-1} = t_{i-1}$ for convenience.

Assuming $\{\zeta_i^{crop}\}$ are independently identically normally distributed with $\zeta_i^{crop} \sim \mathcal{N}(0, (\sigma_\eta^{crop})^2)$ and similarly, $\int_{t_{i-1}}^{t_i} \xi^{crop}(t) dt \sim \mathcal{N}(0, (\sigma_\xi^{crop})^2)$ we can write

$$\begin{gathered} v_i - v_0 = \frac{h^{crop}(rd(t_i))}{h^{crop}(rd(t_{i-1}))} (v_{i-1} - v_0) + \\ h^{crop}(rd(t_i)) g' \left(p^{crop}(t_{i-1})\right) s_d^{parcel}(t_{i-1}) \left(\sum_{k=0}^{n_i} \frac{1}{2} (t_{i,k+1} - t_{i,k-1}) i_g^{crop}(rd(t_{i,k})) \right) + \zeta_i'^{crop}, \end{gathered} \tag{3.22}$$

where

$$\zeta_i'^{crop} \sim \mathcal{N} \left(0, \left(\frac{h^{crop}(rd(t_i))}{h^{crop}(rd(t_{i-1}))} + 1 \right) (\sigma_\eta^{crop})^2 + h^{crop}(rd(t_i)) g' \left(p^{crop}(t_{i-1})\right) (\sigma_\xi^{crop})^2 \right). \tag{3.23}$$

Finally, for $p^{crop}(t_{i-1})$ we will make an estimate based on the previous measurement v_{i-1}. This can be obtained from equation (3.9),

$$g(p^{crop}(t_{i-1})) \approx \frac{v_{i-1} - v_0}{h^{crop}(rd(t_{i-1}))}. \tag{3.24}$$

In the expression for $v_i - v_0$ in equation (3.22), the remaining unknowns are the model parameters C_1^{crop}, C_2^{crop}, Δt_1^{crop}, Δt_2^{crop}, t_0^{parcel} (all contained in s_d^{parcel}), C_3^{crop}, rd_{max}^{crop} (both contained in i_g^{crop}) and p_0^{crop} (from the initial condition of $p^{crop}(t)$, see equation (3.5)), and the functions h^{crop} and g. In the next section, we will discuss the different parameterizations of h^{crop}, g and some simplifications of p^{crop} that will be used to calibrate the model to the data.

3.3 Simplifications and model parameterizations

SAR-derived vegetation indices are a considerably noisy indicator of plant growth. In addition, a single growth season only consists of several tens of measurements. As a result, the model is quite prone to overfitting. Therefore, we will be evaluating several different parameterizations for h^{crop} and g, as well as simplifications to i_g^{crop} and the differential equation of $p^{crop}(t)$. In total, there will be 16 different combinations. In addition to those, we will also assess whether it is best to fit Δt_2^{crop} and t_0^{parcel}, or to just assume the growth season starts/ends at the first/last measurement of the time series. Note that we specifically chose our measurement interval in section 2.7 to avoid the need of fitting Δt_2^{crop}. This is useful, because, as we will see in sections 5.1 and 6.2, fitting Δt_2^{crop} results in a considerable increase of computation time, and significantly increases the risk of overfitting.

For i_g^{crop}, we will be using one simplification to equation (3.6). rd_{max}^{crop} can be interpreted as the highest rain deficit for which the crop experiences no hinder to growth. This might be reasonably approximated to zero, indicating that as soon as there is a rain deficit, the crop growth will experience some inhibition. Hence, we will be using two forms for i_g^{crop}: one where rd_{max}^{crop} is a model parameter, and one where $rd_{max}^{crop} = 0$.

There seems to be no research about $h^{crop}(rd(t))$. Hence, we will be using two simple expressions. The first is that rain deficits have no temporary influence on vegetation index, i.e.

$$h^{crop} = 1. \tag{3.25}$$

The second is a linear relationship:

$$h^{crop}(rd(t)) = \begin{cases} 1 & \text{for } rd(t) \leq rd_{max}^{crop} \\ 1 - \frac{rd(t) - rd_{max}^{crop}}{C_3^{crop}}(1 - h_{min}^{crop}) & \text{for } rd_{max}^{crop} < rd(t) < rd_{max}^{crop} + C_3^{crop} \\ h_{min}^{crop} & \text{for } rd(t) \geq rd_{max}^{crop} + C_3^{crop}. \end{cases} \tag{3.26}$$

where $0 \leq h_{min}^{crop} \leq 1$ is a model parameter. Here, we reduced the dimensionality of the fit space by assuming that h^{crop} follows the same form as i_g^{crop}, with the only difference that it goes from 1 to h_{min}^{crop} instead 0.

For g and p^{crop}, we will evaluate four different parameterizations. The first is the simplest model that rests on the assumption that the vegetation index linearly increases throughout the entire growth phase (and that g and p^{crop} are both linear individually). This assumption is supported by the findings of [38]. This results in

$$g'(p^{crop}(t_i))s_d^{parcel}(t_i) = C_1^{crop}. \tag{3.27}$$

Note that here, $C_2^{crop} = C_1^{crop}$ and g' is constant because g is linear. We can expand this slightly by approximating the exponential part of p^{crop} as linear, allowing p^{crop} to be bilinear, i.e.

$$g'(p^{crop}(t_i))s_d^{parcel}(t_i) = \begin{cases} C_1^{crop} & \text{for } t_0^{parcel} \leq t_i \leq t_0^{parcel} + \Delta t_1^{crop} \\ C_2^{crop} & \text{for } t_0^{parcel} + \Delta t_1^{crop} < t_i \leq t_0^{parcel} + \Delta t_2^{crop}. \end{cases} \tag{3.28}$$

Here, we left out the edge case of equation (3.20) for brevity.

For the third expression for g and p^{crop}, we will use the most general exponential-linear format for p^{crop}, but keep g linear. Again leaving out the edge case, we get

$$g'(p^{crop}(t_i))s_d^{parcel}(t_i) = \begin{cases} C_1^{crop} p^{crop}(t_{i-1}) & \text{for } t_0^{parcel} \leq t_i \leq t_0^{parcel} + \Delta t_1^{crop} \\ C_2^{crop} & \text{for } t_0^{parcel} + \Delta t_1^{crop} < t_i \leq t_0^{parcel} + \Delta t_2^{crop} \end{cases} \tag{3.29}$$

where, from equation (3.24),

$$p^{crop}(t_{i-1}) \approx p_0^{crop} + \frac{1}{C_4}\left(\frac{\max(0, v_{i-1} - v_0)}{h^{crop}(rd(t_{i-1}))}\right). \tag{3.30}$$

where C_4 is a crop-independent model parameter, and negative $v_{i-1} - v_0$ are set to zero to ensure $p^{crop}(t_{i-1}) \geq p_0^{crop}$. When the model is calibrated for each crop separately, as is the case in this project, it becomes more sensible to combine C_1^{crop} with C_4 and p_0^{crop}. Defining $p_{g,0}^{crop} = C_1^{crop} p_0^{crop}$ and $C_4^{crop} = \frac{C_4}{C_1^{crop}}$ we obtain

$$g'(p^{crop}(t_i))s_d^{parcel}(t_i) = \begin{cases} p_{g,0}^{crop} + \frac{1}{C_4^{crop}} \left(\frac{\max(0, v_{i-1} - v_0)}{h^{crop}(rd(t_{i-1}))} \right) & \text{for } t_0^{parcel} \leq t_i \leq t_0^{parcel} + \Delta t_1^{crop} \\ C_2^{crop} & \text{for } t_0^{parcel} + \Delta t_1^{crop} < t_i \leq t_0^{parcel} + \Delta t_2^{crop} \end{cases} \tag{3.31}$$

Fourthly, we will go back to linear p^{crop} but use a quadratic for g:

$$g(p^{crop}) = C_5(p^{crop} - p_0^{crop})^2 + C_6(p^{crop} - p_0^{crop}). \tag{3.32}$$

A non-linear g has some support in the findings of [37]. We will assume g is strictly increasing over the entire range of p^{crop}. Inverting the quadratic equation we obtain

$$p^{crop}(t_{i-1}) \approx p_0^{crop} + \frac{-C_6 + \sqrt{C_6^2 + 4C_5 \frac{\max(0, v_{i-1} - v_0)}{h^{crop}(rd(t_{i-1}))}}}{2C_5}, \tag{3.33}$$

where negative $v_{i-1} - v_0$ are set to zero to ensure $p^{crop}(t_{i-1}) \geq p_0^{crop}$, the "+" in front of the square root (rather than a minus) is the result of the strictly increasing property of g, and we substituted equation (3.24) for $g(p^{crop})$. Furthermore, the combination C_6, C_5 (and h_{min} if applicable) has to be such that $C_6^2 + 4C_5 \frac{\max(0, v_{i-1} - v_0)}{h^{crop}(rd(t_{i-1}))} \geq 0$ for all i. Substituting this into g' yields

$$g'(p^{crop}(t_i))s_d^{parcel}(t_i) = C_1^{crop} \sqrt{C_6^2 + 4C_5 \frac{\max(0, v_{i-1} - v_0)}{h^{crop}(rd(t_{i-1}))}}. \tag{3.34}$$

Again, we combine model parameters, in this case C_1^{crop} with C_6 and C_5. $C_1^{crop} > 0$, so we can take it into the root and define $C_6^{crop} = (C_6 C_1^{crop})^2$ and $C_5^{crop} = C_5 (C_1^{crop})^2$. We thus obtain

$$g'(p^{crop}(t_i))s_d^{parcel}(t_i) = \sqrt{C_6^{crop} + 4C_5^{crop} \frac{\max(0, v_{i-1} - v_0)}{h^{crop}(rd(t_{i-1}))}}. \tag{3.35}$$

The requirement for a real solution to the square root becomes $C_6^{crop} + 4C_5^{crop} \frac{\max(0, v_{i-1} - v_0)}{h^{crop}(rd(t_{i-1}))} \geq 0$ for all i. During the calibration procedure, it will be difficult to prevent the algorithm from trying solutions where one of the data points gives a complex root. Therefore, to ensure that the algorithm does not converge to a complex solution while simultaneously guiding the algorithm back to domain with real solutions, we define

$$g'(p^{crop}(t_i))s_d^{parcel}(t_i) = \begin{cases} \sqrt{C_6^{crop} + 4C_5^{crop} \frac{\max(0, v_{i-1} - v_0)}{h^{crop}(rd(t_{i-1}))}} & \text{for } C_6^{crop} + 4C_5^{crop} \frac{\max(0, v_{i-1} - v_0)}{h^{crop}(rd(t_{i-1}))} \geq 0 \\ 10^9 \left(C_6^{crop} + 4C_5^{crop} \frac{\max(0, v_{i-1} - v_0)}{h^{crop}(rd(t_{i-1}))} \right) & \text{for } C_6^{crop} + 4C_5^{crop} \frac{\max(0, v_{i-1} - v_0)}{h^{crop}(rd(t_{i-1}))} < 0. \end{cases} \tag{3.36}$$

The factor 10^9 should ensure that no significantly complex values are feasible. We chose to set an outlying value for $g'(p^{crop}(t_i))s_d^{parcel}(t_i)$, rather than for the error statistic (section 4.1) directly, for convenient integration with the surrounding algorithms.

Most of the model parameters (are assumed to) obey certain bounds, which are given by

$$\begin{gathered} C_1^{crop}, C_3^{crop}, C_4^{crop}, C_6^{crop} p_{g,0}^{crop} > 0, \\ rd_{max}^{crop} \geq 0, \\ 0 \leq h_{min}^{crop} \leq 1, \\ t_0^{parcel} \leq \text{July 17}, \\ \Delta t_1^{crop} \geq 15 \text{ days}, \\ \Delta t_2^{crop} \geq 45 \text{ days}, \end{gathered} \tag{3.37}$$

C_2^{crop} is entirely free. C_5^{crop} is entirely free, except for the limitation that $C_6^{crop}+4C_5^{crop}\frac{\max(0,v_{i-1}-v_0)}{h^{crop}(rd(t_{i-1}))} \geq 0$ for all i.

The bounds on t_0^{parcel}, Δt_1^{crop} and Δt_2^{crop} were chosen so that there are at least 45 days in the growth season and at least 15 days in the first phase. A lower bound to the length of the second phase is difficult to implement as the upper bound for Δt_1^{crop} would depend on t_0^{parcel} and Δt_2^{crop}. Hence, it has been left out.

In total, we have four expressions for the combination of g and p^{crop}, and two each for i_g^{crop} and h^{crop}. Adding the two times two possibilities for whether to fit t_0^{parcel} and Δt_2^{crop}, there are a total of 64 model parameterizations, ranging from two to nine model parameters. Rather than investigating the performance of each, we take a single base case and separately explore the variation(s) of each variable. As a base case, we have chosen to calibrate only t_0^{parcel} and use the simplest form everything else, i.e.

- g, p^{crop} linear, $rd_{max}^{crop} = 0$, $h^{crop} = 1$, t_0^{parcel} variable, Δt_2^{crop} fixed.

We did not fix t_0^{parcel} in the base case, because t_0^{parcel} is necessary to ensure that the model is actually calibrated to the part of the data that reflects the behaviour we are looking for, as will be shown in section 6. The combinations we will be investigating (in addition to the base case) are:

- linear, t_0^{parcel} fixed,
- linear, h_{min}^{crop} variable ,
- linear, rd_{max}^{crop} variable,
- linear, Δt_2^{crop} variable,
- bilinear
- exponential
- quadratic

where unmentioned parameters are set to their base case. Note how we abbreviated g linear, p^{crop} linear/bilinear/exponential and g quadratic, p^{crop} linear; these abbreviations shall be used in the remainder of this report. These eight parameterizations of the model (including the base case) shall be referred to as the "basic model parameterizations". These parameterizations will be used in sections 5 and 6 where we validate and compare the calibration approaches and different model parameterizations.

4 Calibration methods for the vegetation index model

The model parameters proposed in the previous section are assumed to vary between crops or parcels. Therefore, they need to be estimated using a calibration procedure. Other than t_0^{parcel}, the model parameters are all assumed to be crop-dependent and parcel-independent. Hence, these parameters need to be calibrated for each crop type using all data for all years over all parcels that cultivate that crop. However, instead of that approach, we will be calibrating the data from each parcel for each year separately. The estimations for the model parameters can then be used in a cluster analysis to see if it is possible to identify different behaviour types, such as irrigated and non-irrigated parcels.

In this section, we will explain the three algorithms we will use to calibrate the model parameters to an RVI time series. To make this more convenient, we will first give a proper mathematical definition of the optimization problem and introduce more appropriate notation in section 4.1.

4.1 Formulation of the optimization problem

Let $\mathbf{v} \in \mathbb{R}^N$ be the vector of N observed vegetation indices and $\mathbf{t} \in \mathbb{R}^N$ the corresponding observation times. In addition, we define $\mathbf{v}_{-1} \in \mathbb{R}^N$ and $\mathbf{t}_{-1} \in \mathbb{R}^N$ as the observations and observation times of the previous measurement in the same orbit. That is to say,

$$\mathbf{t} = \begin{pmatrix} t_1 \\ t_2 \\ t_3 \\ \vdots \\ t_N \end{pmatrix}, \qquad \mathbf{t}_{-1} = \begin{pmatrix} t_{b1} \\ t_1 \\ t_2 \\ \vdots \\ t_{N-1} \end{pmatrix}, \qquad \mathbf{v} = \begin{pmatrix} v_1 \\ v_2 \\ v_3 \\ \vdots \\ v_N \end{pmatrix}, \qquad \mathbf{v}_{-1} = \begin{pmatrix} v_{b1} \\ v_1 \\ v_2 \\ \vdots \\ v_{N-1} \end{pmatrix}, \tag{4.1}$$

where v_{b1} and t_{b1} are the observation and observation time of the measurement before v_1, i.e. one of the three measurements that is used in the definition of v_0. Note that this is defined for each of the four orbits separately. That is to say, for the first i with v_i in the second orbit, element i of $\mathbf{v}_{-1}$ is v_{b2} instead of v_{i-1}.

Let $\mathbf{C} \in \mathbb{R}^M$ be the vector of the M model parameters. Let the elements of $\mathbf{C}$ be denoted by C_j for $j \in \{1, 2, ..., M\}$. A given parameterization of the model can be denoted in vectorized format as $f(\mathbf{t}, \mathbf{t_{-1}}, \mathbf{v_{-1}}, \mathbf{C}) : \mathbb{R}^N \times \mathbb{R}^N \times \mathbb{R}^N \times \mathbb{R}^M \to \mathbb{R}^N$.

In this thesis, we will be using a least squares error statistic to define the calibration optimization problem. The optimization problem can be formulated as:

Find $\mathbf{C}$ such that the error statistic

$$E(\mathbf{C}) = ||\mathbf{v} - f(\mathbf{t}, \mathbf{t_{-1}}, \mathbf{v_{-1}}, \mathbf{C})||_2^2 \tag{4.2}$$

is minimal.

Here, $|| \cdot ||_2^2$ is the square of the Euclidean norm.

Solving this optimization problem is not quite straightforward, because each of the model parameterizations is nonlinear in at least one of the model parameters. In addition, the derivative of the model parameterization with respect to its model parameters is discontinuous for many of the parameters (for instance, t_0^{parcel}). This is cause to suspect that derivative-based methods, such as gradient descent methods, might not converge to the most optimal solution. The alternative is a more stochastic algorithm such as differential evolution.

For this calibration problem, we will assess non-linear least squares (derivative-based), differential evolution (stochastic; little reliance on differentiability), and a hybrid between both methods that we customly designed for this problem. For this, the "curve_fit" and "differential_evolution" from the scipy.optimize package will be used.

4.2 Non-linear least squares

4.2.1 Algorithm

(Non-linear) least squares is designed for the error statistic with Euclidian norm $||\cdot||_2^2$. The set of optimal model parameters $\mathbf{C}_{opt}$ minimizes the error statistic. Therefore, at this point, the derivatives to the model parameters are zero, i.e.

$$\nabla_{\mathbf{C}} E(\mathbf{C}_{opt}) = \nabla_{\mathbf{C}} ||\mathbf{v} - f(\mathbf{t}, \mathbf{t_{-1}}, \mathbf{v_{-1}}, \mathbf{C}_{opt})||_2^2 = \mathbf{0}, \tag{4.3}$$

where $\mathbf{0} \in \mathbb{R}^M$ is the length M zero vector, $\nabla_{\mathbf{C}}$ is the gradient operator with respect to $\mathbf{C}$, i.e.

$$\nabla_{\mathbf{C}} = \begin{pmatrix} \frac{\partial}{\partial C_1} \\ \frac{\partial}{\partial C_2} \\ \vdots \\ \frac{\partial}{\partial C_M} \end{pmatrix}. \tag{4.4}$$

The expression can be rewritten as follows:

$$\begin{aligned} \nabla_{\mathbf{C}} ||\mathbf{v} - f(\mathbf{t}, \mathbf{t_{-1}}, \mathbf{v_{-1}}, \mathbf{C}_{opt})||_2^2 &= \nabla_{\mathbf{C}} \Big(\left(\mathbf{v} - f(\mathbf{t}, \mathbf{t_{-1}}, \mathbf{v_{-1}}, \mathbf{C}_{opt})\right)^T \left(\mathbf{v} - f(\mathbf{t}, \mathbf{t_{-1}}, \mathbf{v_{-1}}, \mathbf{C}_{opt})\right) \Big) \\ &= 2 \Big(\nabla_{\mathbf{C}} \left(\mathbf{v} - f(\mathbf{t}, \mathbf{t_{-1}}, \mathbf{v_{-1}}, \mathbf{C}_{opt})\right)^T \Big) \left(\mathbf{v} - f(\mathbf{t}, \mathbf{t_{-1}}, \mathbf{v_{-1}}, \mathbf{C}_{opt})\right) \\ &= -2 \Big(\nabla_{\mathbf{C}} \left(f(\mathbf{t}, \mathbf{t_{-1}}, \mathbf{v_{-1}}, \mathbf{C}_{opt})\right)^T \Big) \left(\mathbf{v} - f(\mathbf{t}, \mathbf{t_{-1}}, \mathbf{v_{-1}}, \mathbf{C}_{opt})\right) = \mathbf{0}. \end{aligned} \tag{4.5}$$

The Jacobian Matrix $\mathbf{J}(\mathbf{C}) \in \mathbb{R}^{N \times M}$ of f is given by

$$\mathbf{J}(\mathbf{C}) = \nabla_{\mathbf{C}}^T f(\mathbf{t}, \mathbf{t_{-1}}, \mathbf{v_{-1}}, \mathbf{C}) = \left(\frac{\partial}{\partial C_1} f(\mathbf{t}, \mathbf{t_{-1}}, \mathbf{v_{-1}}, \mathbf{C}), ..., \frac{\partial}{\partial C_M} f(\mathbf{t}, \mathbf{t_{-1}}, \mathbf{v_{-1}}, \mathbf{C}) \right). \tag{4.6}$$

Note that $f(\mathbf{t}, \mathbf{t_{-1}}, \mathbf{v_{-1}}, \mathbf{C}) \in \mathbb{R}^N$ and therefore $\frac{\partial}{\partial C_j} f(\mathbf{t}, \mathbf{t_{-1}}, \mathbf{v_{-1}}, \mathbf{C}) \in \mathbb{R}^N$. Equation (4.5) can then be written as

$$-2\mathbf{J}^T(\mathbf{C}_{opt}) \left(\mathbf{v} - f(\mathbf{t}, \mathbf{t_{-1}}, \mathbf{v_{-1}}, \mathbf{C}_{opt})\right) = \mathbf{0}. \tag{4.7}$$

When f is linear in the model parameters $\mathbf{C}$, equation (4.7) reduces to a closed-form matrix equation. When f is non-linear in the model parameters $\mathbf{C}$, no general closed form solution exists. Non-linear least squares refers to a heuristic method that iteratively approaches a (local) minimum of the error statistic.

The iterative process goes as follows. Given an estimation of the parameters $\mathbf{C^k}$, a subsequent (improved) estimation $\mathbf{C^{k+1}}$ is produced by solving equation (4.7) for a linearization of $f(\mathbf{t}, \mathbf{t_{-1}}, \mathbf{v_{-1}}, \mathbf{C}_{opt})$ around $\mathbf{C^k}$. The linearization is given by the first order Taylor polynomial:

$$f(\mathbf{t}, \mathbf{t_{-1}}, \mathbf{v_{-1}}, \mathbf{C}_{opt}) \approx f(\mathbf{t}, \mathbf{t_{-1}}, \mathbf{v_{-1}}, \mathbf{C^k}) + \mathbf{J}(\mathbf{C^k})(\mathbf{C}_{opt} - \mathbf{C^k}), \tag{4.8}$$

where we directly expressed the sum over the derivatives as a matrix multiplication with the Jacobian matrix $\mathbf{J}(\mathbf{C^k})$. Replacing $\mathbf{C}_{opt}$ by the next estimation $\mathbf{C^{k+1}}$ and substituting into equation (4.7) gives an expression for $\mathbf{C^{k+1}}$

$$-2\mathbf{J}^T(\mathbf{C^k})\Big(\mathbf{v} - f(\mathbf{t}, \mathbf{t_{-1}}, \mathbf{v_{-1}}, \mathbf{C^k}) - \mathbf{J}(\mathbf{C^k})(\mathbf{C^{k+1}} - \mathbf{C^k})\Big) = \mathbf{0}, \tag{4.9}$$

where the Jacobian transpose $\mathbf{J}^T(\mathbf{C}_{opt})$ is also approximated using $\mathbf{C^k}$. This can be written as

$$\mathbf{J}^T(\mathbf{C^k})\mathbf{J}(\mathbf{C^k})(\mathbf{C^{k+1}} - \mathbf{C^k}) = \mathbf{J}^T(\mathbf{C^k})\big(\mathbf{v} - f(\mathbf{t}, \mathbf{t_{-1}}, \mathbf{v_{-1}}, \mathbf{C^k})\big). \tag{4.10}$$

Hereafter, $\mathbf{C^{k+1}}$ can be obtained through a simple linear system solver. Starting from an initial guess $\mathbf{C}^0$, subsequent estimations $\mathbf{C^k}$ can be obtained by iteratively solving this linear system, until the difference between succeeding $\mathbf{C^k}$ is deemed sufficiently small.

4.2.2 Limitations and use case

The main limitation of non-linear least squares is that convergence to the global minimum is only guarantied if both the space of $\mathbf{C}$ and the function $E(\mathbf{C})$ are convex. For our problem, $\mathbf{C}$ is convex, but $E(\mathbf{C})$ is usually not. This can cause several problems for the algorithm. Firstly, the algorithm can converge to a local minimum that is not a global minimum (every local minimum of a convex function is a global minimum). If the initial guess $\mathbf{C}^0$ lies in the attraction region of a local minimum, then the algorithm will converge that way. Hence, the result can vary for different choices of the $\mathbf{C}^0$.

For the set of model parameterizations we treat here, f is most jagged in t_0^{parcel}, Δt_1^{crop} and Δt_2^{crop}. This is especially the case for Δt_2^{crop}. Δt_2^{crop} defines the ends of the growth season without a transition region. This means that as soon as $t_0^{parcel} + \Delta t_2^{crop}$ passes a measurement v_i, the model's estimation for that measurement will drop discontinuously to zero. As a result, small changes to Δt_2^{crop} do not change the error statistic when $t_0^{parcel} + \Delta t_2^{crop}$ lies in between two measurements. Therefore, the local derivative $\frac{\partial f}{\Delta t_2^{crop}}$ is zero almost everywhere. As a result, Δt_2^{crop} will almost surely converge within a single iteration.

For t_0^{parcel} and Δt_1^{crop} we prevented this by avoiding the common simplification that t_0^{parcel} and $t_0^{parcel} + \Delta t_1^{crop}$ coincide with a measurement. This was achieved for t_0^{parcel} in equation (3.10), where we defined the first interval of the growth season to start at t_0^{parcel} instead of the time of the last measurement before the growth phase. For Δt_1^{crop}, we explicitly defined a transition in equation (3.16).

However, even this improved implementation has a limitation. Because measurements are taken at a discrete set of times, the approximation of derivative $\frac{\partial f}{t_0^{parcel}}$ is, in almost all cases, only influenced by the measurement directly succeeding t_0^{parcel}. Therefore, $\frac{\partial f}{t_0^{parcel}}$ has a discontinuity whenever t_0^{parcel} coincides with a measurement. As a result, any measurement that is best modelled by the constant model before the growth season can form a local minimum for t_0^{parcel} if the subsequent measurement is best modelled by the first growth season. For example, t_0^{parcel} can converge to an isolated, seemingly good measurement, even though the measurement is followed by a set of measurements that conform badly to the growth model. However, because these subsequent measurements do not influence $\frac{\partial f}{t_0^{parcel}}$, they do not prevent convergence. The exact same logic holds for Δt_1^{crop}

These problems are mostly resolved with the differential evolution algorithm, which comes at the cost of a greater number of evaluations of f.

4.3 Differential evolution

4.3.1 Algorithm

Differential evolution [47] is an evolutionairy algorithm that creates new candidate solutions by combining existing ones. These candidate solutions are passed to the cost function and the algorithm keeps track of the best solution. The cost function is treated as a black box and can have any form. The differential evolution algorithm is given in pseudocode in algorithm 2.

Algorithm 2 Differential evolution. Modified after [47]. $CR \in [0, 1]$ and $F \in [0, 2]$ are chosen by the user. Clist is initialised with random samples of $\mathbf{C}$ selected with Latin hypercube sampling.

```
while not <<Termination criterion>> do
    for C in Clist do
        C1, C2, C3 ← random elements from Clist\C
        $k$ ← random ∈ $\{1, 2, ..., m\}$
        for each $i$ in $\{1, 2, ..., m\}$ do
            $r$ ← random number in $(0, 1)$
            if $r > CR$ or $i == k$ then
                $Cnew_i \leftarrow C1_i + F(C2_i - C3_i)$
            else
                $Cnew_i \leftarrow C_i$
            end if
        end for
        if $E(\mathbf{Cnew}) < E(\mathbf{C})$ then
            Replace C by Cnew in Clist
        end if
    end for
end while
```

4.3.2 Parameter choices and use case

Before initialisation, the parameters CR and F and the method for sampling the parameter space to generate the initial candidate solutions have to be chosen.

$CR \in [0, 1]$ is called the recombination constant. A low recombination constant means a slower, but more thorough search of the parameter space. As our problem is relatively smooth in most model parameters, the somewhat higher $CR = 0.7$ will be used.

$F \in [0, 2]$ is called the mutation constant. A low F speeds up convergence, but decreases the search radius. Storn and Price (1997) [47] recommend taking $F = 0.5$ initially and increasing it if premature convergence occurs. New developments since the initial publication by Storn and Prince have shown that allowing F to take a different random value at every generation significantly improves the performance of the algorithm [48, 49]. For this project, the "dithering" technique proposed by Dapak and Ludwig (2014) [49] will be used, where F is taken from a uniform distribution at every generation. Following the initial recommendation by Storn and Prince, F will be uniformly distributed in the interval $[0.5, 1]$.

Finally, the initial set of candidate solutions needs to be generated. The Latin hypercube sampling algorithm will be used to perform the sampling at initialisation. It requires a desired number of candidate solutions as well as finite bounds to each of the model parameters. The number of candidate solutions is generally recommended to scale with the dimensionality of the problem [47], so we will use $15M$ candidate solutions (where M is the dimensionality, i.e. the number of model parameters in $\mathbf{C}$). It is important to choose the finite bounds broadly enough so that the globally best solution is almost guaranteed to fall within the bounds, as the algorithm has very limited capabilities of searching outside of these bounds. For most parameters, the cost function increases steeply outside of the range of feasible solutions. Hence, candidate solutions will quickly converge towards the range of feasible solutions, even when they are initialized very far away due to a broad definition of bounds. As such, making these bounds extremely broad will not very considerably slow down convergence. Therefore, we will extend the bounds from equation (3.37) as follows:

$$
\begin{gathered}
0 < C_1^{crop} < 1, \\
0 < C_3^{crop}, C_4^{crop}, C_6^{crop} < 10^8, \\
0 < p_{g,0}^{crop} < 10^4, \\
-0.15 < C_2^{crop} < 0.15, \\
10^3 < C_5^{crop} < 10^3, \\
0 \leq rd_{max}^{crop} \leq \max_{i \in \{1,2,..,n\}} (rd(t_i)), \\
0 \leq h_{min}^{crop} \leq 1, \\
t_0^{parcel} \leq \text{July 17}, \\
\Delta t_1^{crop} \geq 15 \text{ days}, \\
\Delta t_2^{crop} \geq 45 \text{ days},
\end{gathered}
\tag{4.11}
$$

Here, the upper limit of rd_{max}^{crop} was set to the highest value for the rain deficit rd that occurred in the given year, as $rd_{max}^{crop} > \max_i(rd(t_i))$ is equivalent to $rd_{max}^{crop} = \max_i(rd(t_i))$. Large values for $rd(t_i)$ are in the order 10^1. Hence, $1 - \frac{rd(t_i)}{C_3^{crop}} \approx 1$ if $C_3^{crop} \geq 10^8$. Therefore, allowing larger values for C_3^{crop} will not significantly improve the results. The limits for $C_1^{crop}, C_2^{crop}, C_4^{crop}, C_5^{crop}$ and $p_{g,0}^{crop}$ were empirically estimated by applying non-linear least squares to potato parcels. Note that the limits of C_1^{crop} and C_2^{crop} make sense, as the RVI usually ranges between 2.4 and 3.2. Hence, differences between subsequent measurements are expected to be at most order 1.

4.4 The hybrid method

4.4.1 Algorithm

The error statistic E is actually smooth with a single, global minimum in many of its model parameters. For these parameters, non-linear least squares will perform much better than differential evolution. Hence, it makes sense to design a hybrid method that takes advantage of the properties of non-linear least squares for the parameters that are most suited for it, and use a differential evolution approach for the parameters that are not. Here, we will develop our own algorithm that does exactly this, and taylor it to our application.

We will achieve this by setting a set of parameters to a fixed value while performing one of the fit methods on the remaining parameters. By alternating between the two methods, using complementary (possible overlapping) parameter sets, a good estimate of the optimal solution can be achieved. The parameters are thus divided into three complementary, disjoint sets: $\mathbf{C}_{difev}$ for parameters that are best fitted with differential evolution only, $\mathbf{C}_{both}$ for parameters that get the best fit when non-linear least squares is applied using an initial estimate from differential evolution, and $\mathbf{C}_{nllsq}$ for parameters that are best fitted with non-linear least squares and that do not significantly benefit from (or are harmed by) an initial estimate from differential evolution. Note that differential evolution searches the entire parameter space, and therefore has no real use for an initial estimate from earlier iterations of either method.

Ideally, both methods would be alternatingly performed multiple times until some convergence requirement is achieved. However, to limit computation time, the computationally expensive differential evolution will be performed only once.

To make optimal use of the single differential evolution, a decent initial "guess" for $\mathbf{C}_{nllsq}$ is obtained with non-linear least squares first. The computation time of non-linear least squares is only weakly dependent on number of parameters. Hence, to improve the initial estimate for $\mathbf{C}_{nllsq}$, all parameters (i.e. $\mathbf{C}_{difev} \cup \mathbf{C}_{both} \cup \mathbf{C}_{nllsq}$) will be fitted in this first iteration.

Subsequently, differential evolution is applied on $\mathbf{C}_{difev} \cup \mathbf{C}_{both}$, while the parameters in $\mathbf{C}_{nllsq}$ remains fixed at the initial guess produced by the first non-linear least squares step. The bounds from equation (4.11) are used here.

Finally, the parameters in $\mathbf{C}_{difev}$ are fixed to the values obtained with differential evolution. A final non-linear least squares step is then performed on $\mathbf{C}_{nllsq} \cup \mathbf{C}_{both}$. In this final step, results for $\mathbf{C}_{nllsq}$ and $\mathbf{C}_{both}$ from respectively the first iteration of non-linear least squares and the differential evolution step, are used as initial estimates for each parameter. Using these estimates can speed up convergence and, in the case of $\mathbf{C}_{both}$, help non-linear least squares avoid local minima.

4.4.2 Parameter configuration

Through understanding of the model parameterizations and the error statistic, we can make a good a priori guess which parameters are suited and unsuited for a non-linear least squares approach.

Firstly, the phase boundaries t_0^{parcel}, Δt_1^{crop} and Δt_2^{crop} make a sharp transition from one phase to the next. In fact, as we described in section 4.2.2, the error function is constant for Δt_2^{crop} between measurements, with a sharp discontinuity at the measurements themselves. Though we made sure the error statistic is continuous in Δt_0^{parcel} and t_1^{parcel} (see section 4.2.2), the derivative of the error function still has a discontinuity at every measurement. Therefore, it will be very difficult for non-linear least square to converge properly for any of these parameters. We can conclude that t_0^{parcel}, Δt_1^{crop} and Δt_2^{crop} are almost certainly unsuited for fitting with non-linear least squares, and will therefore be set to a fixed value in the last step of the hybrid algorithm.

Secondly, the model parameterization is obviously smooth in C_1^{crop}, C_2^{crop}, C_4^{crop}, C_5^{crop}, C_6^{crop} and $p_{g,0}^{crop}$. With a little more work, one can see it is also smooth in h_{min}^{crop}: for each i and with fixed rd_{max}^{crop} and C_3^{crop}, the value $\left[\max\left(h_{min}^{crop}, 1 - \frac{rd(t_{i-1}) - rd_{max}^{crop}}{C_3^{crop}}(1 - h_{min}^{crop})\right)\right]$ increases linearly (from some value between 0 and 1) to 1 as h_{min}^{crop} goes from 0 to 1. Therefore, these seven parameters are likely best fitted with non-linear least squares.

Lastly, for the parameters C_3^{crop} and rd_{max}^{crop}, the model parameterization is neither completely smooth, nor obviously sufficiently jagged to make the a priori assumption that it can only be fitted with differential evolution. The derivative to C_3^{crop} has a discontinuity wherever $\frac{rd(t_{i-1}) - rd_{max}^{crop}}{C_3^{crop}} = 1$ for some i. However, the derivative to C_3^{crop} is some combination of all terms i for which $\frac{rd(t_{i-1}) - rd_{max}^{crop}}{C_3^{crop}} < 1$. Therefore, it is plausible that these discontinuities are relatively minor, and the model parameterization is smooth enough to get a good performance with non-linear least squares. Similarly, the derivative to rd_{max}^{crop} has a discontinuity wherever $rd_{max}^{crop} = rd(t_{i-1})$ for some i, in addition to the discontinuities at $\frac{rd(t_{i-1}) - rd_{max}^{crop}}{C_3^{crop}} = 1$. Again, the derivative to rd_{max}^{crop} is a combination, in this case of all terms i for which $rd_{max}^{crop} < rd(t_{i-1})$ and $\frac{rd(t_{i-1}) - rd_{max}^{crop}}{C_3^{crop}} < 1$. Hence, for both parameters, there is some hope that non-linear least squares gives a good performance, but it is equally plausible that differential evolution will be necessary to get a decent fit. Therefore, we will simply run tests with C_3^{crop} and rd_{max}^{crop} in each of the three options, $\mathbf{C}_{difev}$, $\mathbf{C}_{both}$ and $\mathbf{C}_{nllsq}$, to see which performs best.

Similarly, we will validate the a priori assumptions for the other 10 parameters by comparing the quality of the fits produced under this assumption with the quality of the fits produced with the given parameter in $\mathbf{C}_{both}$. For these tests, we shall use the 2019 data of the 1167 potato parcels in the validation region described in 2.5, rather than all (potato) parcels in the Netherlands, to reduce computation time. As we will show in section 5.3, the (in some sense) optimal parameter configuration is:

$$\begin{gathered} C_2^{crop}, C_3^{crop}, C_4^{crop}, rd_{max}^{crop}, p_{g,0}^{crop} \in \mathbf{C}_{nllsq} \\ t_0^{parcel}, \Delta t_1^{crop}, \Delta t_2^{crop}, C_5^{crop}, C_6^{crop} \in \mathbf{C}_{difev}. \end{gathered} \tag{4.12}$$

In addition, $C_1^{crop} \in \mathbf{C}_{nllsq}$ for linear p^{crop}, and $C_1^{crop} \in \mathbf{C}_{both}$ for bilinear p^{crop} ($\mathbf{C}_{both} = \varnothing$ in other cases). See respectively sections 8.2.1 and 8.2.2 for a discussion why $C_1^{crop} \in \mathbf{C}_{both}$ and $C_5^{crop}, C_6^{crop} \in \mathbf{C}_{difev}$ turned out to yield considerably better results.

5 Validation and optimization of the calibration methodology

This section contains the results of three validation steps designed to verify and optimize the hybrid calibration method developed in section 4.4. First, in section 5.1, we show that the hybrid calibration method yields superior calibrations to both differential evolution and non-linear least squares for all model parameterizations. Second, in section 5.2, we investigate the consistency of the hybrid method by comparing the results of multiple independent applications to the same data. Third, in section 5.3, we demonstrate that the parameter configuration we proposed in section 4.4.2 is an (in some sense) optimal trade-off between optimality of the results and computational expense.

In this section, we will be using histograms such as the one in figure 9 to compare the quality of the results of different approaches. These histograms display the relative difference in least squares error statistic (see equation (4.2)) of the results of two separate calibration attempts. Negative values mean that the algorithm on the left of the minus (see label x-axis) outperforms the other, and vice versa. This is a rather uncommon approach to quantify differences in algorithm performance (the author has not seen it before). More commonly employed are single-valued approaches such as mean or median error statistics, or number of parcels where one method outperforms the other.

The downside of statistics based on the median or number of parcels is that they are biased towards methods that perform slightly better in most cases, but yield a much more significantly inferior result on a (small or major) minority of parcels. This, for example, could be the case when comparing non-linear least squares to differential evolution on a function with multiple minima, where our initial guess is (slightly) more likely to fall within the region of attraction of the global minimum. Non-linear least squares will converge closer to the global minimum than differential evolution, but differential evolution is much less likely to get stuck in a local minimum.

On the other hand, a mean quality statistic can be biased towards methods with a small number of very large outliers. Plotting complete histograms will visualize such differences and allow one to be properly informed of trade-offs when making decisions.

5.1 Comparison between calibration methods

In section 4, we described three approaches to calibrating the model parameters in the model: non-linear least squares, differential evolution and the hybrid method. In this section, we will compare the performance of these calibration methods by comparing the least squares error statistic (equation (4.2)) of the fits generated by each method over a large number of parcels. To keep computation time to a manageable level, only the 2019 data of the 1167 potato parcels of the validation region (see section 2.5) were used.

The time used to calibrate the model parameterizations to these 1167 parcels is shown in table 3 for each of the methods. Clearly, non-linear least squares is considerably faster than both others, and the hybrid method considerably outperforms differential evolution in terms of computation time. The quadratic method is unexpectedly slow for differential evolution. It only contains four model parameters, compared to six for the exponential model. Clearly, this forms a bad case for differential evolution. We will propose an explanation and possible directions for improvement in section 8.2.2 of the discussion.

Table 3: Computation time of non-linear least squares (nnlsq), differential evolution (difev) and the hybrid method to calibrate the 1167 potato parcels in the validation region for each of the basic model parameterizations. The number of degrees of freedom (DOF) is also given. The computation time of the hybrid is further split up into its three steps (see section 4.4).

model parameterization	DOF	nllsq (s)	difev (s)	hybrid (nllsq 1, difev, nllsq 2) (s)
linear	2	107	1010	107 (107, -, -)
linear; t_0^{parcel} variable	3	136	1068	275 (133, 80, 62)
linear; h, t_0^{parcel} variable	4	264	2205	552 (290, 168, 94)
linear; rd_{max}^{crop}, t_0^{parcel} variable	4	187	1658	374 (187, 90, 97)
linear; rd_{max}^{crop}, h, t_0^{parcel} variable	5	303	3661	865 (413, 244, 208)
linear; Δt_2^{crop}, t_0^{parcel} variable	4	177	2973	789 (169, 534, 86)
bilinear; t_0^{parcel} variable	5	289	3074	1891 (280, 1523, 88)
exponential; t_0^{parcel} variable	6	926	8589	1597 (933, 527, 137)
quadratic; t_0^{parcel} variable	4	190	9896	7246 (196, 6998, 52)

Figure 9 shows the relative difference between the error statistics for the simple case p^{crop} and g linear and all other parameters fixed. This model parameterization only contains model parameters C_1^{crop} and C_3^{crop}, both of which are in $\mathbf{C}_{nllsq}$, so the hybrid method is equivalent to non-linear least squares for this case. Therefore, only the comparison between differential and non-linear least squares is made. Interestingly, non-linear least squares yields consistently better results than differential evolution for this model. This demonstrates that C_1^{crop} and C_3^{crop}, are properly placed in $\mathbf{C}_{nllsq}$.

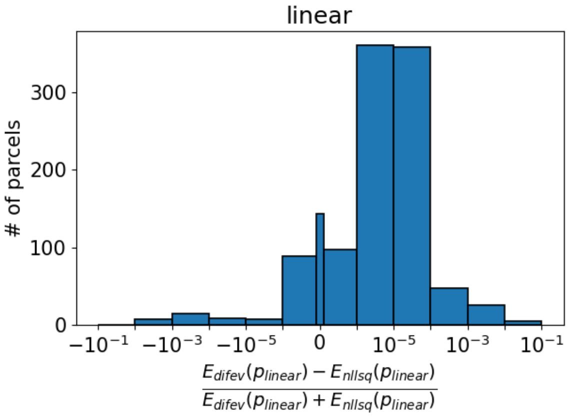

Figure 9: Comparison between the performance of differential evolution (difev) and non-linear least squares (nllsq) for the model parameterization with p^{crop} and g linear, all other model parameters fixed. The x-axis shows the relative difference in error statistic of the calibration result of both methods. The middle, thinner bar contains values within 10^{-9} of zero, reflecting parcels where there was no significant difference in fit quality. The relative difference is mostly positive, showing that non-linear least squares outperforms differential evolution on this model.

Figure 10 shows a comparison of the performance between the hybrid method and respectively differential evolution (left) and non-linear least squares (right), for the model parameterization with g and p^{crop} linear with only t_0^{parcel} variable (top), and for the same model parameterization with also t_1^{crop} variable. To keep this section concise, only the figures of two of the remaining basic model parameterizations are included in this section, see figure 10. Similar figures for the rest of the basic model parameterizations are included in appendix A.1.

The function for t_0^{parcel} was included because it nicely illustrates the behaviour of the rest of the model parameterizations. In all model parameterizations, the hybrid method outperforms non-linear least squares on almost all parcels. This can be seen in figures 10b and 10d, where the bars on the right of zero are all close to zero. These bars indicate the parcels where non-linear least squares gave a better result than the hybrid method, which almost never happens.

Figure 10a shows that the hybrid method and differential evolution give very similar performance for this model parameterization. Both give a better result than the other on approximately half the parcels. For the model parameterizations in appendix A.1 all give either similar results, or the hybrid method (significantly) outperforms differential evolution.

The only exception is the model parameterization including Δt_2^{crop}, as depicted in figure 10c. Though the results are again pretty similar, large differences in quality $\left(\frac{|E_{hybrid}-E_{difev}|}{E_{hybrid}+E_{difev}} > 10^{-2}\right)$ are actually slightly more commonly in favor of differential evolution than vice versa. An explanation of why this is so is presented in section 8.2.1 of the discussion.

Even so, the performance of differential evolution is only slightly better than that of the hybrid method. Therefore, it is unlikely to be worth the nearly four fold increase in computational complexity (see table 3). Hence, we can conclude that the hybrid method is the most suitable method for the calibration of the model.

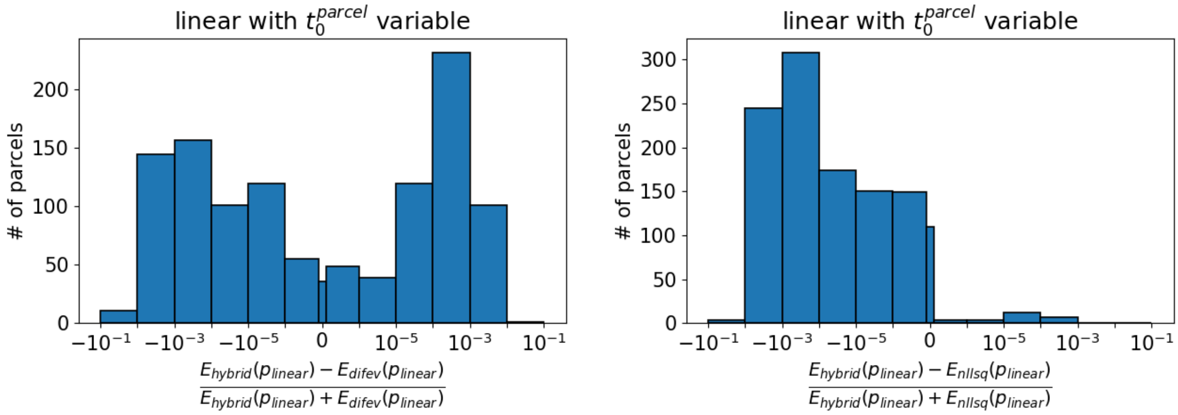

(a)

(b)

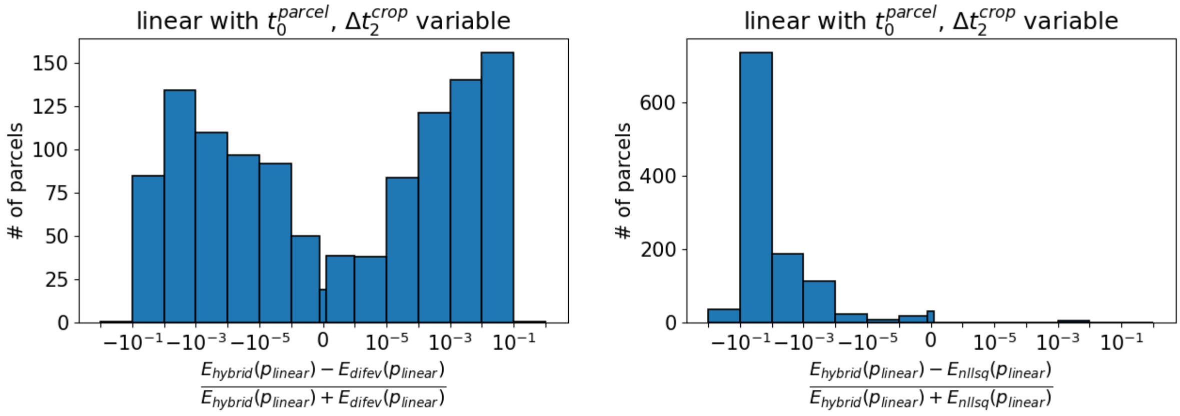

(c) *(d)*

Figure 10: Comparison between the performance of the three calibration methods for two of the basic model parameterizations. In each row, the left and right subfigures show the relative difference in error statistics respectively between the hybrid method and differential evolution and between differential evolution and non-linear least squares. The 2019 data from the 1167 potato parcels in the validation region described in section 2.5 was used for these images. The middle, thinner bar contains values within 10^{-9} *of zero, reflecting parcels where there was no significant difference in fit quality. Similar images for the other basic model parameterizations are given in appendix A.1.*

5.2 Consistency of the hybrid calibration method

In the previous section, we found that the hybrid method gives a much better performance than either of the other methods. To get a measure for the consistency of the results of the hybrid method, the algorithm can be executed twice on the same data set. The variance in the error statistic can be used to estimate the confidence level that a calculated result is the optimal one. In addition, this gives a measure for the base variation in the algorithm's outcome. This will help to interpret the results of the next subsection, where we validate the parameter configuration of the hybrid method.

The results of the variation in error statistic between two executions of the hybrid method are shown in figure 11. One figure was made for each of the basic model parameterizations; i.e. one for each the four forms of p^{crop} and g as well as for each of the model parameters h_{min}^{crop}, rd_{max}^{crop} and Δt_2^{crop}. As expected, model parameterizations with more parameters show greater variation as it becomes more difficult to search the higher dimensional parameter space. Especially the results using Δt_2^{crop}, a bilinear or quadratic model parameterization (figures 11d, 11e and 11f), and, to a lesser extent, the exponential model parameterization (figure 11f) seem unstable. An explanation of why this is likely so is presented for each case in the subsection of section 8.2 of the discussion.

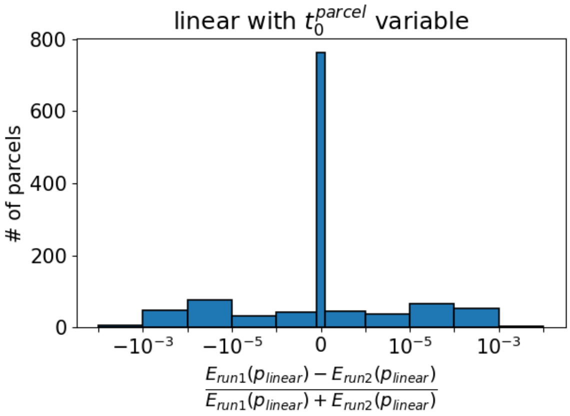
linear with t_0^{parcel} variable
# of parcels
800
600
400
200
0
-10^{-3}
-10^{-5}
0
10^{-5}
10^{-3}
$\frac{E_{run1}(p_{linear}) - E_{run2}(p_{linear})}{E_{run1}(p_{linear}) + E_{run2}(p_{linear})}$

(a)

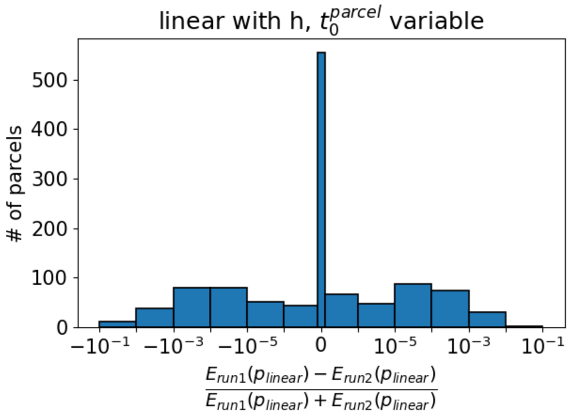
linear with h, t_0^{parcel} variable
# of parcels
500
400
300
200
100
0
-10^{-1}
-10^{-3}
-10^{-5}
0
10^{-5}
10^{-3}
10^{-1}
$\frac{E_{run1}(p_{linear}) - E_{run2}(p_{linear})}{E_{run1}(p_{linear}) + E_{run2}(p_{linear})}$

(b)

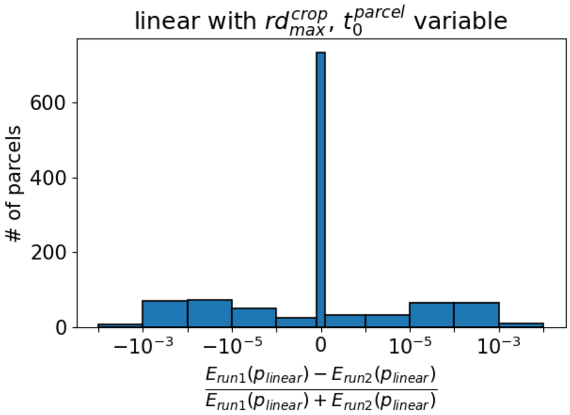
linear with rd_{max}^{crop}, t_0^{parcel} variable
# of parcels
600
400
200
0
-10^{-3}
-10^{-5}
0
10^{-5}
10^{-3}
$\frac{E_{run1}(p_{linear}) - E_{run2}(p_{linear})}{E_{run1}(p_{linear}) + E_{run2}(p_{linear})}$

(c)

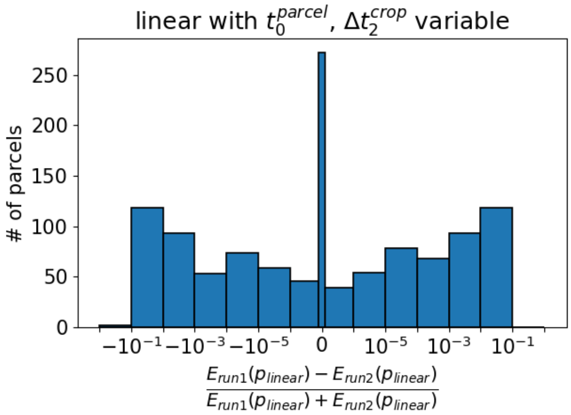
linear with t_0^{parcel}, Δt_2^{crop} variable
# of parcels
250
200
150
100
50
0
-10^{-1}
-10^{-3}
-10^{-5}
0
10^{-5}
10^{-3}
10^{-1}
$\frac{E_{run1}(p_{linear}) - E_{run2}(p_{linear})}{E_{run1}(p_{linear}) + E_{run2}(p_{linear})}$

(d)

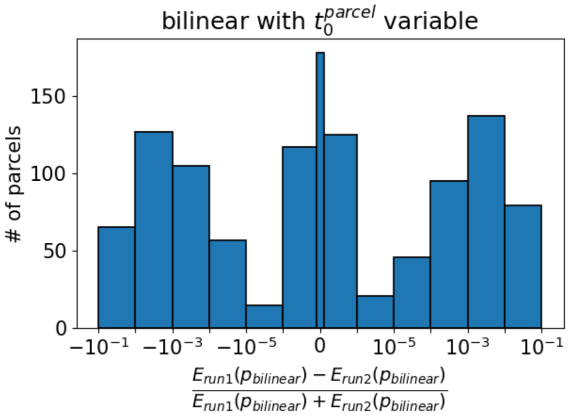
bilinear with t_0^{parcel} variable
# of parcels
150
100
50
0
-10^{-1}
-10^{-3}
-10^{-5}
0
10^{-5}
10^{-3}
10^{-1}
$\frac{E_{run1}(p_{bilinear}) - E_{run2}(p_{bilinear})}{E_{run1}(p_{bilinear}) + E_{run2}(p_{bilinear})}$

(e)

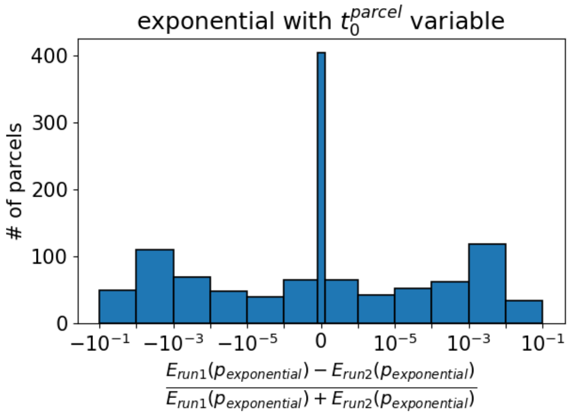
exponential with t_0^{parcel} variable
# of parcels
400
300
200
100
0
-10^{-1}
-10^{-3}
-10^{-5}
0
10^{-5}
10^{-3}
10^{-1}
$\frac{E_{run1}(p_{exponential}) - E_{run2}(p_{exponential})}{E_{run1}(p_{exponential}) + E_{run2}(p_{exponential})}$

(f)

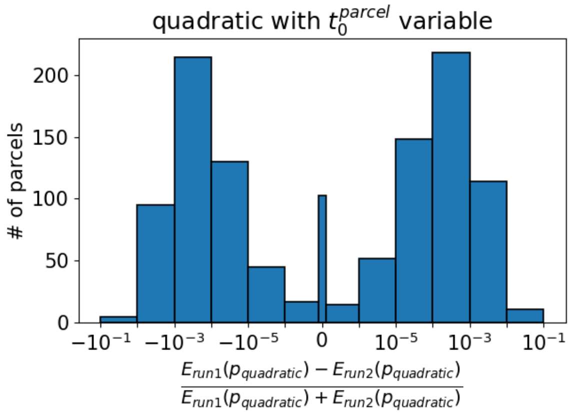

(g)

Figure 11: Relative difference in error statistic between two iterations of the hybrid method. The 2019 data from 1167 potato parcels in the validation region described in section 2.5 was used for these images. The fits were made with the model parameterization indicated in the title of each figure. The middle, thinner bar contains values within 10^{-9} *of zero, reflecting parcels where there was no significant difference in fit quality between the two iterations.*

5.3 Validating the parameter configuration of the hybrid method

This section contains a comparison between the parameter configuration for the hybrid method we proposed in section 4.4.2, and a configuration where one of the parameters was moved to $\mathbf{C}_{both}$. C_1^{crop} is treated separately for the linear and bilinear model parameterizations, because its fitting behaviour is considerably different in a two-phase model compared to the single-phase linear p^{crop}. For the more complicated cases of $C_3^{crop}, rd_{max}^{crop}, C_5^{crop}$, C_6^{crop} and C_1^{crop} in the bilinear and exponential case, a full comparison between $C \in \mathbf{C}_{nllsq}$, $C \in \mathbf{C}_{difev}$ and $C \in \mathbf{C}_{both}$ has been included. To avoid bloating this section, a large part of the (less interesting) figures is contained in appendix A.2.

Figure 12 shows several figures for the comparison between the default parameter configuration and one with one parameter moved to $\mathbf{C}_{both}$. The parameters $h_{min}^{crop}, \Delta t_2^{crop}, \Delta t_1^{crop}, C_4^{crop}, p_0^{crop}$ and C_1^{crop} (linear case) all result in histograms approximately symmetrical around zero. One example is show in figure 12a. This means that the performance of these parameters is similar in their proposed configuration and in $\mathbf{C}_{both}$. A such, the proposed configuration can be considered optimal for these parameters, as additional parameters in $\mathbf{C}_{both}$ result in an increase in computation time, especially for the parameters originally in $\mathbf{C}_{nllsq}$.

The cases $t_0^{parcel} \in \mathbf{C}_{difev}$ (figure 12b) and $C_2^{crop}, p_0^{crop} \in \mathbf{C}_{nllsq}$ (figures 12c and 29f of appendix A.2) actually give a better performance than in $\mathbf{C}_{both}$. t_0^{parcel} is such a bad case for non-linear least squares that the algorithm has more trouble converging to the optimum when it is given an initial guess for t_0^{parcel} close to the optimum than when it is simply kept fixed. On the other hand, $C_2^{crop}, p_0^{crop} \in \mathbf{C}_{both}$ does not actually hamper the quality of the estimate of C_2^{crop} or p_0^{crop} itself. After all, the last non-linear least squares is still performed, but it now uses an estimate generated by differential evolution, which is very unlikely to be a significant detriment to its quality. Instead, the addition of one extra dimension in the parameter space of differential evolution makes it more difficult for it to converge to the global optimum. As a result, the other parameters calibrated in the differential evolution step get an inferior estimate for part of the parcels.

For exponential p^{crop}, we see that $C_2^{crop} \in \mathbf{C}_{both}$ (figure 12d) yield a better quality than $C_2^{crop} \in \mathbf{C}_{nllsq}$. Note that the relatively large variation in error statistic (i.e. few values around zero and a peak around

10^{-2} on both sides) is an inherent quality of these models, as shown in section 5.2. For this parameter, there is a trade-off between quality of the result and computation time. Depending on how important computational complexity is, one might opt for the (slight) improvement in quality that is obtained with $C_2^{crop} \in \mathbf{C}_{both}$. However, this methodology is designed for usage on the 260 thousand parcels in Netherlands, so the considerable increase in computation time is not worth the rather limited improvement in quality. Hence, opted for $C_2^{crop} \in \mathbf{C}_{nllsq}$ in this thesis project.

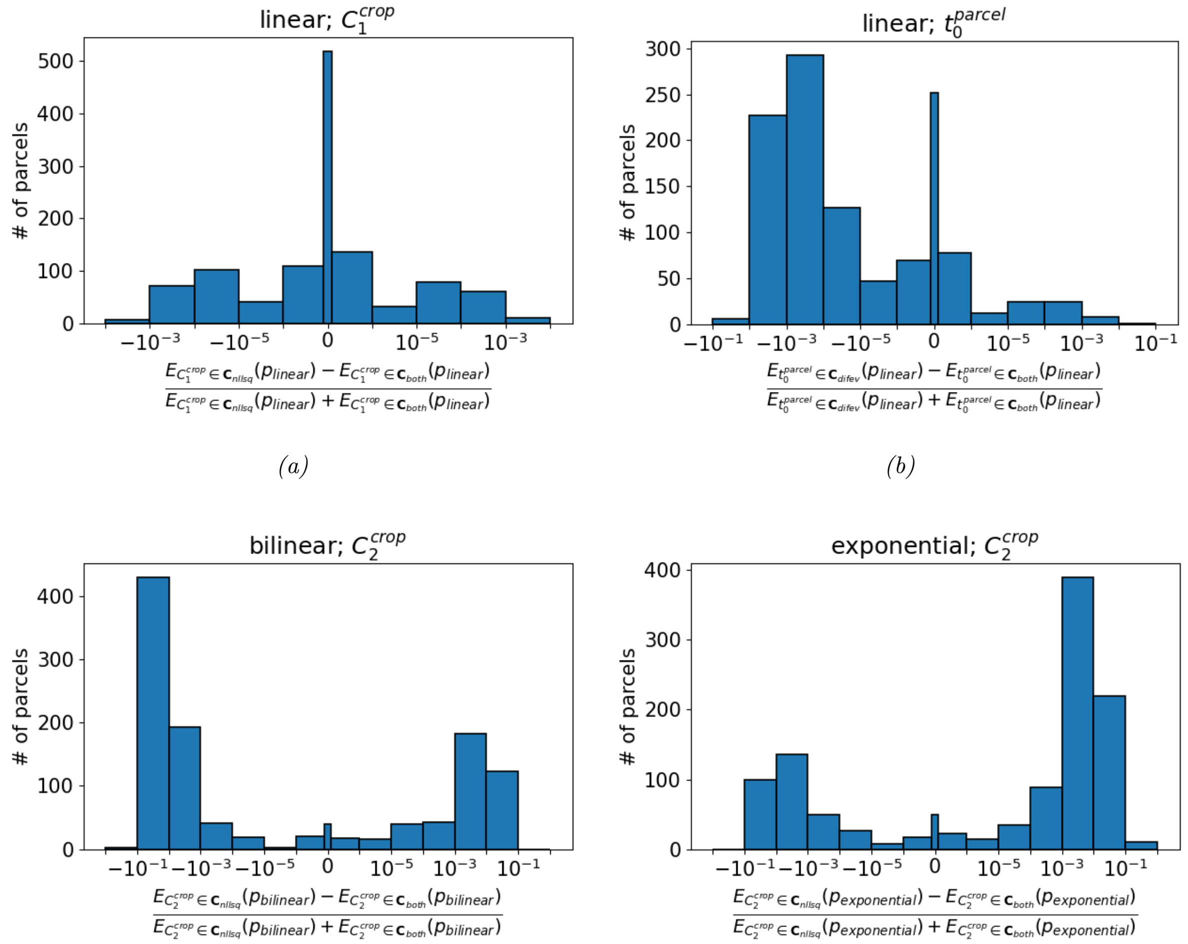

(a) *(b)*

(c) *(d)*

Figure 12: Validation of the parameter configuration (i.e. the choice of sub-algorithm used to fit each parameter within the hybrid method) of the hybrid method for the model parameters C_1^{crop} *(with linear* p^{crop}*),* t_0^{parcel} *and* C_2^{crop}*. Similar figures for* $C_4^{crop}, p_{g,0}^{crop}, \Delta t_1^{crop}$ *and* Δt_2^{crop} *are given in figure 29 of appendix A.2. Each subfigure shows an investigation of the configuration of one model parameter* $C \in \mathbf{C}$*. The x-axis shows the relative difference between the error statistics of fits generated by the hybrid method with* $C \in \mathbf{C}_{both}$ *and either* $C \in \mathbf{C}_{nllsq}$ *or* $C \in \mathbf{C}_{difev}$*, depending on the a priori guess formulated in section 4.4.2 (see label in the x-axis). The 2019 data from 1167 potato parcels in the validation region described in section 2.5 was used for these images. The basic model parameterizations were used for this investigation, i.e.* t_0 *was fitted in each figure, but the models were otherwise kept in the simplest form that included the relevant parameter. In each histogram, negative values signify that the a priori assumption gave a better result than* $C \in \mathbf{C}_{both}$*, whereas positive values signify the opposite. The middle, thinner bar contains values within* 10^{-9} *of zero, representing parcels where there was no significant difference in fit quality.*

A similar, but more elaborate investigation is made for the parameters C_3^{crop} (bilinear and exponential case), $C_3^{crop}, rd_{max}^{crop}, C_5^{crop}$ and C_6^{crop} in figure 13 and figure 30 of appendix A.2. In these figures, every row of two subfigures is dedicated to a single parameter $C \in \mathbf{C}$. The subfigures on the right compare the quality of the results for $C \in \mathbf{C_{difev}}$ with $C \in \mathbf{C_{nllsq}}$, where negative values mean $C \in \mathbf{C_{difev}}$ is outperforming $C \in \mathbf{C_{nllsq}}$. The subfigures on the left compare the quality of the results for $C \in \mathbf{C_{both}}$ with $C \in \mathbf{C_{difev}}$ where negative values mean $C \in \mathbf{C_{both}}$ is outperforming $C \in \mathbf{C_{difev}}$.

C_3^{crop} and rd_{max}^{crop} are performing approximately equally in all cases. Therefore, $C_3^{crop}, rd_{max}^{crop} \in \mathbf{C_{nllsq}}$ is most suitable as that results in the lowest computational complexity.

Figure 13b shows that C_1^{crop} with bilinear p^{crop} gives considerably superior performance in $\mathbf{C_{difev}}$ than in $\mathbf{C_{nllsq}}$. An even better performance is achieved with $C_1^{crop} \in \mathbf{C}_{both}$, as show in figure 13a. Clearly, C_1^{crop} has to be calibrated in at least the differential evolution step to get a decent performance. Furthermore, calibrating one additional parameter in the non-linear least squares step does not have a significant impact on computational complexity. Therefore, $C_1^{crop} \in \mathbf{C}_{both}$ is the best choice, as we already claimed in in equation (4.12). An explanation of why $C_1^{crop} \in \mathbf{C}_{nllsq}$ gives poor performance is given in section 8.2.1.

Figure 13d shows that C_5^{crop} gives hugely better performance in $\mathbf{C_{difev}}$ than in $\mathbf{C_{nllsq}}$. In addition, figure 13c shows a slightly better performance for $C_5^{crop} \in \mathbf{C}_{difev}$ than $C_5^{crop} \in \mathbf{C}_{both}$. A very similar result is obtained for C_6^{crop} in figures 30e and 30f. This validates the claim in equation (4.12), that $C_5^{crop}, C_6^{crop} \in \mathbf{C}_{difev}$ is the most optimal choice. This result was unexpected, because as described in section 4.4.2, we thought the error statistic would be mostly smooth with few minima, which should imply that non-linear least squares gives a good performance. Yet, these results demonstrate the opposite. An explanation of this is given in section 8.2.2.

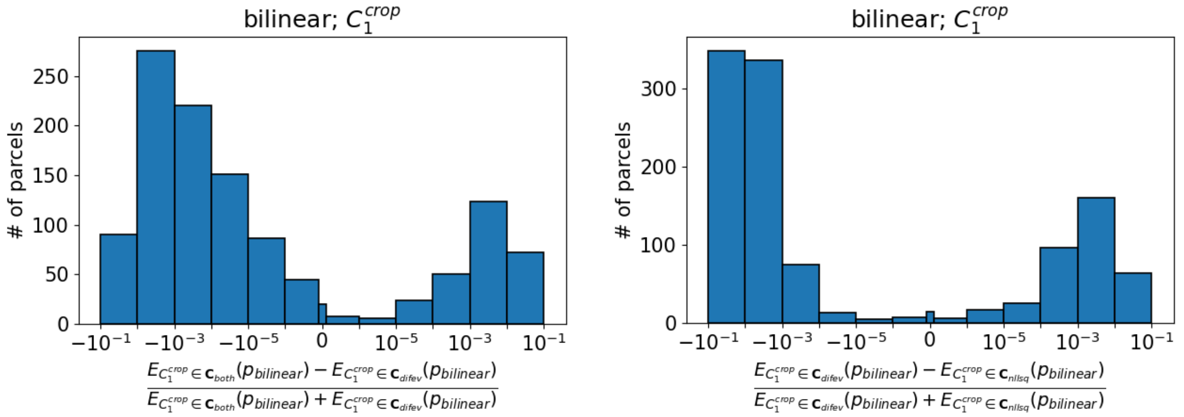

(a) *(b)*

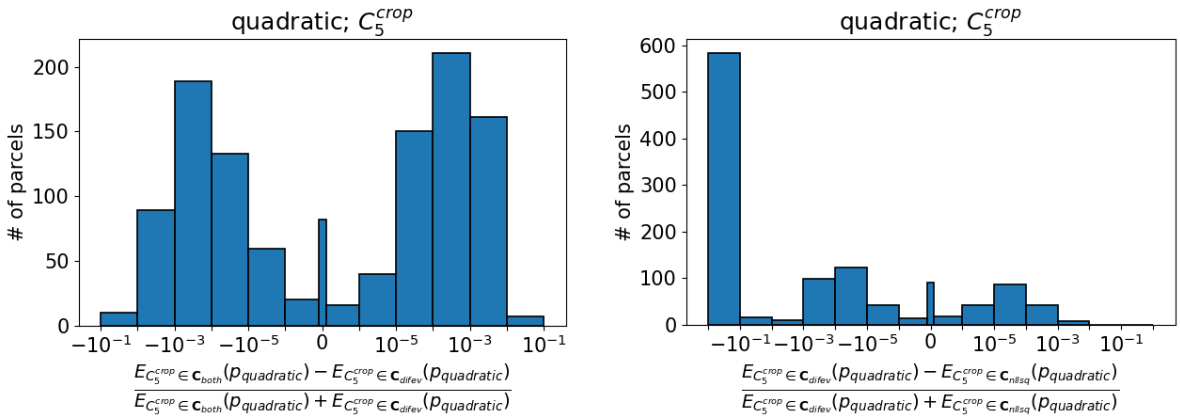

(c) *(d)*

Figure 13: Investigation of the parameter configuration (i.e. the choice of sub-algorithm used to fit a given parameter within the hybrid method) of the hybrid method for the more convoluted model parameters C_1^{crop} (with bilinear p^{crop}) and C_5^{crop}. Similar figures for $C_3^{crop}, rd_{max}^{crop}$ and C_6^{crop} are given in figure 30 of appendix A.2. Each row of two subfigures shows an investigation of the configuration of one these model parameters $C \in \mathbf{C}$. The x-axis shows the relative difference between the error statistics of fits generated by the hybrid method with $C \in \mathbf{C}_{both}$ and $C \in \mathbf{C}_{difev}$ (left), and between $C \in \mathbf{C}_{difev}$ and $C \in \mathbf{C}_{nllsq}$ (right). The 2019 data from 1167 potato parcels in the validation region described in section 2.5 was used for these images. t_0 was fitted in all figures, but the fits were otherwise kept in the simplest form that included the relevant parameter. In each histogram, negative values signify that $C \in \mathbf{C}_{both}$ gives better performance than $C \in \mathbf{C}_{difev}$ (left) or that $C \in \mathbf{C}_{difev}$ gives better performance than $C \in \mathbf{C}_{nllsq}$ (right), whereas positive values signify the opposite. The middle, thinner bar contains values within 10^{-9} of zero, representing parcels where there was no significant difference in fit quality.

6 Assessing to what extend model features reflect the behaviour of the RVI

In this section, The different features of the model will be investigated on whether they properly model the behaviour of the RVI. To this end, a good visualisation of the RVI time series can be very useful. Unfortunately, a simple plot of the (normalized) RVI is chaotic and noisy, even when averaged over a large set of parcels. An example of this was presented in figure 7. Only near the very end of this thesis project did we manage to develop a better method to visualize this. We achieved this by smoothing the time series specifically over the orbits. To be more precise, a smoothed time series is generated by taking the average of interpolated (normalized) RVI values of each orbit. Note that this smoothing is purely used in visualisation, and not during the calibration.

This works surprisingly well. A smoothed time series reveals clear patterns in the RVI that have obvious correlations with the cumulative rain deficit. This visualisation would have actually been useful during the development of the model, but unfortunately, we only formulated this approach after generating most of the results. As such, this section will start with an analysis of the smoothed time series of normalized RVI measurements, to see what can be learned in terms of model formulation. Subsequently, in section 6.2, we will investigate the contribution to the quality of the fit of the various model extensions.

6.1 Average behaviour all parcels

In figure 14, the smoothed normalized RVI time series of each year is plotted, along with the 6-day cumulative rain deficit. These images make four phenomena clearly visible.

The first phenomenon is the significant drop in RVI in the first month after mid-March. In the formulation of the model, the definition of v_0 rested on the assumption that the parcels are empty before the growth season. This would imply that the RVI is at a zero-measurement level before the growth season, increasing from that level as the growth season advances. Obviously, this assumption was naive. In reality, most fields are covered by a catch crop during most of the winter [50]. The drop in RVI is most likely caused by the destruction of the catch crop before the start of the growth season.

This can cause problems in several aspects of our modelling. Firstly, h_g^{crop} was defined (equation (3.7)) under the assumption that $v_{i-1} - v_0 > 0$. As this is clearly not the case, this has consequences for the fit of h_{min}^{crop}, as will be investigated in more detail in section 7.2. Secondly, the quadratic and exponential models include an estimate of $p^{crop}(t_{i-1})$, which assumes positivity of $v_{i-1} - v_0$ (equation 3.30). For negative $v_{i-1} - v_0$, the exponential and quadratic models reduce to the bilinear and linear model respectively (see equations (3.31) and (3.35)), where $p_{g,0}^{crop}$ and C_6^{crop} take the role of growth constant C_1^{crop}.

In addition, the drop in RVI makes the start of growth season t_0^{parcel} very important. In the models we defined without t_0^{parcel}, the entirety of the measurements are assumed to be part of the growth season (or until the end of the growth season if Δt_2^{crop} is included). This means the drop in RVI will be included, which will heavily bias the fit of growth constant C_1^{crop} towards zero (negative C_1^{crop} is not allowed). This is not the behaviour we want to model with C_1^{crop}. Therefore, t_0^{parcel} should be part of any model to avoid this period.

The second phenomenon is the very clear correlation with rain deficit. Every time the rain deficit drops to near-zero, the RVI either increases, often rapidly, or a downward trend is momentarily abated. Given this, it seems that the scaling factor $h^{crop}(rd(t))$ is actually a very important part of the system. Unfortunately, due to the mostly negative $v_{i-1} - v_0$, $h^{crop}(rd(t))$ is not yet able to properly model this behaviour of RVI. Sections 8.3.1 and 8.3.3 will go into more detail how the methodology can be improved to make full use of h^{crop} to accurately model the rain deficit-driven oscillations in RVI.

Thirdly, there does not seem to be a very significant growth. In each time series, increases in RVI almost exclusively occur at drops in the rain deficit. When the rain deficit increases again, the RVI drops back to close its original value. Any long-term increase in RVI is dwarfed by the magnitude of the bumps caused by the fluctuating rain deficit. This is bad news for the model developed in this thesis, as most of it is dedicated to modelling this apparently insignificant growth in RVI. A similar lack of growth can be found in the time series of corn, see appendix B.2. Section 8.1.2 contains a more elaborate discussion of what this means for the model.

Fourthly, no indication of harvest is visible. Remember that we intentionally end the time series at the end of August to avoid the harvest (see section 2.7). This means that including end of growth season Δt_2^{crop} in the model should not be necessary. Even so, we will still include some basic processing with Δt_2^{crop} in the next subsection.

Appendix B.1 includes similar time series separated by irrigated or non-irrigated according to the validation data of 2018, 2019 and 2020. Peculiarly, there seem to be no very significant differences between the RVI time series of irrigated and non-irrigated parcels. We will discuss this in more detail in section 8.1.3.

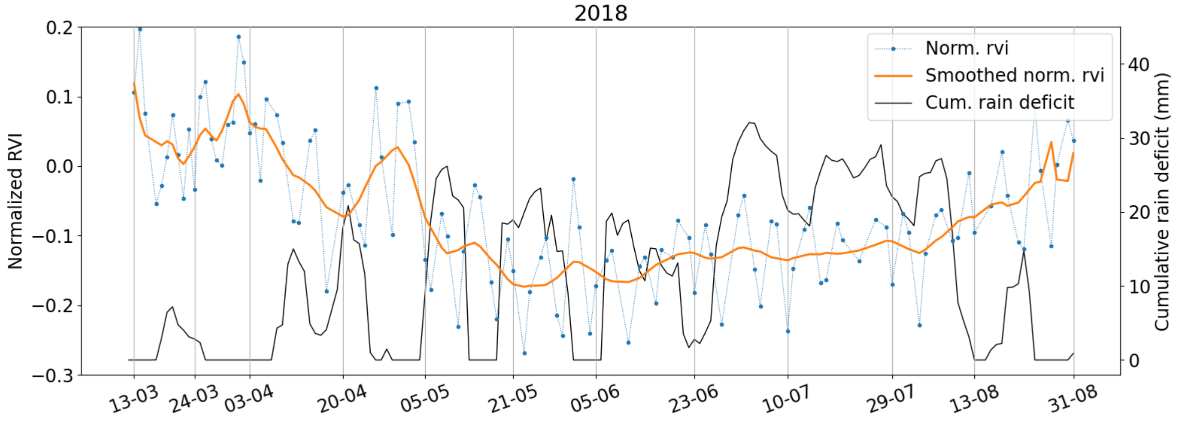

(a)

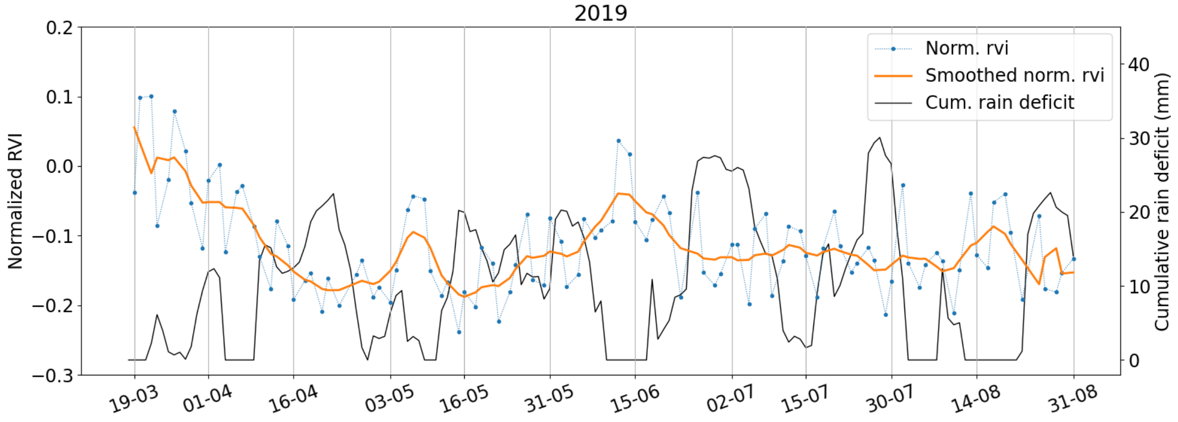

(b)

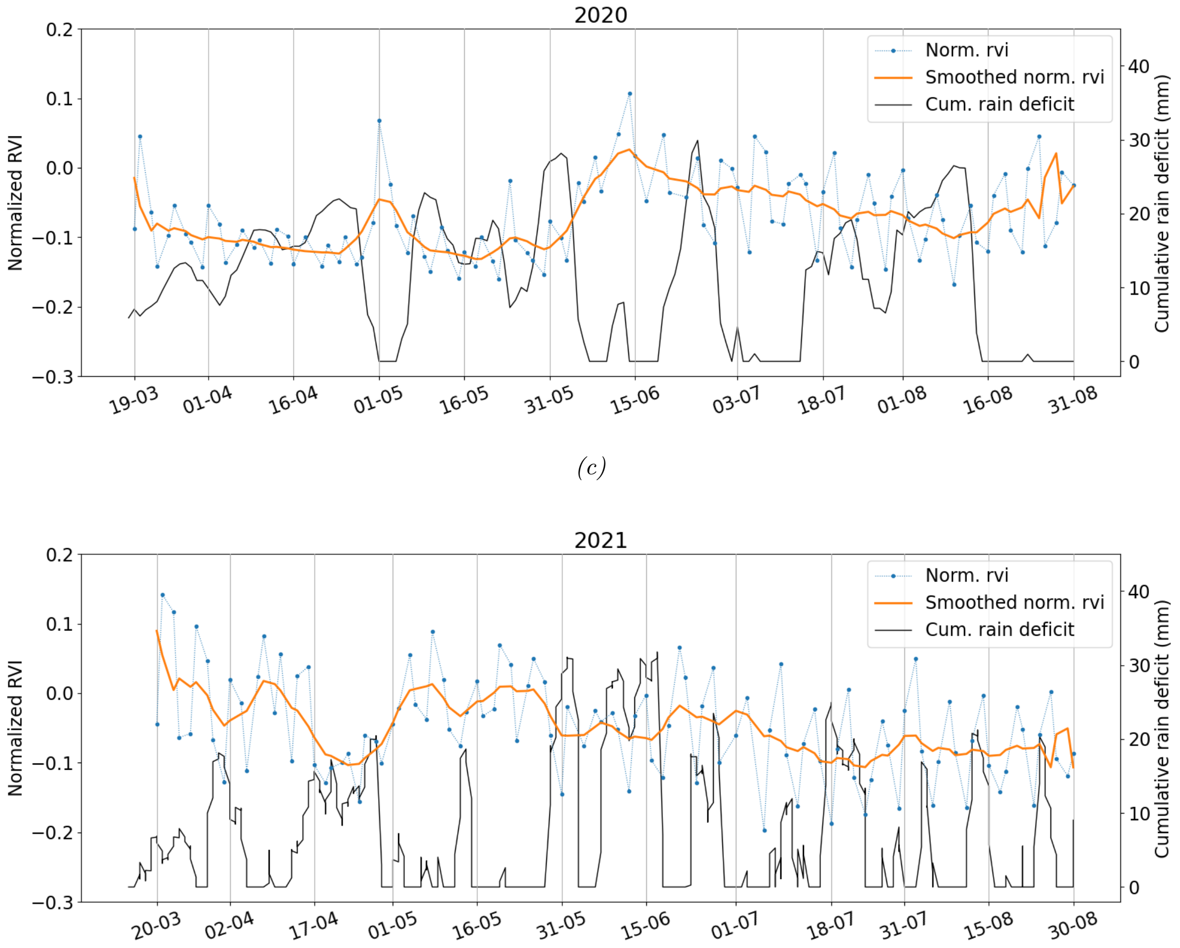

(c)

(d)

Figure 14: Average time series over all potato parcels in the validation region for each year.

6.2 Comparison between model parameterizations

In this section, we investigate how the various features of the different model parameterizations contribute to modelling the behaviour of the RVI. To this end, scatter plots were made to correlate quality improvement obtained with a certain model extension with the values of the parameters it introduces. This visualizes consistency and magnitude of the improvements, as well as trends where certain values of the parameters tend to imply better quality of the fit. The latter is useful, because it can be used to identify features in the RVI time series that causes the behaviour of the model. Furthermore, it can give an indication that the quality improvement is the result of overfitting rather than a reflection of system behaviour.

Appendix A.3 contains the scatter plots for the quadratic and exponential model, along with a short explanation. These were excluded from the main text as their results are heavily skewed by the mostly negative RVI, as we explained in section 6.1. For the other basic model parameterizations, the scatter plots are given in figure 15.

In figure 15a, we see that t_0^{crop} yields a small (compared to, for instance, the improvement with t_0^{crop}, see figure 15d), but consistent and significant, improvement in quality. 353 out of the 362 parcels that yield no improvement (quality difference smaller than 10^{-7}) compared to the base function have

$C_1^{crop} < 10^{-7} \approx 0$. Such a small C_1^{crop} implies that there is no significant difference in the model before and after t_0^{parcel}.

The parcels that do yield an increased quality with t_0^{parcel} form two clusters: one before 1 May, and one between 12 May and 9 June. These correlate precisely with the periods of high rain deficit in 2019, as well as the corresponding dips in RVI, see figure 14b. This makes sense: after t_0^{parcel}, the model predicts growth, so the optimal fit is obtained with t_0^{parcel} right before the increase in RVI coupled with the low rain deficit periods. This also demonstrates that t_0^{parcel} achieves the main reason we included it in the model: avoiding the RVI drop in the first month of the measurements.

Figure 15b shows that the calibration converges to $h_{min}^{crop} = 1$ for most parcels. However, there is a cloud of 337 parcels where $h_{min}^{crop} < 0.99$ yields a considerable improvement in quality. In section 7.2, we will investigate what makes these parcels unique, and explain why $h_{min}^{crop} = 1$ is optimal for the majority of parcels .

Similarly, for the model including rd_{max}^{crop} (figure 15c), roughy half the parcels either show no improvement (line in the middle), and/or converge to $rd_{max}^{crop} = 0$, which is equivalent to fitting no rd_{max}^{crop} at all. Slightly under half the parcels actually show an improvement in quality with a non-zero rd_{max}^{crop}. However, these parcels do not cluster around a single value of rd_{max}^{crop}, even though we would expect potato parcels to behave similarly in this aspect. In addition, the improvement in quality is not very large, compared to, for instance, the improvement that can be obtained with h_{min}^{crop} for some of the parcels, see figure 15b. Combining these clues, we conclude that the improvement obtained with rd_{max}^{crop} is more likely caused by overfitting than an actual reflection of system behaviour.

Figure 15d demonstrates that adding Δt_2^{crop} to the model gives a consistent and considerable improvement to the quality of the fit. However, a very high density of "improved" fits lie just above the lower bound at $\Delta t_2^{crop} = 45$. This means that only a very short part of the time series is fitted with the growth model. The remaining rest gets estimated as constant. Looking at figure 14b, this makes sense. The last two months of the RVI measurements do not contain a significant growth. Therefore, it fits the constant model quite well. On the other hand, the most significant growth happens before the peak around 15 June. Hence, the 30 to 60 day period before that is a good fit to the growth model. This is the reason why most parcels are best calibrated with Δt_2^{crop} between 45 and 60 days. Clearly, Δt_2^{crop} is not actually used to fit the end of the growth season, but rather the greatest peak in rain deficit-dependent RVI fluctuations.

Lastly, scatter plots for t_1^{crop} and C_2^{crop} of the bilinear model are shown in figures 15e and 15f. This model gives an even more dominant improvement than Δt_2^{crop}. However, the mechanism is similar. Δt_1^{crop} is very close to its minimum of 15 days. In addition, C_2^{crop} is negative for most parcels, which happens to be a good fit for the drop in RVI after the peak around 15 June. Clearly, the model is calibrated towards the fluctuations in RVI rather than actual growth of the crops. However, that does not mean that this gives no valuable information. After all, the magnitude of these oscillations can be an indicator of irrigation and other environmental factors. Therefore, we will further analyze the results of the bilinear model parameterization in section 7.3.

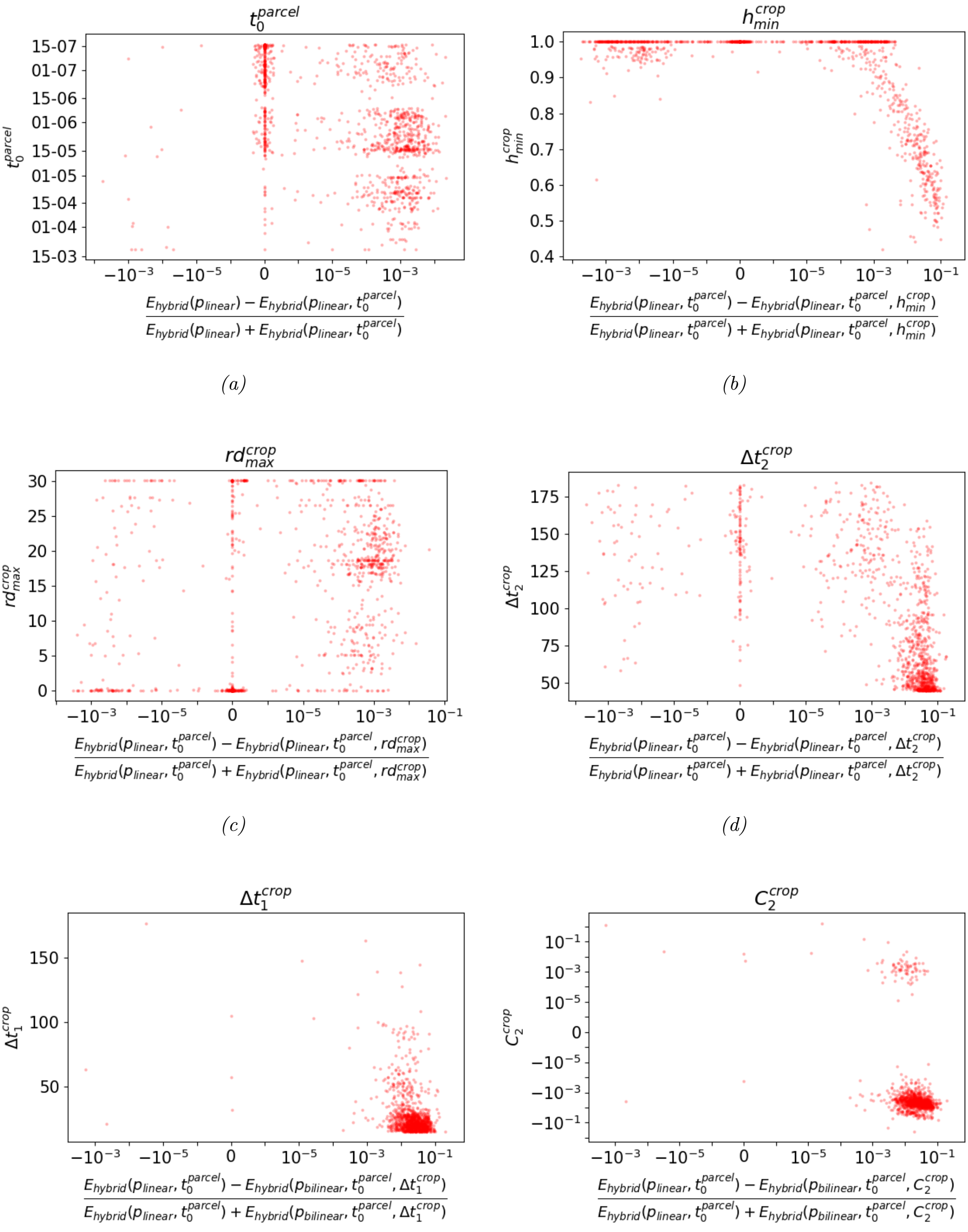

(a) *(b)*

(c) *(d)*

(e) *(f)*

Figure 15: Comparison of the performance of the basic model parameterizations. Similar figures for the exponential and quadratic model parameterizations are given in appendix A.3. Each parameterization is compared to the base case (p^{crop} and g linear, t_0^{crop} variable and all other parameters fixed). The quality improvement obtained with a certain model extension is plotted against the value of the parameters that it introduces. This way, any correlations between improved quality and the value of the model parameters is visualised.

7 Clustering parcels

In the previous two sections, we validated the calibration method and analyzed the relationship between the various model features and the behaviour of the RVI. In this section, we will be studying the scatter plots of different model parameter combinations to identify meaningful clusters. In this context, a cluster can be considered meaningful if it is caused by any kind of difference in system behaviour. In principle, clusters could exist in any combination of a model's model parameters. However, it is difficult to visualize clusters in higher dimensional spaces. The visualisation of a cluster can facilitate the physical interpretation. In addition, there is no reason to believe that complicated combinations of model parameters will yield meaningful clusters. As such, the clustering has been performed visually for combinations of 1 or 2 parameters.

There are 52 combinations of 2 parameters for the basic model parameterizations alone. Rather than cluttering this section with a large number of scatter plots only the three most meaningful clusterings will be discussed here. A subset of the remaining figures along with a small explanation of some interesting features is included in appendix C.3.

7.1 Clusters based on C_1^{crop} and C_3^{crop}

Figure 16a shows the scatter plot between C_1^{crop} and C_3^{crop} of the base model parameterization (p^{crop} and g linear with t_0^{parcel} variable and all other parameters fixed). Here we can identify six clusters, as labeled in figure 16b. Interestingly, cluster 3 seems to be separated by a diagonal line.

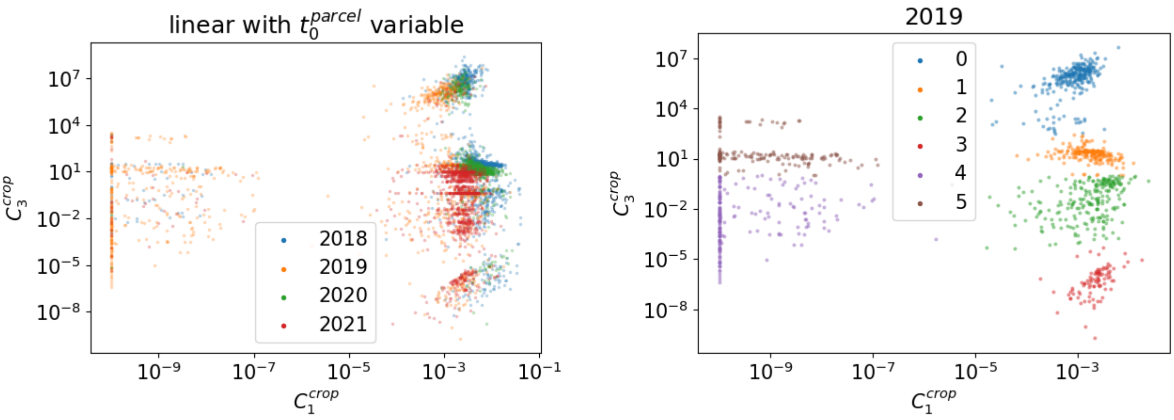

(a) (b)

Figure 16: (a) Scatter plot between C_1^{crop} and C_3^{crop} for the base model parameterization, i.e. p^{crop} and g linear with t_0^{parcel} variable and all other parameters fixed. For the image, values $C_1^{crop} < 10^{-10}$ were set to 10^{-10}. In the scatter plot, one can clearly identify six clusters. These are marked in (b) for 2019, where the labels in the legend will be used as identifiers for these clusters.

Table 4 shows the number of parcels in each cluster for each year, along with the irrigation rate accoring to the validation data (see section 2.5). We can calculate the p-value of the irrigation rates by using a t-test with null hypothesis that the irrigation probability is equal for a given cluster and the remaining parcels. This p-value is larger than 0.05 for all but three clusters: 2018, cluster 2 has p-value 0.0364, 2020 clusters 0 and 1 have p-values $2.28 \cdot 10^{-4}$ and $4.58 \cdot 10^{-3}$ respectively. For brevity, the rest of this section will focus on the significant clusters of 2018 and 2020, as these yield the most interesting results. A similar analysis for the 2019 and 2020 clusters is given in appendix C.1

Curiously, though the irrigation rate of especially cluster 0 in 2020 can be considered statistically significantly different from the average, this is not significantly reflected in the parcels of the same cluster in different years (though note that the average irrigation rate over all parcels is higher in 2020). To further investigate the difference between cluster 0 and cluster 1 of 2020, the average time series of both clusters are shown in figure 17.

There are two interesting differences between these time series, both of which are rather subtle. Firstly, and most importantly, the RVI of cluster 0 remains roughly constant between approximately 22 March and 25 April, whereas the RVI of cluster 1 is steadily decreasing in the same period. Probably as a result of this, the RVI of cluster 1 remains consistently lower until the beginning of July. Secondly, the RVI of cluster 1 has a larger dip in the first half of August. Both these phenomena coincide with a period of high rain deficit. This explains the high C_3^{crop} of cluster 0; the RVI of these parcels has a higher derivative than the ones of cluster 1. More importantly though, the lack of decrease in RVI during periods of high rain deficit could be caused by irrigation. This gives some support to the validity of the validation data. Yet, it remains questionable why this is only visible during the first and the last rain deficit peaks. This is especially so since we have some reason to believe that there is a catch crop on the parcels until the last week of April (see section 6.1). This will be discussed in more depth in section 8.4.1.

Table 4: The number of parcels and percentage of parcels that received irrigation according to the validation data (see section 2.5) in each of the clusters defined in figure 16b. Note that there is no irrigation data for 2021.

	2018		2019		2020		2021
Cluster	# parcels	% irrigated	# parcels	% irrigated	# parcels	% irrigated	# parcels
0	322	28.26	275	29.09	136	47.79	32
1	494	26.52	209	32.06	887	31.68	426
2	207	20.77	228	28.95	39	28.21	484
3	84	23.81	92	31.52	37	35.14	125
4	30	16.67	192	26.56	2	0.0	31
5	30	23.33	171	32.75	1	0.0	12
all	1167	25.45	1167	29.91	1102	33.58	1111

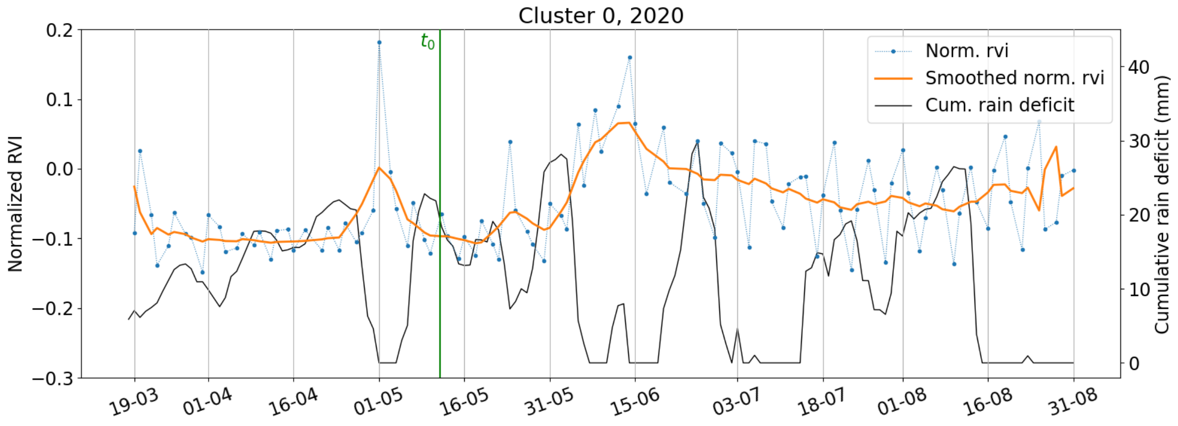

(a)

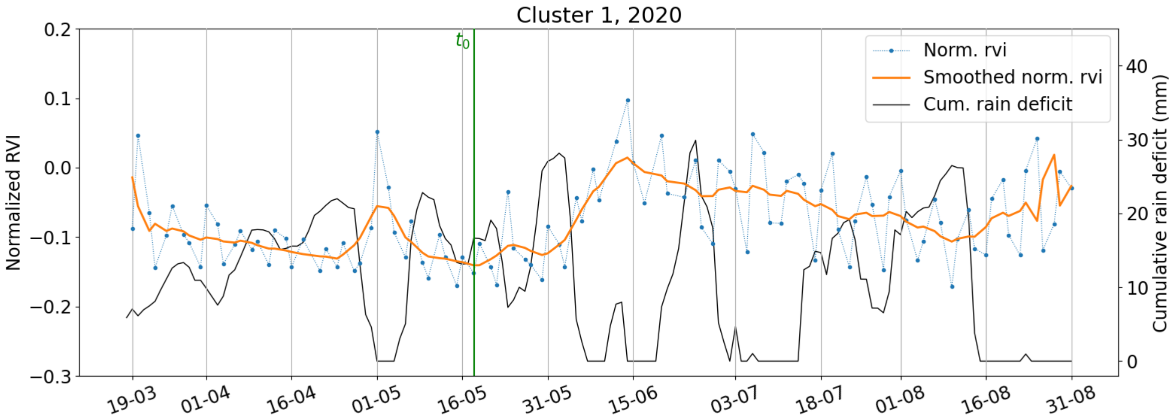

(b)

Figure 17: Average time series of parcels in the two large clusters in C_1^{crop} and C_3^{crop} of 2020, see table 4 and figure 19. The vertical green line marked t_0 represents the median of t_0^{parcel} in each cluster. The spread in t_0^{parcel} is quite large, so the accuracy of this indication is limited.

The average time series of cluster 0, 1 and 2 of 2018 are plotted in figure 18. Clusters 0 and 1 are actually pretty close to the time series that was kept in mind while designing the model. After the initial drop in RVI (which is not part of the model), the RVI increases for the entire growth season, as was originally expected. In addition, the RVI shows a rapid increase and subsequent decrease every time the rain deficit drops to (near) zero, a phenomenon that h^{crop} was designed for. Lastly, the growth rate decreases in cluster 1 during the long drought of the end of June to the beginning of August 2018. This effect is modelled by the growth inhibitor i_g^{crop} and is governed by the model parameter C_3^{crop}. This is also exactly the difference between cluster 0 and 1. Cluster 0 seem to grow uninhibitedly during the drought, which is best modelled by a very high C_3^{crop}.

Cluster 2 is even more extreme than cluster 1: its RVI decreases during the drought of July. This is best modelled by an even lower C_3^{crop}, so that the model expects no growth during times of high rain deficit. This matches with the (small) correlation between these clusters and irrigation that was found in table 4. Cluster 2 has less overlap with the irrigation validation data, and correspondingly it suffers the most from rain deficits. Once again, this gives some support to the validity of the validation data. However, the correlation is far too weak to build a classifier based on only this information.

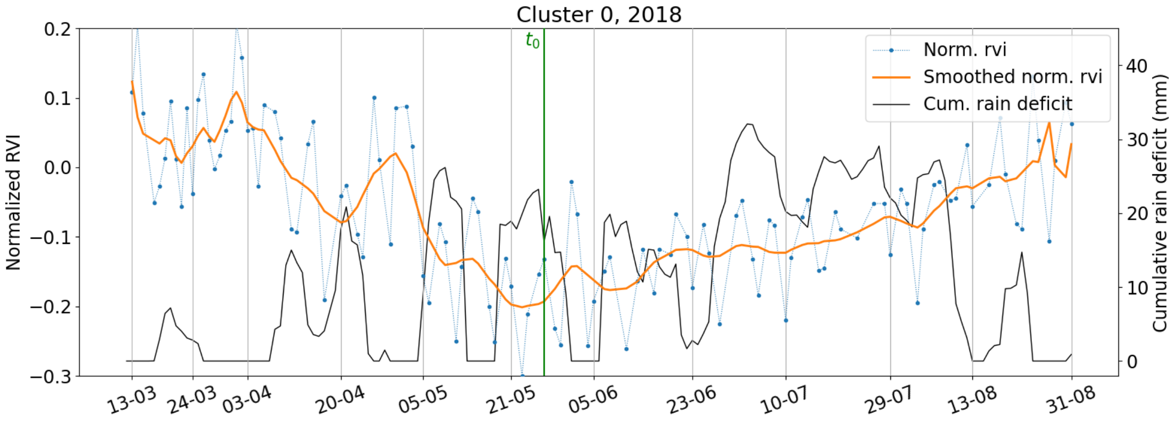

(a)

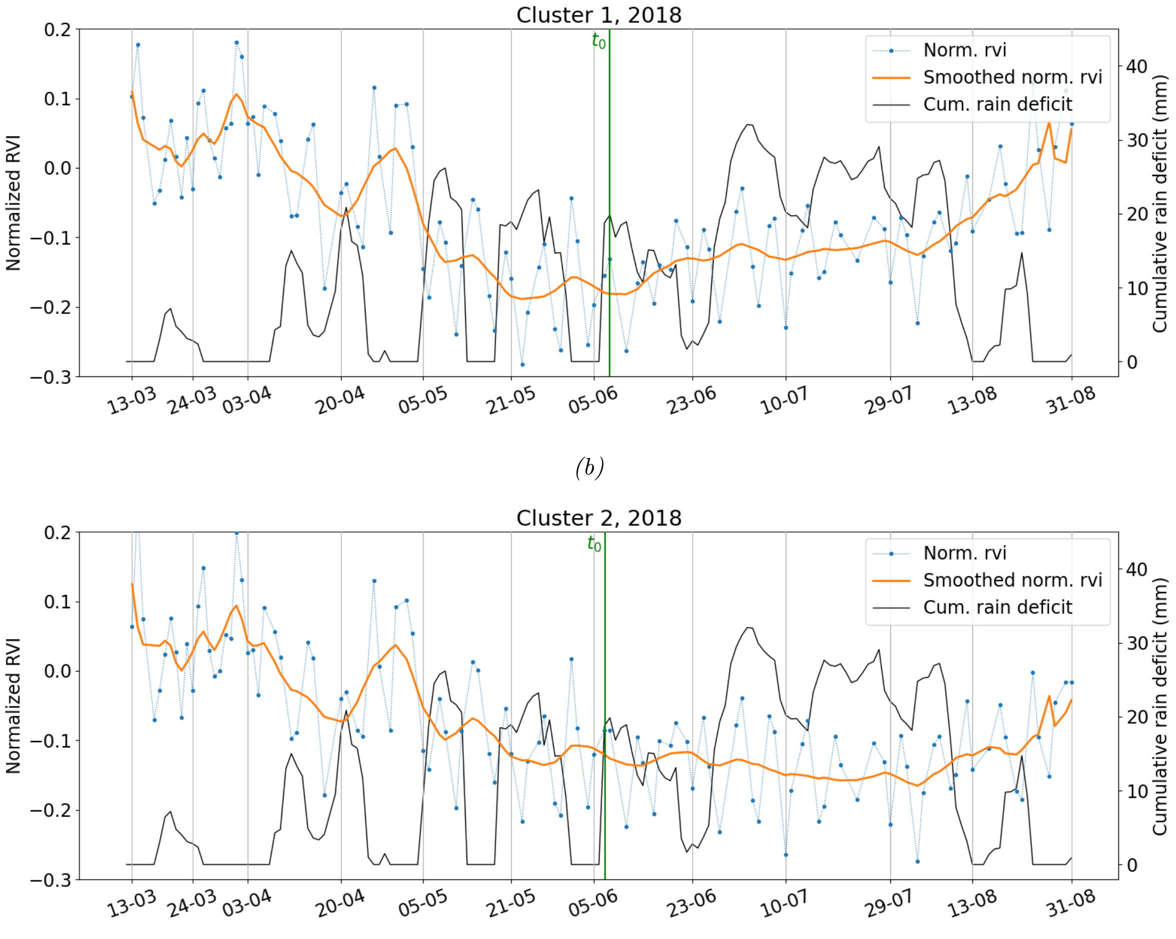

(b)

(c)

Figure 18: Average time series of parcels in the three large clusters in C_1^{crop} and C_3^{crop} of 2018, see table 4 and figure 19. The vertical green line marked t_0 represents the median of t_0^{parcel} in each cluster. The spread in t_0^{parcel} is quite large, so the accuracy of this indication is limited.

7.2 Clusters based on h_{min}^{crop}

In section 6.2, we found that $h_{min}^{crop} < 1$ compared to $h_{min}^{crop} = 1$ leads to an improved fit quality for only a minority of the parcels. To investigate why this is the case, the parcels are clustered according to their h_{min}^{crop} value and the quality of the fit compared to the base case $h = 1$. This is depicted in figure 19. The time series of the normalized RVI, averaged over the parcels in each cluster are plotted in figure 20.

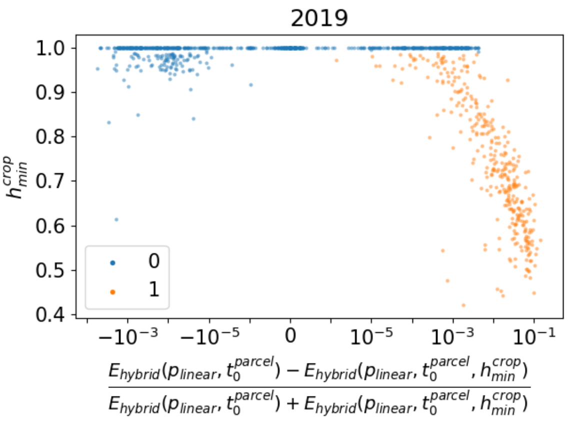

Figure 19: Definition of clusters in h_{min}^{crop}.

The RVI time series show one important difference between the two clusters. In cluster 0, the RVI decreases rapidly by approximately 0.3 in the first month after 19-03. On the other hand, the parcels in cluster 1 only decrease by about 0.1 in the same period. After the end of April, the RVI behaves nearly identically for both clusters.

This effect reveals an error in our approach for h^{crop}. Remember that the model scales the estimate of $v_i - v_0$ with the fraction $0 \leq h^{crop}_{min} \leq h^{crop}(rd(t)) \leq 1$, where $h^{crop} \downarrow h^{crop}_{min}$ as $rd(t) \to \infty$ (see equation (3.9)). The rationale behind this was that $v_i - v_0$ decreases as $rd(t)$ increases. However, for many parcels, $v_0 > v_i$ for most i. As a result, h^{crop} causes the modelled $v_i - v_0$ to increase rather than decrease, as the $v_i - v_0$ are negative. Because of this, $h^{crop}_{min} < 1$ causes the model to predict higher measurements during rain deficits, exactly the opposite of what happens in practice. This is the reason the calibration algorithm converges to $h^{crop}_{min} = 1$ for the majority of parcels.

The smaller set of parcels in cluster 1 have a positive normalized RVI during the period of low rain deficit (where RVI peaks). These can be accurately modelled by h^{crop}. Unfortunately, the magnitude of h^{crop}_{min} will be mostly determined by the average normalized RVI (i.e. how positive or negative the RVI is on average) instead of actual correlation with the rain deficit. Therefore, it is unlikely that this clustering will contain useful information on differences between parcels. In section 8.3.3 we will discuss how the application of h^{crop} in the model can be improved.

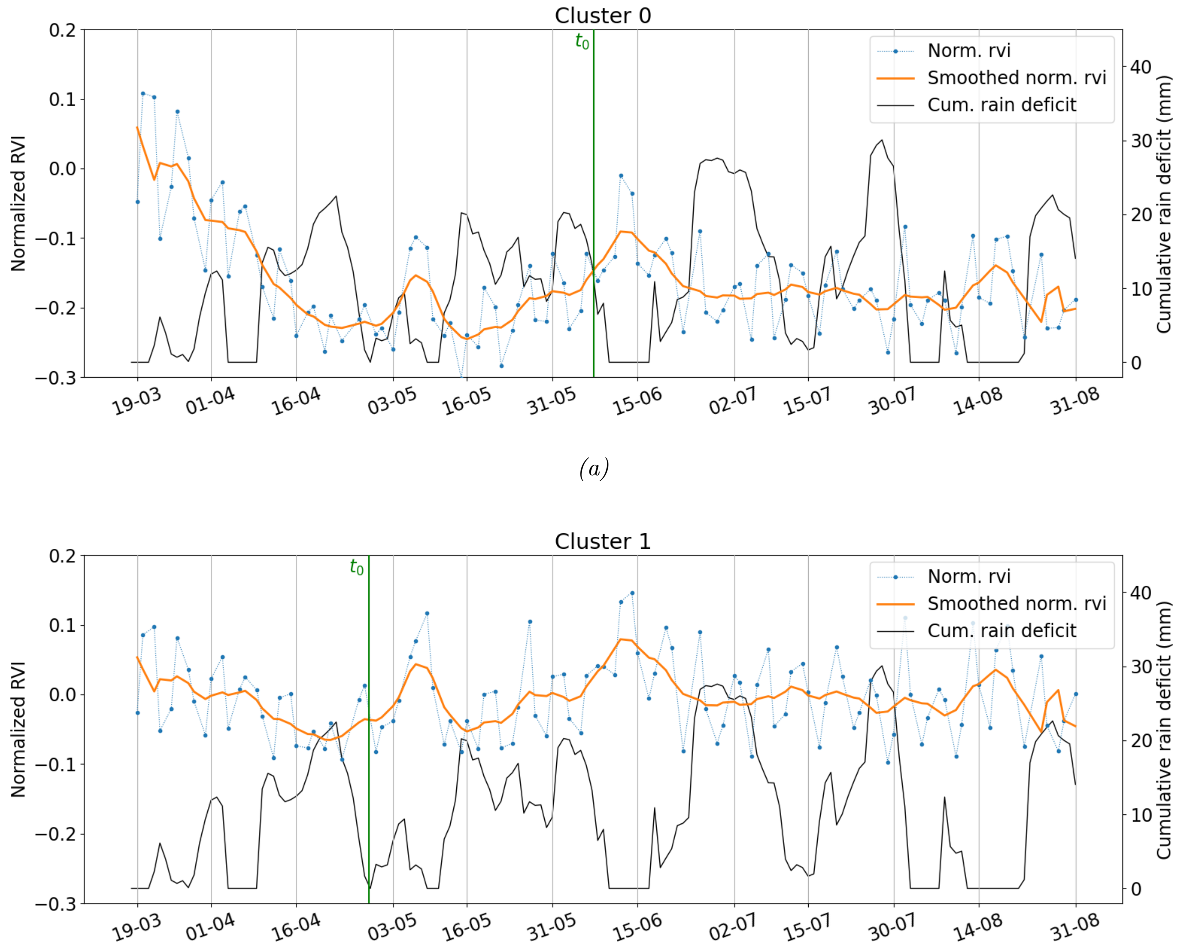

(a)

(b)

Figure 20: Average time series of 2019 of parcels in each of the clusters of h^{crop}_{min} as defined in figure 19. The vertical green line marked t_0 represents the median of t_0^{parcel} in each cluster.

Table 5 gives the number of parcels in each cluster as well as the percentage of irrigated parcels (according to the validation data). A t-test with null hypothesis that the irrigation probability is equal for both clusters can be used to obtain a p-value for the clustering-irrigation correlation. Somewhat unexpectedly, there is a statistically significant correlation (p-value $2.08 \cdot 10^{-6}$) between this clustering and irrigation. A priori we might have expected $h_{min}^{crop} = 1$ (cluster 0) to correlate with irrigation, as a higher h_{min}^{crop} indicates rain deficit independence, which can be the result of irrigation. However, as just discovered, $h_{min}^{crop} = 1$ indicates a drop in RVI in the first set of measurements rather than an independence of rain deficits.

Instead, we can postulate that the difference in drop in RVI itself might be the result of a difference in irrigation. As can be seen in figure 20a, the negative derivative of the RVI has three peaks around the first three peaks of the rain deficit (a slight delay can be caused by the smoothing). These parts are the biggest difference with figure 20b, where these negative peaks in derivative are far less pronounced. This is peculiar, as we believe this first period of decrease in RVI to be caused by the destruction of a catch crop before the potatoes are planted (see section 6.1).

Table 5: The number of parcels and percentage of parcels that received irrigation according to the validation data (see section 2.5) in each of the clusters defined in figure 19.

	2019	
Cluster	# parcels	% irrigated
0	829	33.53
1	337	20.77
all	1167	29.91

7.3 Clusters based on $t_0^{parcel} + \Delta t_1^{crop}$ and C_2^{crop}

For the bilinear basic model parameterization (i.e. g linear, p^{crop} bilinear, t_0^{crop} variable and other model parameters constant), the most interesting clusters can be found in C_2^{crop} and $t_0^{parcel} + \Delta t_1^{crop}$.

Figure 21 shows scatter plots between t_0^{parcel} and Δt_1^{crop} for the years 2019 and 2020. There are some very clear diagonal lines, indicating that $t_1^{parcel} = t_0^{parcel} + \Delta t_1^{crop}$ tends to cluster around certain values. Evidently, rather than the start of the second growth phase t_1^{parcel} being determined by a crop-dependent but parcel-independent "duration of the first growth phase", the transition to the second growth phase is fitted to specific moments in time. Note that this does not necessarily mean that there is an actual growth phase transition at that moment; it can also be the result of synchronous environmental factors, such as rainfall.

The clusters for C_2^{crop} are simple. As shown in figure 22, C_2^{crop} can be separated in two qualitatively different clusters: $C_2^{crop} > 0$ and $C_2^{crop} < 0$. Apparently, there is a distinction between parcels that have a decreasing RVI in the latter part of the time series (i.e. the part that gets marked as the second growth phase), and parcels that experience growth instead.

In this section, only the years 2019 and 2020 are investigated. This has two reasons. Firstly, 2018 and 2021 are less homogeneous in t_1^{parcel} (see appendix C.2). Secondly, $C_2^{crop} < 0$ for the majority of parcels in 2019, whereas $C_2^{crop} > 0$ for the majority of parcels in 2020, as we will see in table 6. Therefore, it will be informative to investigate the difference between these years.

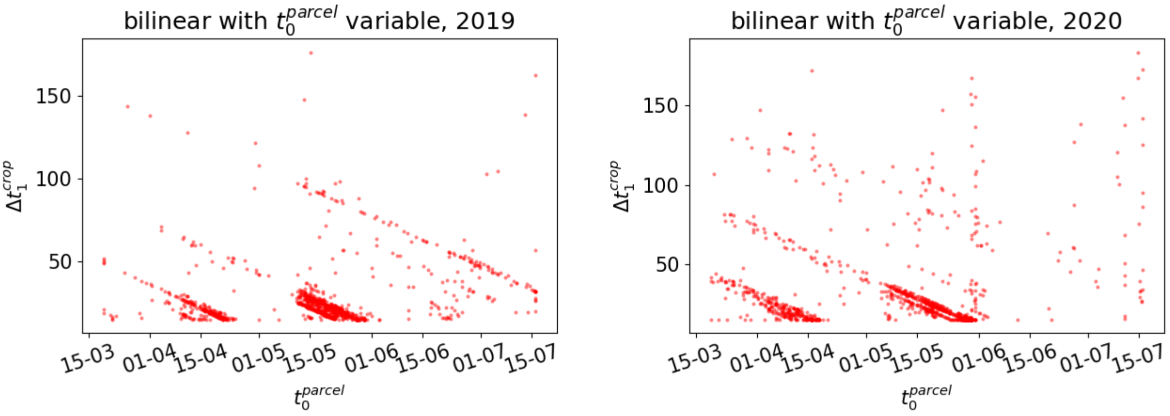

(a) *(b)*

Figure 21: Scatter plots between parameters t_0^{parcel} and Δt_1^{crop} for the years 2019 and 2020. The model parameterization used to generate these images is defined by bilinear p^{crop} with t_0^{parcel} variable and all other parameters fixed. The clear diagonal lines indicate that $t_0^{parcel} + \Delta t_1^{crop}$ tends to cluster.

Parcels can be divided into six clusters based on their t_1^{parcel} and C_2^{crop}. The definition of the clusters is depicted in figure 22. For each of these clusters, the number of parcels as well as the percentage of irrigated parcels (according to the validation data) are given in table 6. A t-test with null hypothesis that the irrigation probability is equal for both clusters can be used to obtain a p-value for the clustering-irrigation correlation. Only two clusters have a statistically significant variation (p-value smaller than 0.05) from the mean irrigation rate: cluster 0 (p-value $6.71 \cdot 10^{-4}$) cluster 3 (p-value $8.38 \cdot 10^{-3}$) of 2020 and cluster 5 (p-vaue $1.06 \cdot 10^{-2}$).

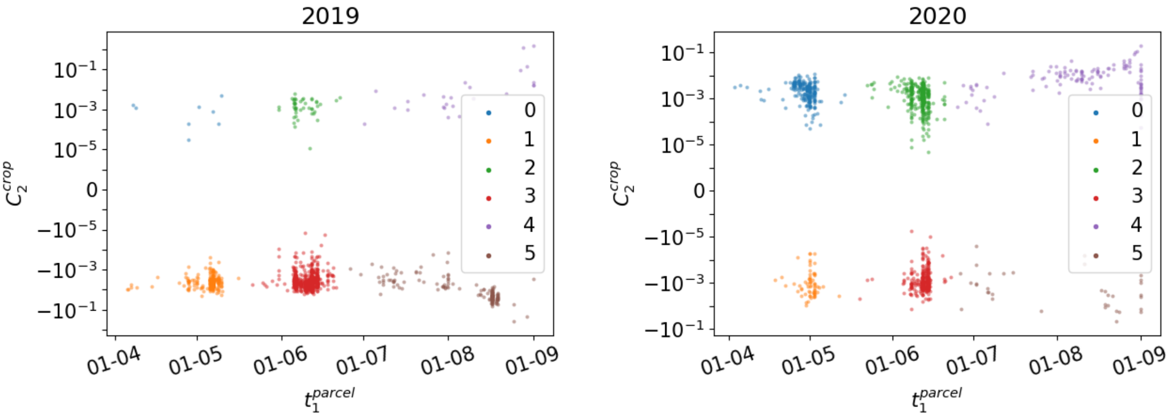

(a) *(b)*

Figure 22: Definition of clusters in the combination of C_2^{crop} and $t_1^{parcel} = t_0^{parcel} + \Delta t_1^{crop}$.

Table 6: The number of parcels and percentage of irrigated parcels (according to the validation data) in each of the clusters defined in figure 22.

	2019		2020	
Cluster	# parcels	% irrigated	# parcels	% irrigated
0	8	25.0	217	24.88
1	233	30.04	64	37.5
2	45	31.11	374	33.16
3	696	31.47	292	39.38
4	26	30.77	120	35.83
5	159	22.64	35	28.57
all	1167	29.91	1102	33.58

An explanation for why parcels can be divided into these six clusters can be found by looking at the average time series of each cluster. These average time series are shown in figures 23 to 26 for cluster 0 to 3 respectively, and cluster 5 from 2019 and cluster 4 from 2020 are shown in 27. Cluster 0, 2 and 4 for 2019 and cluster 5 for 2020 are very sparsely populated and will be left out of this investigation. In all these figures, the *medians* of t_0^{parcel} and $t_1^{parcel} = t_0^{parcel} + \Delta t_1^{crop}$ of are marked by a green and yellow vertical line.

Figure 23 shows the average time series of the parcels in cluster 0 for 2020. In this figure, the start of the second growth phase coincides with the bump in normalized RVI at the beginning of May. This makes sense, because the first phase then has strictly increasing RVI, which yields a good fit with our model. On the other hand, the peak at the first of June is slightly lower than the RVI at the end of year, which is the reason positive C_2^{crop}. This is also explains why there are almost no parcels in this cluster for 2019. August 2019 ended with a period of rain deficit, which cased RVI to decrease. As a result, the RVI at the end of August almost never exceeds the peak at the start of May.

Figure 24 shows the average time series of the parcels in cluster 1 for 2019 and 2020. Parcels in cluster 1 have a negative C_2^{crop} and a $t_1^{parcel} = t_0^{parcel} + \Delta t_1^{crop}$ that coincides with the RVI peak at the beginning of May, similar to cluster 0 of 2020. Unlike cluster 0, however, the bump around 15 June decreases as much as it increases in both 2019 and 2020. As a result, the latter part of the time series is approximately level with the dip in the middle of May. Because of this, the most optimal fit can be achieved by placing the phase transition at the peak of the first bump, and fitting a negative slope to the end of the year. The period of monotonous increase before the peak then allows a very accurate fit for the first part of the growth season.

Interestingly, in both years, cluster 1 has a significantly higher normalized RVI than the average (see figures 14b and 14c) for the majority of the time series. This can mainly be attributed to a significant increase in RVI between approximately 22 April and 3 May (2019) and 12 April and 24 April (2020) that is absent in cluster 0. This period of increase in RVI is peculiar, as it mostly coincides with a high rain deficit, especially for 2020.

One can feasibly hypothesize that this period of increase might be the result of irrigation. This could also (partly) explain the difference that causes the actual difference in model parameters: the behaviour of the bump in the middle of June. The crop is less hampered by the drought due to the irrigation, resulting in a more fully grown crop by the time rain in June falls. As a result, the crop does not experience a very significant growth in June, but only a temporary increase in water content. Once the drought returns, the RVI reverts to its old value as the crop water content decreases. On the other hand, unirrigated crops in cluster 0 make a growth spurt when enough water is available in June. The RVI then never drops down to the RVI from before the rain, as the crop growth is not reverted in the subsequent drought. Comparing this hypothesis with the validation data, we find that cluster 1 does indeed show a slightly above average irrigation rate, but it is not statistically significant. On the other hand, cluster 0 of 2020 does have a significantly lower irrigation rate, which lends a measure of support to this hypothesis.

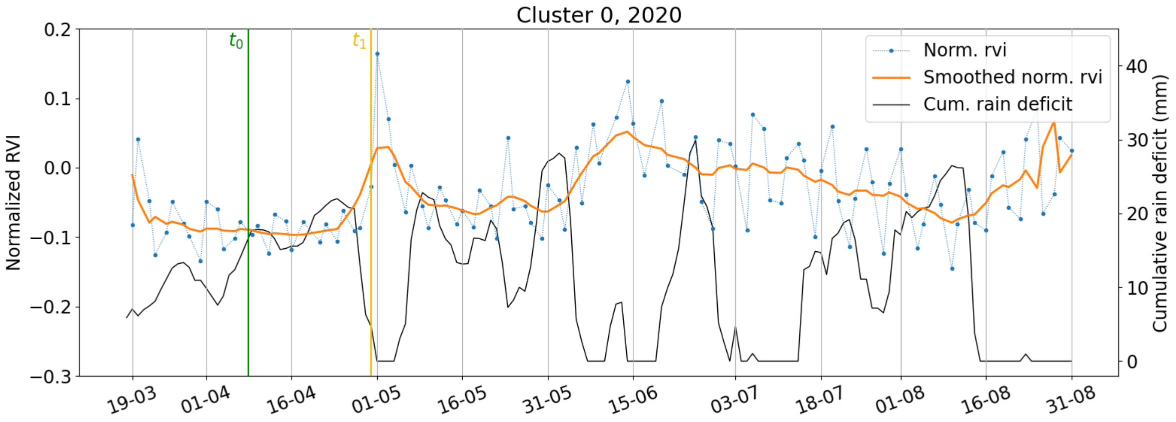

Figure 23: Average time series of parcels of cluster 0 as defined in figure 22. The vertical green line marked t_0 *and the vertical yellow line marked* t_1 *represent the medians of respectively* t_0^{parcel} $t_1^{parcel} = t_0^{parcel} + \Delta t_1^{crop}$ *in this cluster.*

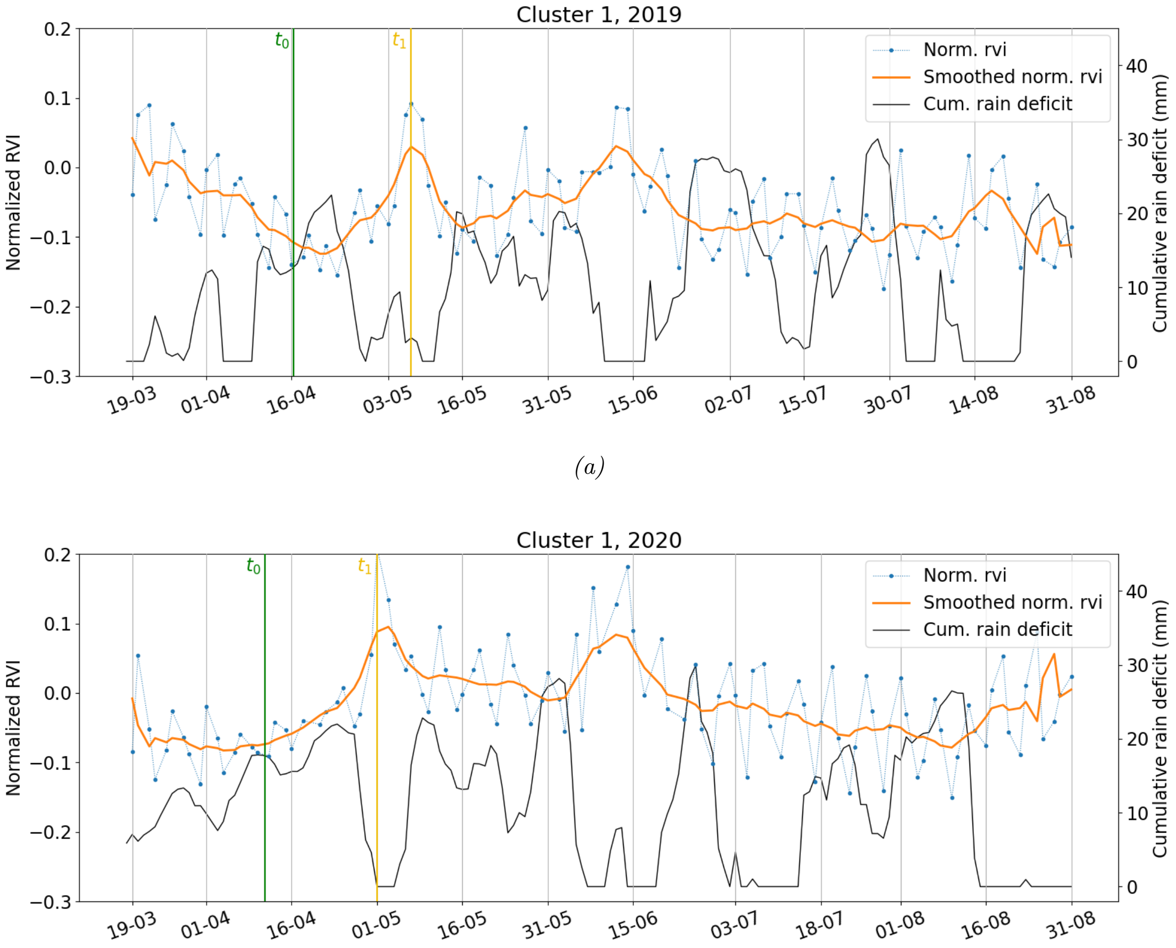

(a)

(b)

Figure 24: Average time series of parcels of cluster 1 as defined in figure 22. t_0^{parcel} *and* $t_1^{parcel} = t_0^{parcel} + \Delta t_1^{crop}$ *are the medians of the corresponding model parameters in this cluster.*

Figures 25 and 26 show the average time series of the parcels of respectively cluster 2 for 2020 and 3 for 2019 and 2020. The start of the second growth phase t_1^{crop} coincides with the RVI peak in June for each of the other three time series. The drop in RVI after the peak in the middle of June is considerably larger for cluster 3 parcels than cluster 2 parcels. As a result, parcels in cluster 3 are best modelled by negative C_2^{crop}, reflecting the drop in RVI after the peak around June 15. On the other hand, the RVI of cluster 2 climbs more in the latter half of August than it dropped between June 15 and August 15. As such, a positive C_2^{crop} is a better fit to these parcels

A possible explanation why the parcels in cluster 3 experience a more significant drop when the rain deficit once again accumulates at the end of June, is that the parcels in cluster 2 received irrigation after this point, whereas the parcels of cluster 3 did not. Once again, there is some agreement in the validation data. Cluster 3 has a greater irrigation level to a (barely) statistically significant level (p-value $4.89 \cdot 10^{-3}$). However, both clusters still have a significant number of both irrigated and non-irrigated parcels, so we cannot conclude that the difference between parcels is caused by irrigation alone.

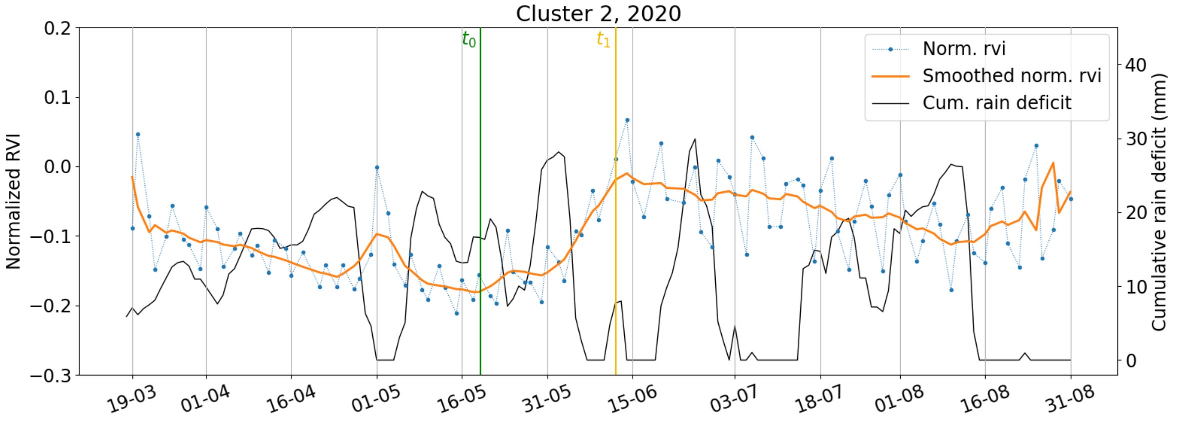

(a)

Figure 25: Average time series of parcels of cluster 2 as defined in figure 22. t_0^{parcel} and $t_1^{parcel} = t_0^{parcel} + \Delta t_1^{crop}$ are the medians of the corresponding model parameters in this cluster.

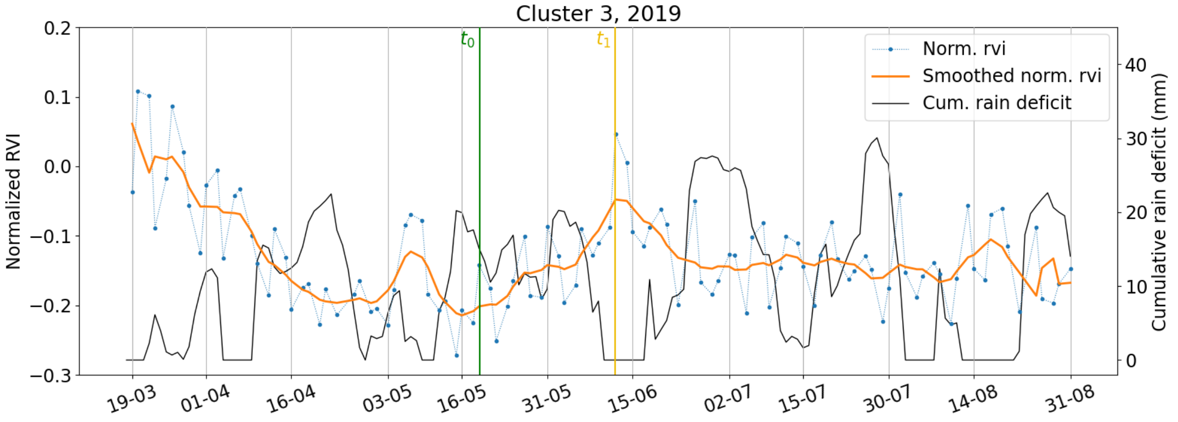

(a)

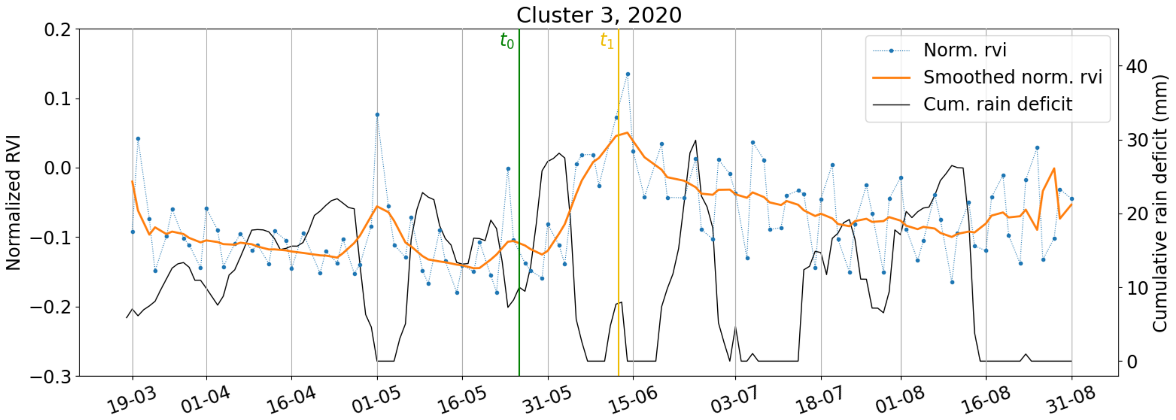

(b)

Figure 26: Average time series of parcels of cluster 3 as defined in figure 22. The vertical green line marked t_0 and the vertical yellow line marked t_1 represent the medians of respectively t_0^{parcel} $t_1^{parcel} = t_0^{parcel} + \Delta t_1^{crop}$ in this cluster.

Figure 27 shows the average time series of the parcels in cluster 5 for 2019 and cluster 4 for 2020. Both these are cluster for very high $t_1^{parcel} = t_0^{parcel} + \Delta t_1^{crop}$. However, cluster 5 has negative C_2^{crop} whereas cluster 4 has positive C_2^{crop}. Remember that cluster 4 in 2019 and cluster 5 in 2020 are both almost empty. An explanation can be found by comparing figure 27a and 26b. For both clusters, t_1^{parcel} is so high that only a small set of measurements fall into the second phase. For 2019, the *rain deficit* peaks at the end of August, whereas for 2020 it remains flat at zero in the corresponding period. As a result, the *RVI* decreases in the last few measurements of 2019, while it increases in late August 2020. This difference in the rain deficit of this period causes the difference in the sizes of clusters 1 and 4 of these years.

It is difficult to find out why the parcels in these clusters converge to such a high t_1^{parcel}. One reason might be the relatively low bump at the beginning of May (compared to the other clusters), especially for 2019. Yet, the difference with clusters 0 and 1 does not seem significant enough to fully explain this. Hence, it is not unlikely that the calibration algorithm converged to a local minimum for cluster 4 and 5 while the global minimum was actually near cluster 0 or elsewhere. Alternatively, cluster 0 could be the result of convergence to a local minimum, with the real optimum being near cluster 2 or 5.

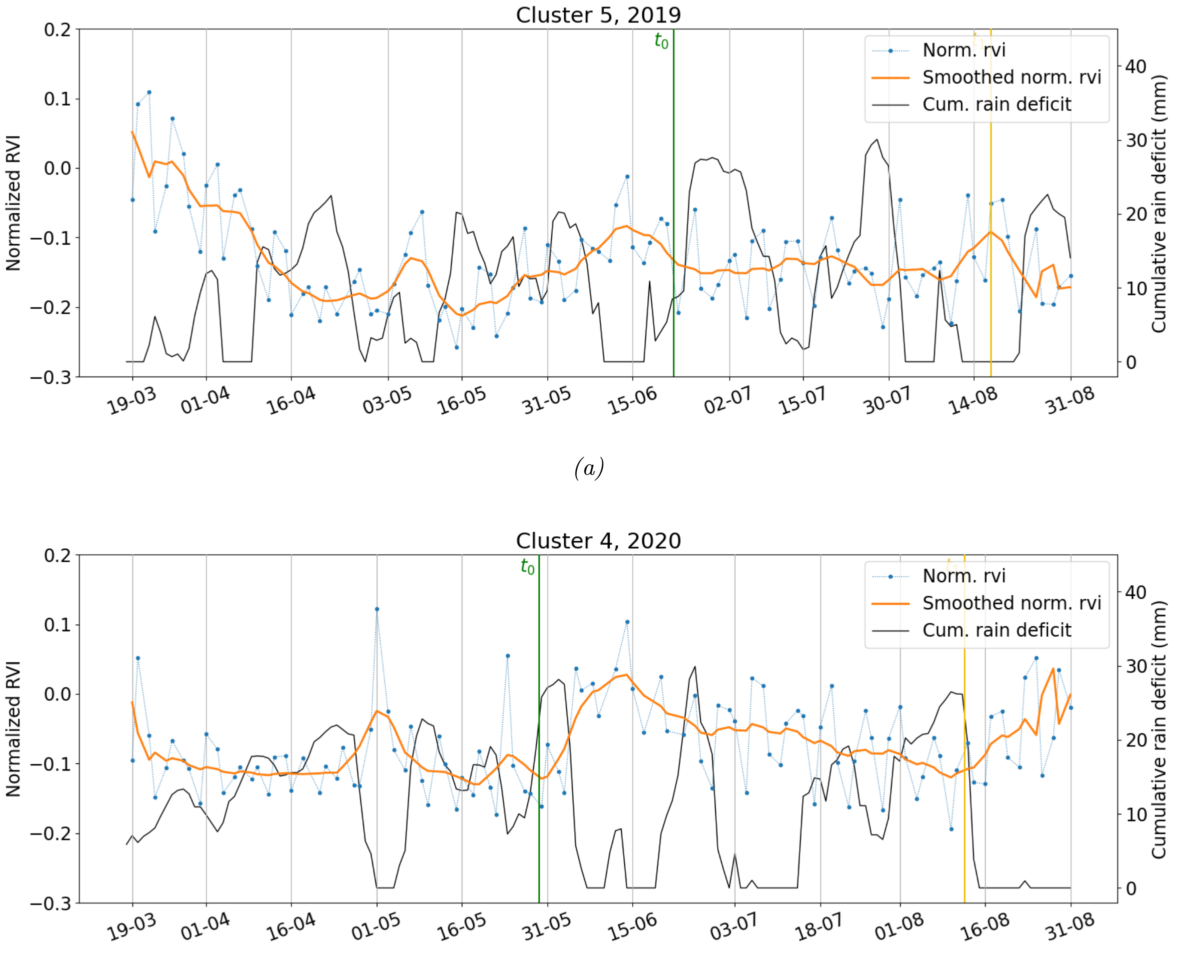

(a)

(b)

Figure 27: Average time series of parcels of cluster 5 for 2019 and cluster 4 for 2020, as defined in figure 22. The vertical green line marked t_0 *and the vertical yellow line marked* t_1 *represent the medians of respectively* t_0^{parcel} $t_1^{parcel} = t_0^{parcel} + \Delta t_1^{crop}$ *in this cluster.*

We have found that four out of six clusters in $t_1^{parcel} = t_0^{parcel} + \Delta t_1^{crop}$ are caused by the two peaks in May and June. This is to be expected, because they represent the most significant change in the derivative of RVI. This means that rather than actually modelling a 2-phase growth season, the bilinear fit is calibrated to the rain-deficit induced fluctuations in RVI. This can actually still be useful, as these fluctuations are likely to correlate with environmental factors such as irrigation. More will be discussed on this in section 8.1.2.

Looking at the average time series of 2018 and 2021 in figure 14a and 14d, it becomes clear why the clusters in t_1^{parcel} are less well-defined for 2018 and 2021. Where the time series of 2019 and 2020 have two clear bumps around the middle of the time series, 2021 has multiple smaller bumps (and one clear valley), and 2018 has no significant bumps after the beginning of May. Hence, optimal t_1^{parcel} is more diverse and more susceptible to noise than in 2019 and 2020.

8 Discussion

In this section, we will discuss some of our findings in more depth. This section consists of four parts.

In section 8.1, we will discuss possible causes of some of the important features of the behaviour of the RVI. Due to our lack of validation data, we have know way to validate the hypotheses we propose here. Therefore, we make some suggestions how future research can investigate these phenomena and further the understanding of the behaviour of the RVI.

In section 8.2, we discuss why the calibration algorithms give such poor performance for the two-phase models (bilinear and exponential) and especially the quadratic model. In addition, we make some suggestions on how to refine the implementation to reduce computation time and improve the consistency of the results.

In section 8.3 we discuss some of the limitations of the current model and its implementation. We then make some suggestions which model features are the most useful and how to further improve the related parameterization.

Finally, in section 8.4, we discuss the most important feature of the clusterings: its correlation with the precipitation deficit. We discuss possible explanations for the statistically significant correlation that was obtained earlier, and show some of the problems with these hypotheses. Lastly, we give an outline on how an irrigation classifier can be utilized to improve the watervraagprognosetool.

8.1 Behaviour of RVI during the growth season

In this section, we will discuss three of the most important, unexpected features of the behaviour of the RVI: the high correlation with rain deficit (section 8.1.1), the lack of long-term growth of the RVI (section 8.1.2), and the lack of obvious correlation with the irrigation data (section 8.4.1). For each, we will discuss possible causes and make some suggestions how these causes can be investigated in future research.

The main conclusion of this section is that in order to detect the subtle differences in RVI caused by irrigation, the model and methodology need to be tuned to very specifically look for these differences. In order to do that, a better understanding of how environmental factors influence the RVI is needed. To achieve this, future research is best served by collecting some more detailed data on what is happening in the fields, either through field experiments or through closer collaboration with the farmers.

8.1.1 Correlation with rain deficit

One of the most promising findings of this thesis is the correlation between RVI (radar vegetation index) and rain deficit. In the formulation of the model, we postulated that vegetation water content might have a strong correlation with rain deficit. As SAR backscatter is responsive to water in the plant, the backscatter and RVI should similarly correlate with the rain deficit. Scaling factor $h^{crop}(rd(t))$ was designed to model this effect. Unfortunately, this did not yet work as intended due to a flaky definition of v_0.

As made visible in the smoothed RVI time series (see figure 14), almost all of the large changes in RVI correlate precisely with, and are therefore probably caused by, changes in the rain deficit. This is such a dominant confirmation of our hypothesis that the influence of rain deficit on plant water content should be visible in a remote SAR image, that it calls for a critical analysis of the cause of these fluctuations. This is even more so because crop growth seems to have barely any influence on the RVI. There are two alternative explanations for the correlation between rain deficit and RVI.

Firstly, the clouds that are inevitably more present during a rainy season might influence the measurements. Note that one or two positive outliers (possibly caused by clouds) will be visualised as a smooth bump due to the smoothing applied on the time series. Even though atmospheric effects are filtered during the image preprocessing, this is not perfect, especially when the clouds cover the majority of the image. However, the bumps in the RVI cover much longer time periods than what could feasibly be caused by clouds. For instance, the June bump of 2019 and 2020 consists of about 12 subsequent, visibly increased measurements. The influence of clouds can be further investigated by comparing the RVI over areas without vegetation in with images of high rain deficit.

Secondly, the soil moisture can affect the RVI. As was explained in section 2.1.1, backscatter measurements are a combination of scatter from the vegetation and scatter from the soil. As such, changes in soil composition are likely to have an influence on the measurements. Especially for a crop like potatoes that does not have a very abundant biomass above the ground, the contribution of soil will be relatively more pronounced. If the soil moisture is the main driving force of changes in RVI, one would expect the fluctuations to decrease in magnitude during the growth season, as the crop canopy becomes more abundant. Indeed, this effect is somewhat visible in the time series of figure 14. However, the deflation of the magnitude of RVI fluctuations is much more significant in the time series of corn parcels, as can be seen in figure 33 of appendix B.2. As corn has a much more abundant canopy than potatoes, a larger part of the soil signal is blocked by the vegetation. As a result, the fluctuations in RVI show a much greater decrease in magnitude for corn parcels than for potato parcels.

The ratio between the contribution of soil moisture and vegetation water content can be estimated in a small-scale field test where water is injected rapidly in a dry field. In principle, the contribution to the change in RVI of plant water content should be delayed compared to that of soil moisture. Therefore, the effect on the RVI of both components can be estimated by measuring the evolution of the radio backscatter in the minutes following the injection. Since measurements need to be taken on the second to minute scale, a stationary radar will need to be used. Though the limited size of the antenna limits spatial resolution, this should not be a problem due to the proximity of the area of interest. Furthermore, to get a decent separation between the contribution of vegetation water content and soil moisture, the water should probably be injected considerably faster than regular irrigation systems do. To further increase precision, this can be combined with measurements of the plant water content with a second to minutes interval.

This experiment can help improve the understanding of the underlying mechanisms influencing the RVI. This is useful, because soil moisture is just as much an indicator of irrigation as high vegetation water content. Thus, regardless of the mechanism, irrigated parcels can be expected to have smaller rain deficit-dependent oscillations than unirrigated parcels. In addition, the RVI fluctuations as a result of rain deficits are modelled by h^{crop}, which also acts as a filter for these fluctuations. The remaining model parameters can then be used to model vegetation behaviour such as growth.

8.1.2 Lack of growth of the RVI

One of the most important assumptions in the development of the model was that RVI would increase during the growth season. However, this was not at all clear in the data. One might hypothesize that crop growth becomes significant only in August or later. The time series of 2018 and 2020 give some support for this as they show some significant increase in the month of August (see figures 14a and 14c). However, this also coincides with the a decrease in rain deficit, so it might be a temporary increase similar to the earlier bumps in RVI. In addition, above-ground biomass of potato plants typically peak in July or August [51].

Another possibility is that the growth is simply dwarfed by the rain-dependent fluctuations in RVI. This hypothesis is problematic because the RVI is literally designed to have a good correlation with vegetation abundance, and to decorrelate as much as possible with environmental factors such as soil moisture. Furthermore, there is an additional problem: how come the RVI drops so significantly during the first month after 19 March? As we mentioned in section 6.1, we believe this drop in RVI is likely caused by the presence of a catch crop that is destroyed before the potatoes are planted. The destruction usually happens chemically or mechanically [52]. In both cases, it takes time for the biomass to break down into the soil, so it makes sense for the drop in RVI to be spread over a month-long time period.

What is intriguing is the magnitude of the drop. Especially in 2018 and 2019, the RVI falls much further than either the rain deficit-dependent fluctuations, or the increase in the growth period of the main crop. This would seem to imply that the presence of a catch crop has greater influence on the RVI than potato plants do. From this, it seems to be possible for plant biomass to impact the RVI more than rain deficit can. This suggests an interesting direction for future research: studying the growth in RVI during the growth phase of the catch crop. This can help to improve understanding of RVI development during the growth phase of a crop, which in turn can provide insight into why the growth of potato and corn plants are barely visible in the RVI time series.

In this thesis, data analysis was performed on images from March up to and including August. We decided to use no images after August to reduce the necessity of fitting Δt_2^{crop}, and because rain deficits are most significant in the summer months. However, the downside of this is that the information on the remaining part of the year could have provided some additional insight in the development of RVI. Thus, a useful next step for future research would be to process the remaining images of one or more years. This can contribute to the understanding of the RVI development.

Development and validation of irrigation detection methodology would become significantly easier with a better understanding of the relation between vegetation abundance and RVI. In this section, we made some suggestions that are easy to implement as they only require readily available data. However, these will merely help to identify some correlation between the data and environmental factors. Ideally, to identify proper causation in these systems, future research should perform field experiments similar to the experiments suggested in the previous section.

8.1.3 Correlation with irrigation data

A priori, we expected to see several differences in the behaviour of the RVI of irrigated and non-irrigated parcels: lower correlation with rain deficits (i.e. lower magnitude of rain deficit-dependent bumps in RVI) and a greater growth that is less abated by rain deficits. However, the smoothed time series averaged over irrigated parcels (according to the validation data) show almost no difference with those averaged over non-irrigated parcels, see appendix B.1.

In none of the years, the bumps in the RVI are significantly abated for the irrigated parcels. Only the 2018 time series shows some behaviour that is in line with our expectations: the growth in the dry period of July is larger for the irrigated parcels than for their counterparts. In section 7.1, we saw this behaviour reflected in the lower irrigation rate of cluster 2 in 2018 in table 4. This gives some hope that rain deficit-dependent growth is visible in RVI time series, and can be detected by our methodology. However, no such things seem visible in 2019 and 2020. In addition, the correlation between irrigation and cluster 2, though statistically significant, is far too weak to build a proper classifier.

This is the main reason we doubt the validity, or at least the utility, of the validation data. Though there clearly seems to be some correlation with RVI, it is not consistent enough. Remember that the validation data marks parcels that have been irrigated at least once during the year. This provides a possible explanation why they do not yield a consistent difference in the RVI time series: some parcels could have been irrigated less frequently and/or in different periods of the year than others.

On the other hand, the validation data is not ambiguous on the non-irrigated parcels. These parcels have supposedly not been irrigated once in the entire year. Hence, none of these parcels should show behaviour similar to a parcel that received regular irrigation. Hence, it should be possible to identify clear clusters with a very high rate of irrigation. There are no such clusters in the results of this project. Of course, the methodology still has quite a lot of room for improvement, as we will discuss in sections 8.2 and 8.3. Therefore, these clusters might still appear when the methodology is optimized further.

So far, this project has mostly assumed that irrigation behaves very similarly to rain. Parcels that receive irrigation in periods of drought are expected to behave as if the rain deficit remained at a low level. Yet, it is very possible that that is actually not quite the case. For example, water injection by irrigation might be more gradual than rainfall, resulting in lower (but perhaps more consistent) soil moisture. As we also postulated that soil moisture is the main driving force behind the rain deficit-coupled oscillations in RVI, this could explain why the magnitude of these oscillations is no smaller for irrigated parcels compared to non-irrigated parcels

To investigate exactly how irrigation influences SAR measurements, more precise irrigation data is needed. Ideally, future research would perform some proper field experiments where multiple parcels are given varying levels of irrigation. More realistically, precise dates of irrigation can be obtained for a set of parcels through close collaboration with farmers. Coupling knowledge of irrigation dates and/or levels with RVI measurements, it might be possible to identify features of the RVI time series that are indicators of irrigation. The model parameterization can then be tuned to optimize sensitivity to these features, which will greatly improve correlations between clusters and irrigation.

8.2 Calibration

In sections 5.1 and 5.2 we found that the two-phase model parameterizations (i.e. the bilinear and exponential models) and the quadratic model give poor performance both in computation time and consistency of their results. In this section, we will discuss why this is the case and give some suggestions on how the implementation can be improved to improve performance. However, due to the lack of growth in RVI, the linear model will probably be more useful than the more advanced models discussed here. We will further elaborate on this in section 8.3.2.

8.2.1 Two-phase model parameterizations

The bilinear and, to a lesser extend, the exponential model parameterizations show a high variance in the results when the model is calibrated to the same data multiple times. This phenomenon is shown in figure 11e and 11f. Clearly, the hybrid method developed in this thesis is not capable of reliably converging to the global minimum. In addition, in section 5.3, we found that $C_1^{crop} \in \mathbf{C}_{both}$ gives hugely better performance than $C_1^{crop} \in \mathbf{C}_{nllsq}$. Normally, one would expect the non-linear least squares steps to be able to accurately fit C_1^{crop}, because the error statistic is smooth in C_1^{crop} with a single, global minimum. Yet, this is not the case here.

The reason for these phenomena and for why the two-phase models are such a difficult case for calibration is because t_0^{parcel} and Δt_1^{crop} are heavily coupled with most of the other parameters. That is to say, for the bilinear model, the value of t_0^{parcel} and Δt_1^{crop} has a large impact on the location of the optimum in C_1^{crop} and C_2^{crop}, and vice versa. This causes problems for the step-by-step calibration of the hybrid method, which can be understood as follows.

When $C_1^{crop} \in \mathbf{C}_{nllsq}$, t_0^{parcel} and Δt_1^{crop} are fitted in the differential evolution step using an estimate for the rest of the parameters generated by an initial non-linear least squares. This estimate is almost certainly not optimal, as made clear by the performance of non-linear least squares in figure 28f of appendix A.1. Given the sub-optimal estimate for $C_1^{crop} \in \mathbf{C}_{nllsq}$, the optimum for t_0^{parcel} and Δt_1^{crop} are unlikely to be at the global optimum of the system. As a result, even if differential evolution finds the "optimal" t_0^{parcel} and Δt_1^{crop} given the guesses for the other parameters, these will not necessarily be good estimates of their globally optimal values. Subsequently, the last non-linear least squares step can only settle for a sub-optimal C_1^{crop} and C_2^{crop}, as the estimates for t_0^{parcel} and Δt_1^{crop} are rather poor.

Therefore, it is not surprising $C_1^{crop} \in \mathbf{C}_{both}$ gives a better performance than $C_1^{crop} \in \mathbf{C}_{nllsq}$. This allows the differential evolution step to look for the joint optimum of t_0^{parcel}, Δt_1^{crop} and C_1^{crop} rather than looking for each separately. However, this is also a problem, as every additional parameter in differential evolution not only slows down the algorithm (see table 3), but also reduces the likelihood of it finding the global optimum. The latter is actually demonstrated by the difference in fit quality between $C_2^{crop} \in \mathbf{C}_{nllsq}$ and $C_2^{crop} \in \mathbf{C}_{both}$, see figure 12c. Even though the above argumentation why $C_1^{crop} \in \mathbf{C}_{both}$ outperforms $C_1^{crop} \in \mathbf{C}_{nllsq}$ also holds for C_2^{crop} (to a lesser extent, as it only depends on $t_0^{parcel} + \Delta t_1^{crop}$), the exact opposite is happening when $C_2^{crop} \in \mathbf{C}_{both}$ and $C_2^{crop} \in \mathbf{C}_{nllsq}$ are compared. As mentioned, in section 5.3, the cause of this is that the additional parameter in differential evolution makes it more difficult for the algorithm to find the optimum. This is also the reason the hybrid method considerably outperforms differential evolution for this case, see figure 28e of appendix A.1.

In addition to the two-phase models, the model including Δt_2^{crop} suffers a similar problem. Δt_2^{crop} is very similar to Δt_1^{crop} in terms of calibration, as the end of growth phase is basically a phase transition itself. Thus, C_1^{crop} has a similar dependence on Δt_2^{crop} as it does on Δt_1^{crop} in the bilinear model. However, the Δt_2^{crop} model has one less model parameter than the bilinear model. As a result, differential evolution by itself actually gives a decent performance. In fact, the parcels where differential evolution and the hybrid method give a large difference in quality $\left(\frac{|E_{hybrid}-E_{difev}|}{E_{hybrid}+E_{difev}} > 10^{-2}\right)$ are actually more commonly in favor of differential evolution than vice versa, as we saw in figure 10c. Clearly, differential evolution has a better chance of avoiding local minima, because it can simultaneously calibrate the interdependent C_1^{crop} and Δt_2^{crop}.

8.2.2 Quadratic model parameterization

In section 5.1, we saw that the quadratic model is a bad case for our calibration methods. Linear least squares gives a results of very poor quality (figure 28j). On the other hand, differential evolution and the hybrid method are terribly slow (see table 3); considerably slower than they are for the exponential method, which has 6 parameters instead of 4. Furthermore, the results of the hybrid method are considerably inconsistent (see figure 11g), and differential evolution is likely no better.

These problems are probably caused by the artificial bound on C_5^{crop} and C_6^{crop} that ensures the solution is real (see equation (3.35)). The RVI is often decreasing or approximately constant. As a result, in many cases, the optimal values for C_5^{crop} and C_6^{crop} lie precisely on this bound as this implies zero growth. Along the bound, the error statistic can still change. However, the gradient in the direction of the bound is usually much steeper than the gradient along the bound. As a result, each calibration algorithm will swiftly converge to the bound. After this point, convergence becomes more difficult, as there is only a narrow region along the bound that has negative gradient.

The bound on C_5^{crop} and C_6^{crop} defines a linear curve from the origin into the top left quadrant of (C_5^{crop}, C_6^{crop}) space (i.e. the quadrant $C_5^{crop} < 0$ and $C_6^{crop} > 0$). The bound requires C_5^{crop} and C_6^{crop} to remain above this boundary. The way the bound is enforced (equation (3.36)) introduces a large discontinuity in the derivative of the error statistic along the boundary. When the optimum is close to the boundary line, differential evolution will experience difficulty converging towards it, as it has to follow the curve through (C_5^{crop}, C_6^{crop}) space. Due to the recombination constant CR (see section 4.3.2), differential evolution is much better at following a gradient down one parameter, than at having to find the exact direction of a curve that is a combination of two.

To be more precise, a step $(\Delta C_5^{crop}, \Delta C_6^{crop})$ with either $\Delta C_5^{crop} = 0$ or $\Delta C_6^{crop} = 0$ (but not both) has probability of in the order of CR (exact value depending on the number of parameters and CR). This allows the algorithm to swiftly converge when there is a gradient in the direction of any of the parameters. Similarly, a step $(\Delta C_5^{crop}, \Delta C_6^{crop})$ with both $\Delta C_5^{crop} \neq 0$ and $\Delta C_6^{crop} \neq 0$ has probability in the order of (1 - CR). However, for $(\Delta C_5^{crop}, \Delta C_6^{crop})$ to be near parallel to some curve defined by the bound on C_5^{crop} and C_6^{crop}, $\mathbf{C1} + F(\mathbf{C2} - \mathbf{C3})$ (see algorithm 2) has to to be close to the direction of the line. It can take a large number of iterations before this occurs, which is the reason the calibration of the quadratic model takes much longer than other models of at least as many parameters (see table 3).

There are several possible ways to improve this. Firstly, one could attempt rotating the parameter space so that the bound falls in the direction of one of the parameters instead. However, this would mean $C_6^{crop} > 0$ would no longer be in the direction of one of the parameters, which is likely to give similar problems. Thus, it would be better to twist the parameter space by setting

$$C_5^{'crop} = C_6^{crop} + 4C_5^{crop}\frac{\max(0, v_{i-1} - v_0)}{h^{crop}(rd(t_{i-1}))}. \tag{8.1}$$

In the space of $(C_5^{'crop}, C_6^{crop})$, the bounds reduce to $C_5^{crop} > 0$ and $C_6^{crop} > 0$, which can be much more easily enforced by the algorithm.

Secondly, one can try to make the increase in error statistic in the artificial bound more gradual (equation (3.36)). By adding a small slope to the error statistic that goes from the direction of the bound, one can ensure the optimum is always in the real domain, while simultaneously allowing the algorithm to step into the domain of non-real solutions, which can considerably ease convergence.

Thirdly, the algorithm can be split into two steps. In the first step, the calibration is run with a relatively loose stopping criterion. If this converges to near the bound of C_5^{crop} and C_6^{crop}), the calibration is repeated, but it only looks for solutions *on* the bound, thus reducing the parameter space by one. This is a smooth error function, which should yield fast convergence with any of the calibration methods.

8.3 The vegetation index model

In this section, we will discuss how the parameterization and the implementation of the model can be improved to better reflect system behaviour. The most important conclusion is that the utilization of h^{crop} needs to be improved. This will allow better modelling of the rain deficit dependent oscillations in RVI. The implementation of h^{crop} can be improved in two ways. Most importantly, the estimation of v_0 needs to be improved to prevent negative values for the normalized RVI (section 8.3.1). Secondly, the parameterization of h^{crop} can be expanded to more accurately reflect system behaviour. The latter can be worthwhile because the rain deficit dependent fluctuations in RVI play such a dominant role in system behaviour.

8.3.1 Normalization of RVI

As shown in section 6.1, the assumption of that parcels are empty before the start of the growth season was incorrect for most parcels. In reality, most parcels show a large drop in RVI right before the potatoes are planted. As we explained in section 6.1, this drop is likely caused by the presence of a catch crop that is destroyed right before the main crop is planted. This skewed the results of this thesis as the model was not prepared to handle time series with mostly negative $v_i - v_0$. As a consequence, three aspects of the model did not function as intended.

Firstly, and most importantly, the modelling of rain deficit-induced temporary drops in RVI by h^{crop} did not be fitted to most of the data. This is especially problematic, because the rain deficit-coupled increases and decreases of RVI could be clearly recognized in the time series.

Secondly and thirdly, the exponential and quadratic model reduced to the equivalent of the linear model. Therefore, the results from these models could not be contribute to improving the understanding of system behaviour. "Fortunately", the time series gave no indication in the data that either model would be a good fit to the data.

Because of the importance of h^{crop}, one of the most important improvements to the model is to find an alternative definition of the normalized RVI that avoids negative values. There are several possible approaches for this.

One method is to find a better way to define v_0^{crop}. An important note here is that v_0^{crop} is one of the method used to properly combine the measurements from the four different orbits, so it would be a large advantage to preserve this property. v_0 can be defined on one of three different scales.

Firstly, one can take the minimum of the RVI time series as v_0. As this is quite sensitive to outliers, it is probably better to use some low percentile instead. This can then be further offset with a constant, as this effectively weighs down near-zero $v_i - v_0$ values in the fit of h^{crop}. A good offset is probably best determined empirically. Secondly, one can expand the previous method by using data from multiple years in the definition of v_0. It is reasonable to assume v_0 remains constant over a specific parcel for multiple years.

Thirdly, one can attempt to set a standard for v_0 that is applicable on all parcels. This is the most complicated approach, as it will require some research to validate spatial coherence of v_0 and to identify environmental factors that have a significant influence on v_0. For instance, v_0 is probably dependent on soil type, as that is the largest contributor to SAR backscatter in the absence (or even in the presence) of vegetation.

An alternative to estimating v_0 is the introduction of an orbit-dependent offset that equalizes the average v_i of each orbit. In addition to that, this offset can be used to decrease the RVI to a level that is optimal for h^{crop}, either with a fixed offset for all parcels, or a fixed average v_i after the offset. This is similar to the offset suggested as an extension to v_0 earlier, and it is probably best to determine the optimal offset empirically.

8.3.2 Modelling growth of RVI

One of the most important assumptions during the development of model, was that RVI increases during the growth season as a result of crop growth. However, as we discussed in section 8.1.2, this was not at all clear in the data. As a result, our models were largely overfitting the data. The bilinear model found optimal moments of phase transitions around bumps in the RVI that are much more likely to be caused by temporary mechanisms rather than long-term crop growth. These fits can actually be informative, as the size and duration of the bumps can be an indicator of environmental factors such as irrigation. However, this is obviously not what these models were designed for. To achieve that aim, it would be more effective to design model features around these phenomena, as we attempted to realize with h^{crop}_{min}. In fact, due to the very limited growth, using any growth model beyond linear (with some growth inhibitor $i^{crop}_g(rd)$) does not make sense.

Hence, our recommendations for this model is to use the linear model that was developed in this thesis. Develop new model features (or extent existing ones) to model phenomena that now seem to make two-phase parameterizations like the bilinear model useful. Suggestions for this will be given in the section 8.3.3. An additional benefit of the linear model is that the two-phase models are much more difficult to calibrate, as we discussed in section 8.2.1.

8.3.3 Scatter modifier h^{crop}

As h^{crop} is of such importance, we will give some suggestions on how it can be further extended in the future.

Firstly, an important area of optimization is the definition of the rain deficit $rd(t)$. In this thesis a cumulative rain deficit with a 6-day memory was used. Cumulative rain deficit is usually defined with a longer memory. The watervraagprognosetool (WVP) itself uses a 30-day memory, while the KNMI calculates it since the beginning of the growth season [53]. We chose for a relatively short memory, because a visual inspection of the data revealed that the RVI tended to correlate better with the derivative of the 30-day rain deficit than with the rain deficit itself. This choice, however, has received no further attention in this thesis. As such, there is likely some room for optimization. A visual inspection of the time series seems to imply that the RVI correlates better with an even shorter memory cumulative rain deficit.

In addition, rain deficit has been capped at zero, as we assumed that a negative rain deficit (i.e. a precipitation surplus) would have no significant impact on crop growth or vegetation water content. However, the RVI seems to be increasing for some time even after the rain deficit has become zero (see figure 14). This makes sense under the hypothesis that soil moisture has a large influence on RVI, as soil moisture can probably still increase significantly after the six day rain deficit has hit zero. Therefore, it is possible the accuracy of h^{crop} will improve when the definition of the rain deficit allows negative values.

Secondly, h^{crop}_{min} is currently defined using the same model parameters as the growth inhibitor i^{crop}_g. This helps reduce computational complexity of calibration. However, the fluctuations in RVI that correlate with rain deficit are much more dominant than any growth visible in the time series. As such, it is likely that h^{crop}_{min} and the RVI fluctuations will be dominant in the calibration of C^{crop}_3 and rd^{crop}_{max}. This can be a problem if the fluctuations in RVI are not of particular interest, for instance because they are possibly caused by soil moisture rather than vegetation water content (see section 8.1.1). In that scenario, h_{min}^{crop} can be used as a filter for these fluctuations. This way, the aspects of the model modelling growth will correlate better with the long-term trends instead of the short-term rain deficit interactions.

Thirdly, the utility of rd_{max}^{crop} can use some further research. In this project, we quickly sidelined this parameter when it did not yield a very significant improvements in figure 15c. However, it might give better results when the normalized RVI is defined such that it is mostly positive instead of negative. In addition, using a separate rd_{max}^{crop} for h_{min}^{crop} and for the growth modelling can further improve its performance. Furthermore, if the rain deficit is allowed negative values, rd_{max}^{crop} will almost certainly be needed to put a cap how large the influence of a precipitation surplus can be.

Lastly, h_{min}^{crop} is currently defined as a modification factor to the vegetation's impact on the RVI. However, if our earlier hypothesis is true that the fluctuations in RVI have more to do with soil moisture, they would be modelled more accurately with an additive term. In fact, it might be even more accurate to model it the other way around: an additive term that is dampened by vegetation size. After all, vegetation reduces the backscatter signal from the soil. This effect is visible in the RVI time series of mostly 2021 for potatoes (figure 14d) and those of all years corn parcels (figure 33 in appendix B.2). In these images, the magnitude of the rain deficit-correlated bumps reduces during the growth season. This is exactly the opposite of the original expectation that such fluctuations should be caused by crop water content, but it fits perfectly in the soil moisture hypothesis.

8.3.4 End of growth season Δt_2^{crop}

An interesting extension to the research would be to lengthen the time series with September and October. The additional data from the remainder of the growth season will improve the calibration of the model parameters, possibly revealing differences between parcels that were not visible before. However, this is also tricky to handle, as the harvest will almost certainly be included into the time series. This can skew the calibration if not handled properly, for instance by causing underestimation of the growth constant. Therefore, the end of the growth season Δt_2^{crop} will become more important. However, fitting Δt_2^{crop} is similarly somewhat risky, as the lack of growth in RVI might cause optimal $t_2^{parcel} = t_0^{crop} + \Delta t_2^{crop}$ estimate to be long before the harvest. This phenomenon was very clear when fitting Δt_2^{crop} to the 2019 data in figure 15d.

A possible solution to this problem is to set strict bounds on t_2^{parcel}. For most parcels, harvest will not happen before September [41]. Therefore, setting September 1 as a lower bound to t_2^{parcel} makes sense. However, this is a little difficult to enforce in our current calibration approach, as we fit Δt_2^{crop} instead of t_2^{parcel}. This makes it easy to set a minimum bound on the length of the growth season, but more difficult to set a bound to the t_2^{parcel} itself. If both bounds are needed, a diagonal bound in $(t_0^{parcel}, \Delta t_2^{crop})$ space will appear, which might cause similar problems to the ones we found for the quadratic model (see section 8.2.2).

8.4 Parcel clustering

In this section, we discuss possible causes for the correlation between the clustering and the irrigation validation data (section 8.4.1). Here, we conclude that more detailed irrigation data is necessary to validate that the correlation is actually caused by irrigation, rather than a mutual correlation with some environmental factor. Lastly, we will give an outline how a decently accurate irrigation classifier can be used to improve the irrigation prediction of the watervraagprognosetool in section 8.4.2.

8.4.1 Correlation with irrigation data

In each of the three clusterings that were discussed in section 7, there was some statistically significant correlation between the clusters and the irrigation validation data. Unfortunately, these differences in irrigation rate never exceed a factor two, meaning that any classifier based on these clusters will have very limited performance.

As we have seen, the clusters were mostly unrelated to any of the system features a certain model feature was designed for. Instead, either the rain deficit-driven oscillations in RVI or relatively short differences the derivative in RVI was what caused the distinctions. As a result, there was no directly obvious way to explain correlations between model parameters and irrigation data. Nevertheless, for each case, we managed to formulate a hypothesis on how irrigation might have caused the differences in time series between different clusters. However, these differences are much more subtle and short-lived than we had initially expected. Furthermore, if these differences are actually caused by irrigation, then one would expect a much larger difference in irrigation rate. Though this is an indication that our hypotheses linking irrigation to RVI behaviour is flawed, it can also be the validation data itself that is inaccurate.

In addition, for cluster 0 in (C_1^{crop}, C_3^{crop}) (figure 17a), the clustering based on h_{min}^{crop} (figure 20), and cluster 1 in $(t_1^{parcel}, C_2^{crop})$ (figure 24), the hypothesis was based on a difference in drop in RVI in the first month of the time series. However, we believe that decrease in RVI was caused by the destruction of a catch crop. This would imply that the parcels were irrigated while a catch crop was on it, or even after the process of destroying the catch crop had already started. This does not seem likely. A hypothetical explanation might be that the potato plants were planted while the catch crop biomass was still decomposing (i.e. the biomass was still visible to the SAR image). The subsequent decrease in RVI was caused by the further decomposition of the catch crop, but irrigation might have already taken place for the newly planted potatoes. This hypothesis could be tested in future research by collaborating more closely with the farmers, to obtain data on the exact dates of planting, irrigation and destruction of the catch crops.

In the case that these differences are not caused by irrigation, an alternative hypothesis for the correlation with irrigation rate is needed. One possibility is that the irrigation validation data correlates with other environmental factors such as soil type or behaviour of the farmer, which in turn might cause the differences between the RVI time series. It is not unlikely such correlation exists, because the irrigation data is spatially correlated as can be seen in figure 6. This would also explain the low rate correlation. For example, the areas indicated by the validation data might have a slightly higher percentage of a certain soil type, but the difference is unlikely to be an order of magnitude. In the specific example of soil type, this hypothesis can be tested by comparing clustering with a soil map. However, this investigation is outside of the scope of this thesis.

8.4.2 Employment in the watervraagprognosetool

This project is a step towards improving the predictive power of the irrigation model in the watervraagprognosetool developed by Witteveen+Bos. In many of the previous sections of the discussion, we gave reccomendations on how to improve the current methodology so that it can be used to classify irrigated and non-irrigated parcels. If a classifier is developed that achieves a decent performance, it can be used to improve the predictive power of the existing irrigation predictor in multiple ways.

Firstly, the information on the irrigation behaviour of recent years can be used to improve the irrigation model. Currently, the irrigation model is based on data from the period 1911-2011. More recent and more detailed data on irrigation can help to update and improve the model.

Secondly, continuous classifications of parcels during a growth season can be assimilated into a model to improve its predictive power. One can feasibly assume that irrigation of a parcel has a high degree of temporal coherence. If a field is irrigated at one point during a drought, it will likely continue to be irrigated as long as the drought persists (or until harvest). Hence, the information of which parcels received irrigation in recent weeks, should be usable to significantly improve to the prediction of future irrigation rates.

The performance of this second approach is largely dependent on the length of time series necessary to build an accurate classifier. This is a large advantage of the first approach. There, the irrigation estimates can be based on the time series of the entire growth season (or the entire year, if the remaining months prove to be useful). Furthermore, both methods can also be combined. Improving the model with time series from previous years is useful even when irrigation data of the current year is subsequently assimilated. In addition, the assimilation procedure itself can be optimized using the data from previous years. Therefore, the most logical first step is to build a classifier based on an entire growth season. This can be used with data from recent years to improve the model. Subsequently, research can investigate the possibility of further improving the model with irrigation data from the current year.

9 Conclusion

In this thesis, we investigated possibilities to detect irrigation of crop parcels by using remotely sensed SAR images. We showed that irrigation detection based on a single image is infeasible. Instead, we developed a methodology to classify parcels based on a time series of radar vegetation index (RVI) measurements. This is achieved by modelling the evolution of RVI measurements, and clustering the parcels based on calibration estimates of the model parameters. In this section, we summarize the main conclusions of this thesis, structured according to the research questions posed in the introduction.

Q1. How can the evolution of Sentinel-1 SAR measurements during the growth phase of a crop be modelled in the presence of rain deficits?

We successfully derived a model for the growth of RVI as a result of plant growth, taking into account the influence of rain deficit. Our implementation this model has one important flaw. The RVI measurements are normalized according to an estimated baseline RVI. The baseline RVI is consistently overestimated, resulting in mostly negative normalized RVI. This is problematic, because multiple model features were parameterized assuming positive normalized RVI. Most importantly, with the current parameterization, the model cannot properly describe precipitation deficit-driven fluctuations in the RVI when the normalized RVI is negative. These fluctuations are paramount to model system behaviour, so the first priority for future research should be to improve the estimation of the baseline RVI.

Furthermore, an investigation of average RVI time series revealed an obstacle within the measurements themselves. Here, we found that changes in the RVI are dominated by precipitation deficit dependent fluctuations rather than plant growth. In addition, the influence of irrigation on the RVI is very subtle. To develop an accurate classifier, it is important to uncover the features of the RVI time series that are indicators of irrigation. To this end, future research is best served by collecting exact irrigation dates of several parcels.

Q2. How can the model be efficiently and reliably calibrated to a large number of parcels?

The model has discontinuities in its derivatives with respect to multiple model parameters. Because of this, reliably calibrating the model is difficult. Therefore, we customly designed a calibration method for this problem that combines the standard methods non-linear least squares and differential evolution. In this method, dubbed the hybrid method, only the parameters that perform poorly in non-linear least squares are calibrated using the more computationally expensive differential evolution. The hybrid method yields fairly consistent and qualitatively good results in reasonable computation time, especially for some of the simpler model parameterizations.

Q3. How do the values of the calibrated model parameters correlate with irrigation?

We calibrated multiple different model parameterizations to RVI measurements of 1167 potato parcels in a validation region. Several clusterings of the model parameters showed statistically significant correlation with the irrigation validation data. The variation in irrigation rate never exceeded a factor two, so it is not yet possible to build an accurate classifier based on these clusters. Nevertheless, this correlation indicates that the methodology is sound. With more detailed irrigation data and an improved estimation of v_0, it might be possible to achieve a decent classification performance with this methodology.

References

[1] Nederlands Hydrologisch Instrumentarium, “Landelijk Hydrologisch Model,” 2019. [Online]. Available: https://www.nhi.nu/

[2] Witteveen+Bos and HKV lijn in Water, “Watervraagprognosetool documentation,” 2020.

[3] Ministerie van Economische Zaken (Rijk), “Basisregistratie Gewaspercelen (BRP).” [Online]. Available: https://data.overheid.nl/en/dataset/10674-basisregistratie-gewaspercelen--brp-

[4] Nationaal Hydrologisch Instrumentarium, “Modelrapportage - Deelrapport Beregening,” no. December, 2008. [Online]. Available: http://nhi.nu/documenten/DR10/NHI2008DR10_v2_Beregening.pdf

[5] M. W. Hoogeveen, K. H. M. Bommel, and G. Cotteleer, *Beregening in land- en tuinbouw : rapport voor de Droogtestudie Nederland*, 2003. [Online]. Available: http://library.wur.nl/wasp/bestanden/LUWPUBRD_00320859_A502_001.pdf

[6] Wageningen Economic Research, “BINternet, land- en tuinbouw,” 2022. [Online]. Available: https://www.agrimatie.nl/Binternet.aspx

[7] D. M. G. dela Torre, J. Gao, and C. Macinnis-Ng, “Remote sensing-based estimation of rice yields using various models: A critical review,” *Geo-Spatial Information Science*, vol. 00, no. 00, pp. 1–24, 2021. [Online]. Available: https://doi.org/10.1080/10095020.2021.1936656

[8] W. Jiao, L. Wang, and M. F. McCabe, “Multi-sensor remote sensing for drought characterization: current status, opportunities and a roadmap for the future,” *Remote Sensing of Environment*, vol. 256, no. January, p. 112313, 2021. [Online]. Available: https://doi.org/10.1016/j.rse.2021.112313

[9] H. Fang, F. Baret, S. Plummer, and G. Schaepman-Strub, “An Overview of Global Leaf Area Index (LAI): Methods, Products, Validation, and Applications,” *Reviews of Geophysics*, vol. 57, no. 3, pp. 739–799, 2019.

[10] M. A. El-Shirbeny and K. Abutaleb, “Sentinel-1 Radar Data Assessment to Estimate Crop Water Stress,” *World Journal of Engineering and Technology*, vol. 05, no. 02, pp. 47–55, 2017. [Online]. Available: http://www.scirp.org/journal/doi.aspx?DOI=10.4236/wjet.2017.52B006

[11] S. C. Steele-dunne, H. Mcnairn, A. Monsivais-huertero, and I. J. Judge, “Radar Remote Sensing of Agricultural Canopies : A Review,” *IEEE Journal of Selected Topics in Applied Earth Observations and Remote Sensing*, 2017.

[12] L. Karthikeyan, I. Chawla, and A. K. Mishra, “A review of remote sensing applications in agriculture for food security : Crop growth and yield , irrigation , and crop losses,” *Journal of Hydrology*, vol. 586, no. March, p. 124905, 2020. [Online]. Available: https://doi.org/10.1016/j.jhydrol.2020.124905

[13] D. Han, S. Liu, Y. Du, X. Xie, L. Fan, L. Lei, Z. Li, H. Yang, and G. Yang, “Crop Water Content of Winter Wheat Revealed with Sentinel-1 and Sentinel-2 Imagery,” *Sensors*, vol. 19, no. 18, p. 4013, sep 2019. [Online]. Available: https://www.mdpi.com/1424-8220/19/18/4013

[14] A. Veloso, S. Mermoz, A. Bouvet, T. Le Toan, M. Planells, J. F. Dejoux, and E. Ceschia, “Understanding the temporal behavior of crops using Sentinel-1 and Sentinel-2-like data for agricultural applications,” *Remote Sensing of Environment*, vol. 199, pp. 415–426, 2017.

[15] G. Wiseman, H. McNairn, S. Homayouni, and J. Shang, “RADARSAT-2 Polarimetric SAR Response to Crop Biomass for Agricultural Production Monitoring,” *IEEE Journal of Selected Topics in Applied Earth Observations and Remote Sensing*, vol. 7, no. 11, pp. 4461–4471, nov 2014. [Online]. Available: https://ieeexplore.ieee.org/document/6827173/

[16] Y. Kim, T. Jackson, R. Bindlish, H. Lee, and S. Hong, “Radar vegetation index for estimating the vegetation water content of rice and soybean,” *IEEE Geoscience and Remote Sensing Letters*, vol. 9, no. 4, pp. 564–568, 2012.

[17] Z. He, S. Li, Y. Wang, L. Dai, and S. Lin, "Monitoring rice phenology based on backscattering characteristics of multi-temporal RADARSAT-2 datasets," *Remote Sensing*, vol. 10, no. 2, 2018.

[18] F. Meyer, "Spaceborne Synthetic Aperture Radar: Principles, Data Access, and Basic Processing Techniques," in *The SAR Handbook: Comprehensive Methodologies for Forest Monitoring and Biomass Estimation*, 2019, ch. 2.

[19] T. van Emmerik, *Open Aircraft Performance Modeling Based on an Analysis of Aircraft Surveillance Data*, 2017.

[20] I. H. Shahrezaei and H. C. Kim, "Resolutional analysis of multiplicative high-frequency speckle noise based on SAR spatial de-speckling filter implementation and selection," *Remote Sensing*, vol. 11, no. 9, pp. 1–24, 2019.

[21] European Space Agency, "Sentinel 1 SAR user guide." [Online]. Available: https://sentinels.copernicus.eu/web/sentinel/user-guides/sentinel-1-sar/

[22] Airbus Defence and Space, "TerraSAR-X Image Product Guide," no. 2.1, pp. 1–24, 2015. [Online]. Available: https://www.intelligence-airbusds.com/files/pmedia/public/r459_9_20171004_tsxx-airbusds-ma-0009_tsx-productguide_i2.01.pdf

[23] European Space Agency, "SNAP - ESA Sentinel Application Platform - Help Documentation," 2021.

[24] F. Filipponi, "Sentinel-1 GRD Preprocessing Workflow," *Proceedings*, vol. 18, no. 1, p. 11, 2019.

[25] G. Kaplan, L. Fine, V. Lukyanov, V. S. Manivasagam, J. Tanny, and O. Rozenstein, "Normalizing the Local Incidence Angle in Sentinel-1 Imagery to Improve Leaf Area Index, Vegetation Height, and Crop Coefficient Estimations," *Land*, vol. 10, no. 7, p. 680, jun 2021. [Online]. Available: https://www.mdpi.com/2073-445X/10/7/680

[26] T. Weiß, T. Ramsauer, A. Löw, and P. Marzahn, "Evaluation of Different Radiative Transfer Models for Microwave Backscatter Estimation of Wheat Fields," *Remote Sensing*, 2020.

[27] T. Weiß, T. Ramsauer, T. Jagdhuber, and A. Löw, "Sentinel-1 Backscatter Analysis and Radiative Transfer Modeling of Dense Winter Wheat Time Series," *Remote Sensing*, pp. 1–25, 2021.

[28] G. Hajduch, "Masking "No-value" Pixels on GRD Products generated by the Sentinel-1 ESA IPF," *S-1 Mission Performance Centre*, 2018. [Online]. Available: https://sentinel.esa.int/web/sentinel/user-guides/sentinel-1-sar/document-library

[29] R. Piantanida, N. Miranda, and G. Hajduch, "MPC-S1: Thermal Denoising of Products Generated by the Sentinel-1 IPF," *Sentinel-1 Document Library*, 2017. [Online]. Available: https://sentinels.copernicus.eu/web/sentinel/user-guides/sentinel-1-sar/document-library/-/asset_publisher/1dO7RF5fJMbd/content/thermal-denoising-of-products-generated-by-the-sentinel-1-ipf

[30] T. Fritz, H. Breit, and M. Eineder, "TerraSAR-X Products – Tips and Tricks," 2008. [Online]. Available: https://slidex.tips/downloadFile/terrasar-x-products-tips-and-tricks

[31] D. Small and A. Schubert, "Guide to ASAR Geocoding," *RSL-ASAR-GC-AD*, no. 1.0.1, p. 36, 2008.

[32] J. W. Goodman, "Some fundamental properties of speckle*," *Journal of the Optical Society of America*, vol. 66, no. 11, p. 1145, 1976.

[33] J.-S. Lee and E. Pottier, *Polarimetric radar imaging : from basics to applications.* CRC Press, 2009.

[34] Esri Inc., "ArcGis Pro," Redlands, CA, 2021.

[35] Y. Kim and J. J. Van Zyl, "A time-series approach to estimate soil moisture using polarimetric radar data," *IEEE Transactions on Geoscience and Remote Sensing*, vol. 47, no. 8, pp. 2519–2527, 2009.

[36] D. Mandal, V. Kumar, D. Ratha, S. Dey, A. Bhattacharya, J. M. Lopez-Sanchez, H. McNairn, and Y. S. Rao, “Dual polarimetric radar vegetation index for crop growth monitoring using sentinel-1 SAR data,” *Remote Sensing of Environment*, vol. 247, no. June, p. 111954, 2020. [Online]. Available: https://doi.org/10.1016/j.rse.2020.111954

[37] C. Szigarski, T. Jagdhuber, M. Baur, C. Thiel, M. Parrens, J. P. Wigneron, M. Piles, and D. Entekhabi, “Analysis of the Radar Vegetation Index and potential improvements,” *Remote Sensing*, vol. 10, no. 11, pp. 0–15, 2018.

[38] S. Dinesh Kumar, S. Srinivasa Rao, and J. R. Sharma, “Radar Vegetation Index as an Alternative to NDVI for Monitoring of Soyabean and Cotton Developing hydrological model for estimating soil moisture View project Search for the course of Vedic river Sraswati View project Radar Vegetation Index as an Alternat,” *Indian Cartographer*, vol. XXXIII, no. Vmc, pp. 2009–2014, 2013. [Online]. Available: https://www.researchgate.net/publication/267020154

[39] M. Trudel, F. Charbonneau, and R. Leconte, “Using RADARSAT-2 polarimetric and ENVISAT-ASAR dual-polarization data for estimating soil moisture over agricultural fields,” *Canadian Journal of Remote Sensing*, vol. 38, no. 4, pp. 514–527, 2012.

[40] R. Nasirzadehdizaji, F. Balik Sanli, S. Abdikan, Z. Cakir, A. Sekertekin, and M. Ustuner, “Sensitivity Analysis of Multi-Temporal Sentinel-1 SAR Parameters to Crop Height and Canopy Coverage,” *Applied Sciences*, vol. 9, no. 4, p. 655, feb 2019. [Online]. Available: http://www.mdpi.com/2076-3417/9/4/655

[41] Nederlandse Aardappel Organisatie, “Wat is het aardappelseizoen?” [Online]. Available: https://kennisplatform.aardappels.nl/wat-is-het-aardappelseizoen

[42] B. your profit, “Wanneer kunnen we maïs zaaien?” 2020. [Online]. Available: https://www.boerenbusiness.nl/businesscase/limagrain/artikel/10886584/wanneer-kunnen-we-ma-s-zaaien

[43] J. G. Chang, M. Shoshany, and Y. Oh, “Polarimetric Radar Vegetation Index for Biomass Estimation in Desert Fringe Ecosystems,” *IEEE Transactions on Geoscience and Remote Sensing*, vol. 56, no. 12, pp. 7102–7108, 2018.

[44] J. Goudriaan, “Using the expolinear growth equation to analyse resource capture,” *Resource capture by crops*, pp. 99–110, 1994.

[45] P. Steduto, T. C. Hsiao, D. Raes, and E. Fereres, “AquaCrop—The FAO Crop Model to Simulate Yield Response to Water: I. Concepts and Underlying Principles,” *Agronomy Journal*, vol. 101, no. 3, pp. 426–437, may 2009. [Online]. Available: https://onlinelibrary.wiley.com/doi/10.2134/agronj2008.0139s

[46] J. Sagardoy, A. Bottrall, and G. Uittenbogaard, “Organization, operation and maintenance of irrigation schemes,” *FAO irrigation and drainage paper*, no. 40, pp. Annex II, chapter 2, 1986. [Online]. Available: https://www.fao.org/3/x5647e/x5647e0e.htm#2.rotationalsupplywithlimitedwater

[47] R. Storn and K. Price, “Differential Evolution - A Simple and Efficient Heuristic for Global Optimization over Continuous Spaces,” *Journal of Global Optimization*, vol. 11, no. 4, pp. 341–359, 1997.

[48] A. Qin and P. Suganthan, “Self-adaptive Differential Evolution Algorithm for Numerical Optimization,” in *2005 IEEE Congress on Evolutionary Computation*, vol. 2. IEEE, jul 2014, pp. 1785–1791. [Online]. Available: https://www.scientific.net/AMR.989-994.2536http://ieeexplore.ieee.org/document/1554904/

[49] D. Dawar and S. Ludwig, “Differential evolution with dither and annealed scale factor,” in *2014 IEEE Symposium on Differential Evolution (SDE)*, no. December 2014. IEEE, dec 2014, pp. 1–8. [Online]. Available: http://ieeexplore.ieee.org/document/7031528/

[50] G. Roerink, “Bouwland areaal heeft 45% winterbedekking,” 2022. [Online]. Available: https://www.groenmonitor.nl/news/bouwland-areaal-heeft-45-winterbedekking

[51] H. Yang, F. Li, W. Wang, and K. Yu, “Estimating above-ground biomass of potato using random forest and optimized hyperspectral indices,” *Remote Sensing*, vol. 13, no. 12, 2021.

[52] ForFarmers, “”Vanggewas op droge grond nu snel vernietigen”,” 2019. [Online]. Available: https://www.forfarmers.nl/rundvee/melkvee/nieuws-kennis-en-advies/vanggewas-op-droge-grond-snel-vernietingen.aspx

[53] Koninklijk Nederlands Meteorologisch Instituut, “Achtergrondinformatie doorlopend potentieel neerslagoverschot.” [Online]. Available: https://www.knmi.nl/kennis-en-datacentrum/achtergrond/Achtergrondinformatie-doorlopend-potentieel-neerslagoverschot

Appendices

A Additional figures for model and calibration method validation

A.1 Method comparison for the basic fit functions

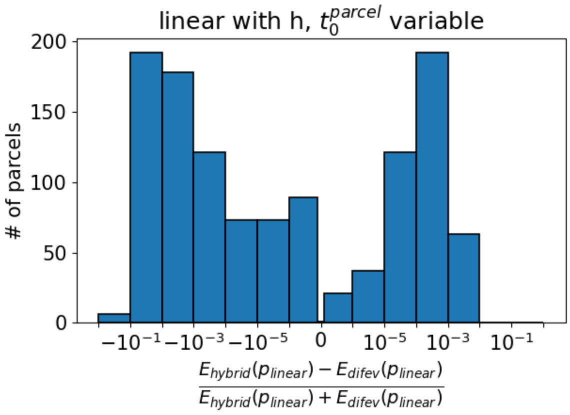

(a)

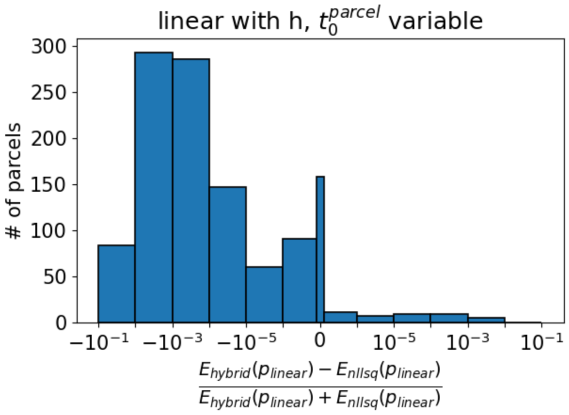

(b)

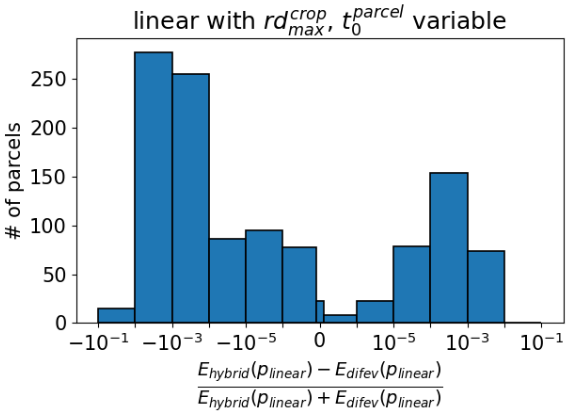

(c)

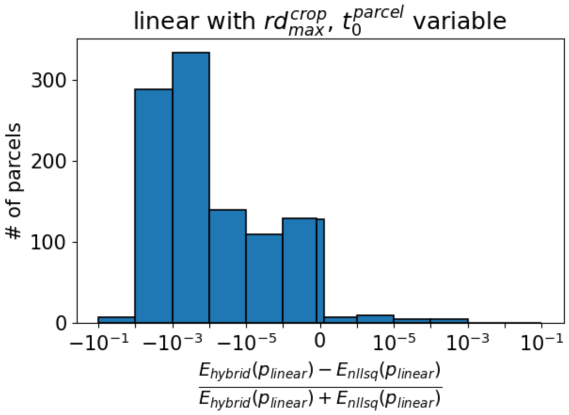

(d)

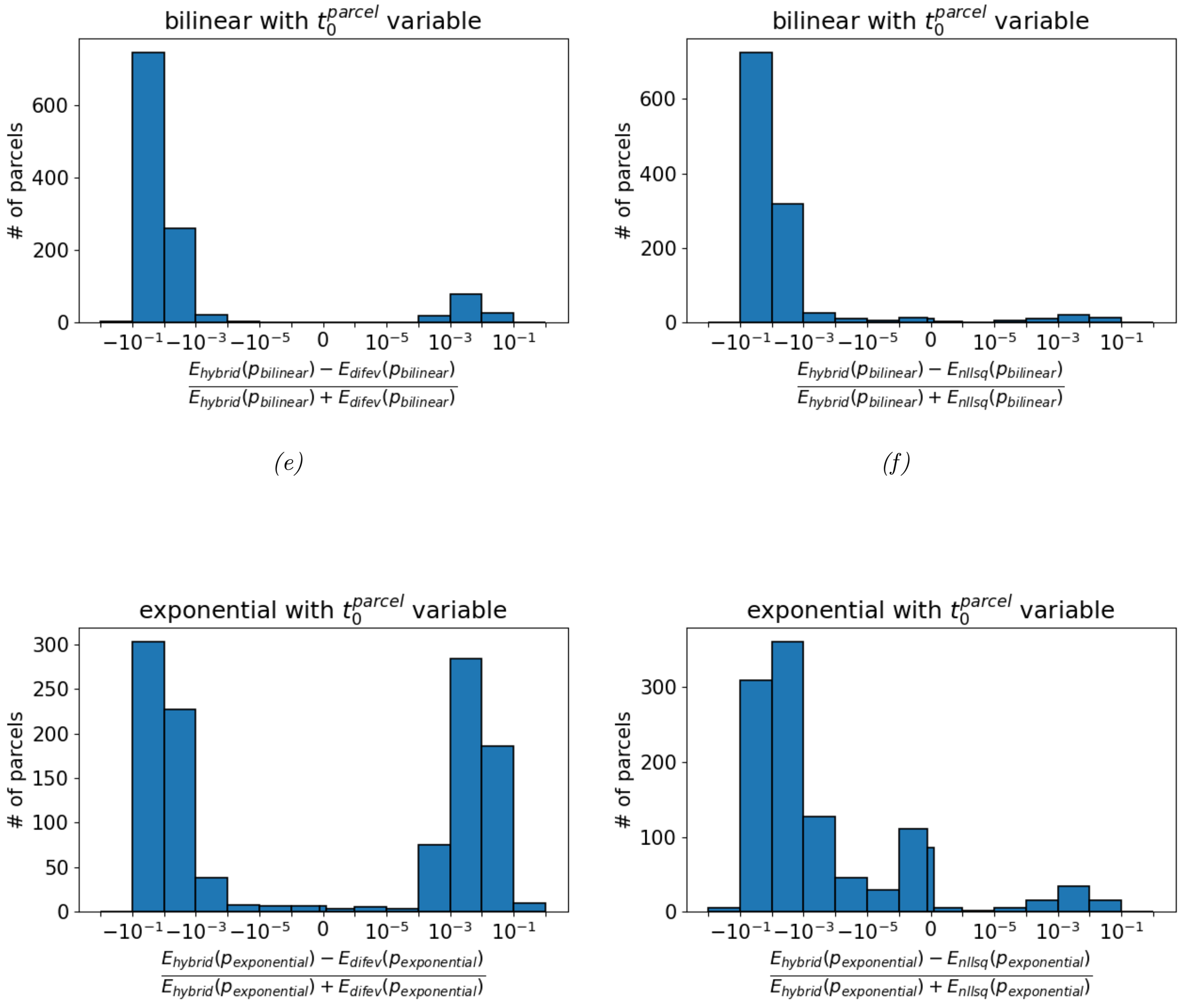
bilinear with t_0^{parcel} variable
# of parcels
0
200
400
600
-10^{-1} -10^{-3} -10^{-5} 0 10^{-5} 10^{-3} 10^{-1}
$\frac{E_{hybrid}(p_{bilinear}) - E_{difev}(p_{bilinear})}{E_{hybrid}(p_{bilinear}) + E_{difev}(p_{bilinear})}$
bilinear with t_0^{parcel} variable
# of parcels
0
200
400
600
-10^{-1} -10^{-3} -10^{-5} 0 10^{-5} 10^{-3} 10^{-1}
$\frac{E_{hybrid}(p_{bilinear}) - E_{nllsq}(p_{bilinear})}{E_{hybrid}(p_{bilinear}) + E_{nllsq}(p_{bilinear})}$
exponential with t_0^{parcel} variable
# of parcels
0
50
100
150
200
250
300
-10^{-1} -10^{-3} -10^{-5} 0 10^{-5} 10^{-3} 10^{-1}
$\frac{E_{hybrid}(p_{exponential}) - E_{difev}(p_{exponential})}{E_{hybrid}(p_{exponential}) + E_{difev}(p_{exponential})}$
exponential with t_0^{parcel} variable
# of parcels
0
100
200
300
-10^{-1} -10^{-3} -10^{-5} 0 10^{-5} 10^{-3} 10^{-1}
$\frac{E_{hybrid}(p_{exponential}) - E_{nllsq}(p_{exponential})}{E_{hybrid}(p_{exponential}) + E_{nllsq}(p_{exponential})}$

(e) *(f)*

(g) *(h)*

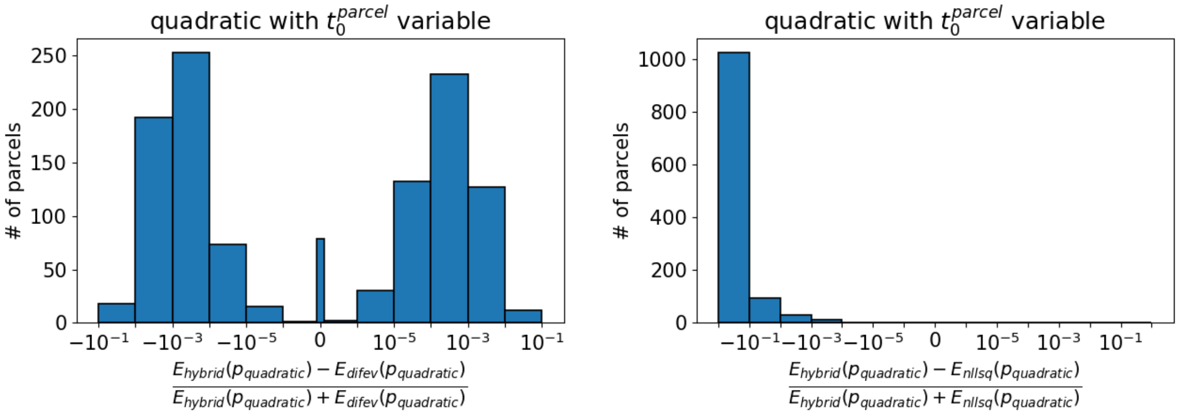

(i) (j)

Figure 28: Comparison between the performance of the three calibration methods for the basic fit functions. In each row, the left and right subfigures respectively show the relative difference in error statistics between the hybrid method and differential evolution and between differential evolution and non-linear least squares. The fit functions for t_0^{parcel} variable and t_2^{crop} variable have been left out as they are treated in section 5.1. The 2019 data from the 1167 potato parcels in the validation region described in section 2.5 was used for these images. The middle, thinner bar contains values within 10^{-9} of zero, reflecting parcels where there was no significant difference in fit quality.

A.2 Hybrid parameter configuration validation

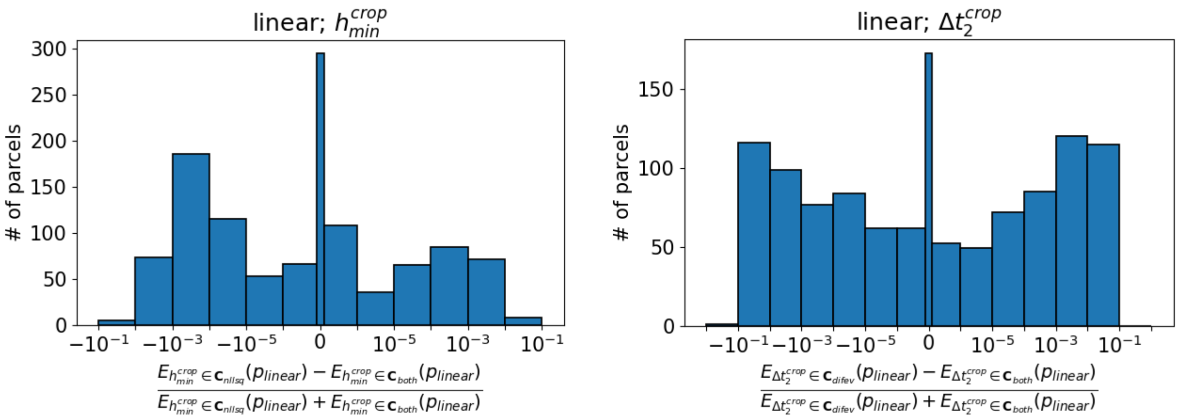

(a) (b)

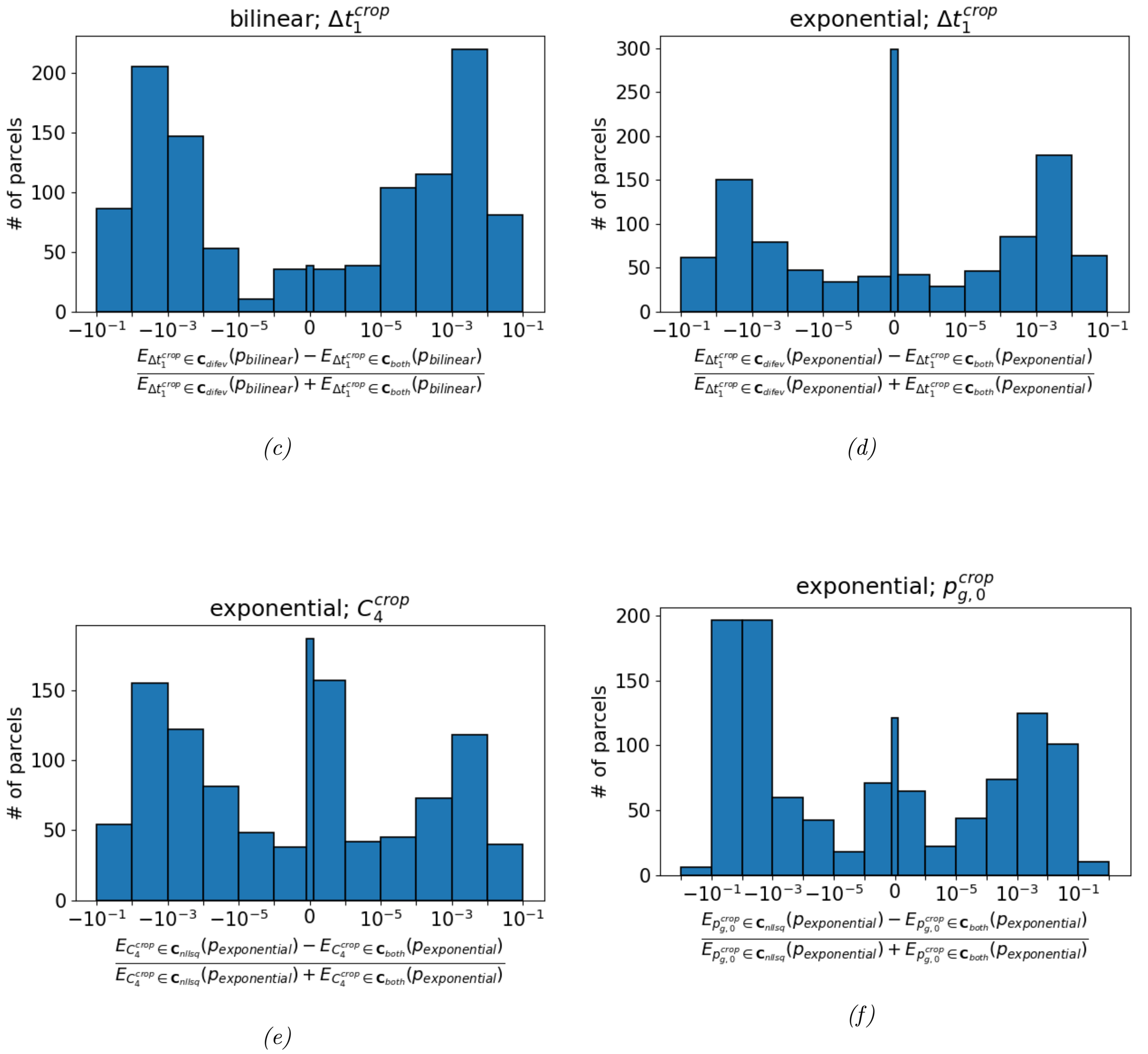

(c) *(d)*

(e) *(f)*

Figure 29: Validation of the parameter configuration (i.e. the choice of sub-algorithm used to fit each parameter within the hybrid method) for the fit parameters $C_4^{crop}, p_{g,0}^{crop}, \Delta t_1^{crop}$ and Δt_2^{crop}. See section 5.3 for an analysis of these figures. Each subfigure shows an investigation of the configuration of one fit parameter $C \in \mathbf{C}$. The x-axis shows the relative difference between the error statistics of fits generated by the hybrid method with $C \in \mathbf{C}_{both}$ and either $C \in \mathbf{C}_{nllsq}$ or $C \in \mathbf{C}_{difev}$, depending on the a priori guess formulated in section 4.4.2 (see also label in the x-axis). The 2019 data from 1167 potato parcels in the validation region described in section 2.5 was used for these images. The basic fit functions were used for this investigation, i.e. t_0 was fitted in each figure, but the models were otherwise kept in the simplest form that included the relevant parameter. In each histogram, negative values signify that the a priori assumption gave a better result than $C \in \mathbf{C}_{both}$, whereas positive values signify the opposite. The middle, thinner bar contains values within 10^{-9} of zero, representing parcels where there was no significant difference in fit quality.

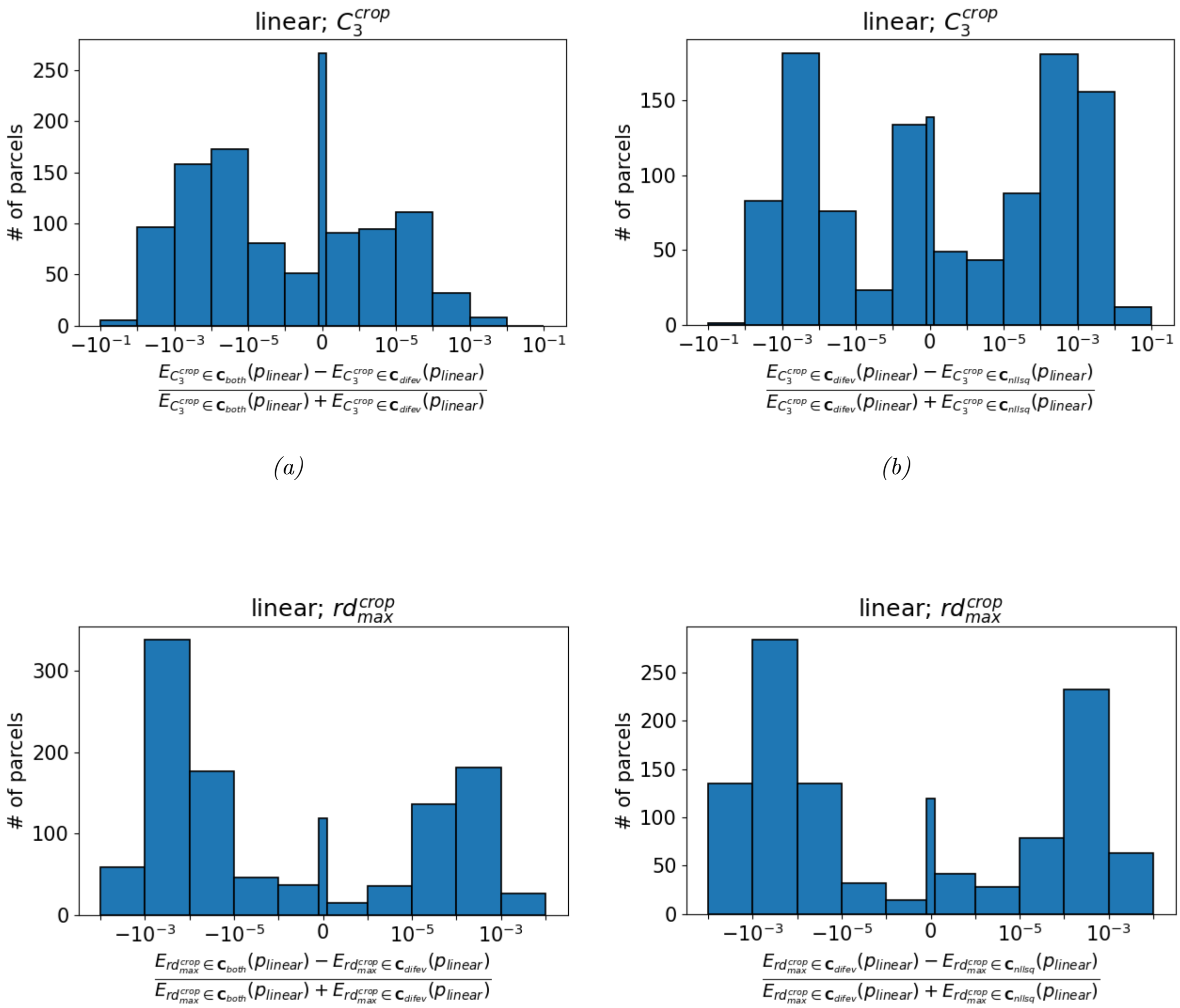
linear; C_3^{crop}
# of parcels
250
200
150
100
50
0
-10^{-1}
-10^{-3}
-10^{-5}
0
10^{-5}
10^{-3}
10^{-1}
$\frac{E_{C_3^{crop} \in \mathbf{c}_{both}}(p_{linear}) - E_{C_3^{crop} \in \mathbf{c}_{difev}}(p_{linear})}{E_{C_3^{crop} \in \mathbf{c}_{both}}(p_{linear}) + E_{C_3^{crop} \in \mathbf{c}_{difev}}(p_{linear})}$
linear; C_3^{crop}
# of parcels
150
100
50
0
-10^{-1}
-10^{-3}
-10^{-5}
0
10^{-5}
10^{-3}
10^{-1}
$\frac{E_{C_3^{crop} \in \mathbf{c}_{difev}}(p_{linear}) - E_{C_3^{crop} \in \mathbf{c}_{nllsq}}(p_{linear})}{E_{C_3^{crop} \in \mathbf{c}_{difev}}(p_{linear}) + E_{C_3^{crop} \in \mathbf{c}_{nllsq}}(p_{linear})}$
linear; rd_{max}^{crop}
# of parcels
300
200
100
0
-10^{-3}
-10^{-5}
0
10^{-5}
10^{-3}
$\frac{E_{rd_{max}^{crop} \in \mathbf{c}_{both}}(p_{linear}) - E_{rd_{max}^{crop} \in \mathbf{c}_{difev}}(p_{linear})}{E_{rd_{max}^{crop} \in \mathbf{c}_{both}}(p_{linear}) + E_{rd_{max}^{crop} \in \mathbf{c}_{difev}}(p_{linear})}$
linear; rd_{max}^{crop}
# of parcels
250
200
150
100
50
0
-10^{-3}
-10^{-5}
0
10^{-5}
10^{-3}
$\frac{E_{rd_{max}^{crop} \in \mathbf{c}_{difev}}(p_{linear}) - E_{rd_{max}^{crop} \in \mathbf{c}_{nllsq}}(p_{linear})}{E_{rd_{max}^{crop} \in \mathbf{c}_{difev}}(p_{linear}) + E_{rd_{max}^{crop} \in \mathbf{c}_{nllsq}}(p_{linear})}$

(a)

(b)

(c)

(d)

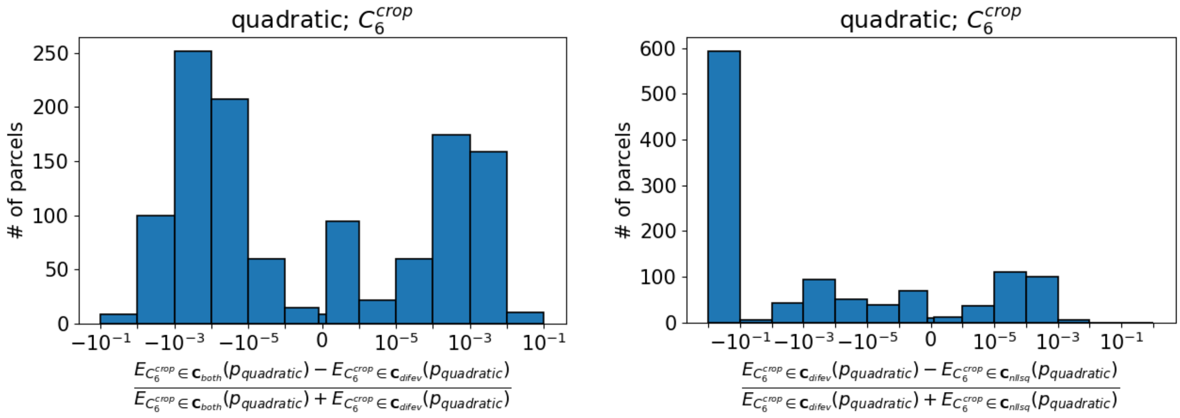

(e) *(f)*

Figure 30: Investigation of the parameter configuration (i.e. the choice of sub-algorithm used to fit a given parameter within the hybrid method) of the hybrid method for the more convoluted fit parameters C_3^{crop}, rd_{max}^{crop} and C_6^{crop}. See section 5.3 for an analysis of these figures. Each row of two subfigures shows an investigation of the configuration of one these fit parameters $C \in \mathbf{C}$. The x-axis shows the relative difference between the error statistics of fits generated by the hybrid method with $C \in \mathbf{C}_{both}$ and $C \in \mathbf{C}_{difev}$ (left), and between $C \in \mathbf{C}_{difev}$ and $C \in \mathbf{C}_{nllsq}$ (right). The 2019 data from 1167 potato parcels in the validation region described in section 2.5 was used for these images. t_0 was fitted in all figures, but the fits were otherwise kept in the simplest form that included the relevant parameter. In each histogram, negative values signify that $C \in \mathbf{C}_{both}$ gives better performance than $C \in \mathbf{C}_{difev}$ (left) or that $C \in \mathbf{C}_{difev}$ gives better performance than $C \in \mathbf{C}_{nllsq}$ (right), whereas positive values signify the opposite. The middle, thinner bar contains values within 10^{-9} of zero, representing parcels where there was no significant difference in fit quality. Notice that performance is almost equal in all cases for rd_{max}^{crop} and C_3^{crop}. On the other hand, non-linear least squares performs much more poorly than the other two for C_5^{crop} and C_6^{crop}.

A.3 Comparison between fit functions

Figure 31 shows scatter plots that correlate quality improvement obtained with a certain model extension with the values of the parameters it introduces. In figures 31a- 31d, we see that the exponential model gives a consistent, significant increase of the fit quality compared to the base, linear case. However, this is similar to the bilinear case we described in section 6.2. Δt_1^{crop} is very close to the minimum of 15 days. This indicates that the model is only fitted to a very short part of the time series.

Note the peculiar horizontal lines in C_4^{crop} in figure 31c. The error function actually keeps decreasing as $C_4^{crop} \to \infty$. However, the derivative will go so close to zero that non-linear least squares believes it has converged. The lines are a result of a fixed number of steps before convergence is achieved.

In figures 31e and 31f, the scatter plots for the quadratic method are shown. We see some very clear clusters with $|C_5^{crop}| > 10^1$ that mostly yield a worse quality than the linear base case. This happens because the normalized RVI $v_i - v_0$ is almost exclusively negative for these parcels. As a result, the second term in the square root of equation (3.35) becomes zero, which reduced the model to the linear model. However, due to the additional fit parameter C_5^{crop}, this model is more difficult to fit for differential evolution, leading to a lower quality in most cases.

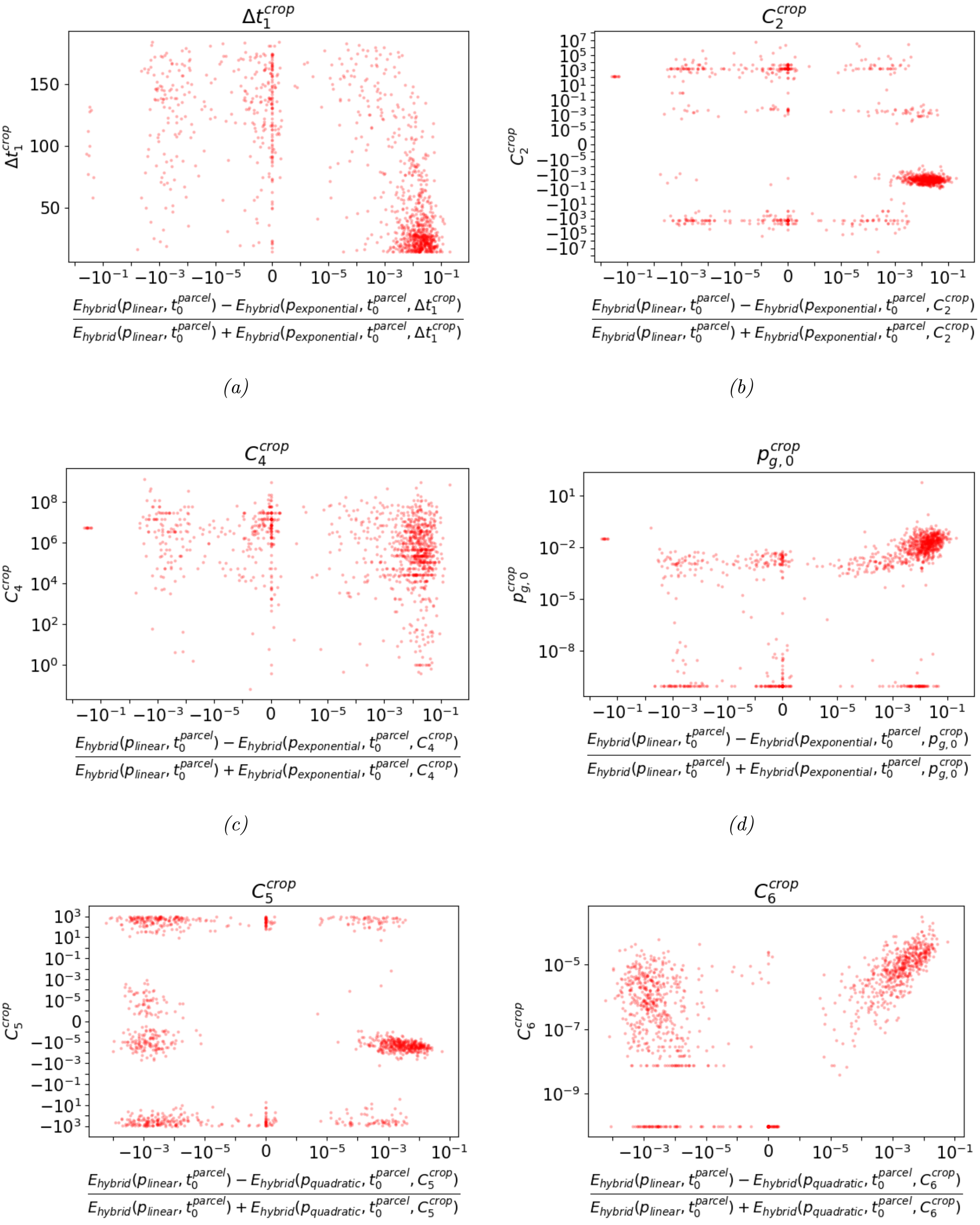

(a) *(b)*

(c) *(d)*

(e) *(f)*

Figure 31: Comparison of the performance of the basic fit functions. Each model is compared to the base case with p^{crop} and g linear, t_0^{crop} variable and all other parameters fixed. The quality is plotted against the value of the parameters that were added to model compared to the base case. This way, any correlations between improved quality and the value of the fit parameters is visualised.

B Additional time series

B.1 Time series of potato parcels separated by irrigation

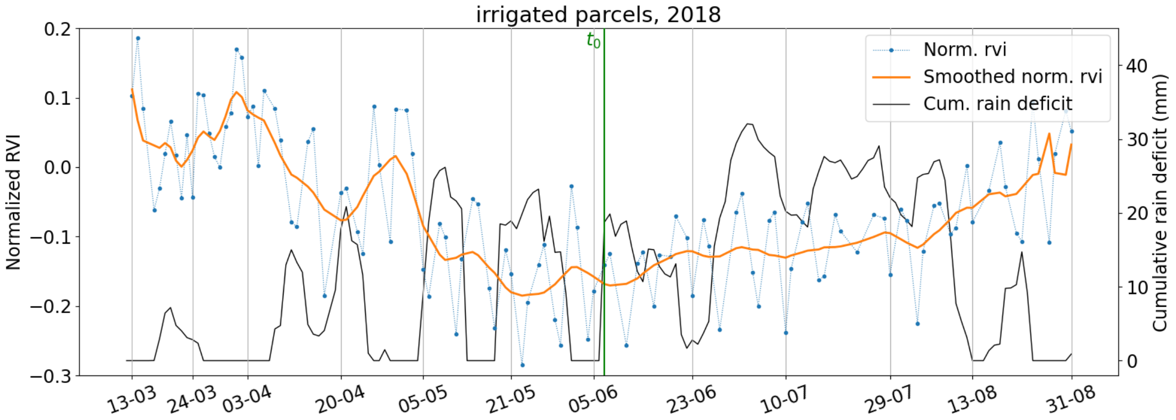

(a)

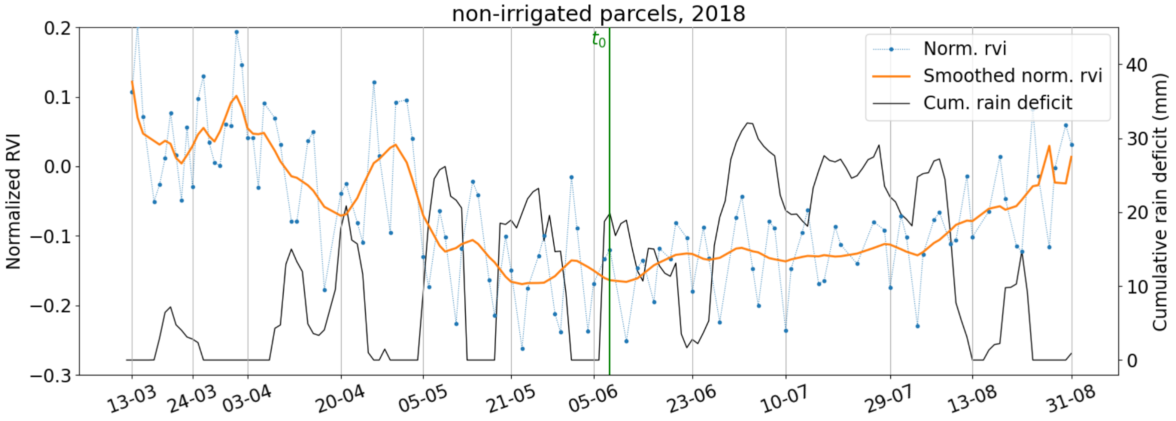

(b)

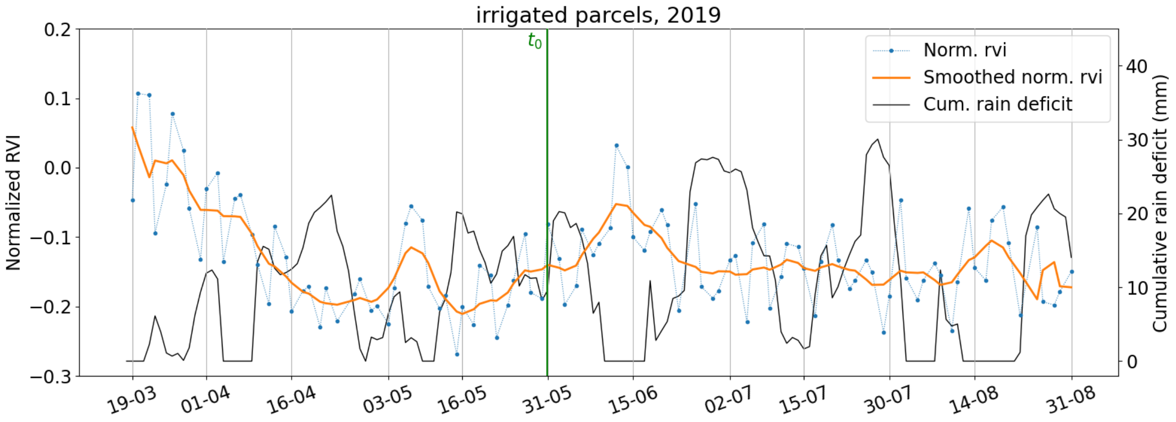
irrigated parcels, 2019
t_0
Norm. rvi
Smoothed norm. rvi
Cum. rain deficit
Normalized RVI
0.2
0.1
0.0
−0.1
−0.2
−0.3
Cumulative rain deficit (mm)
40
30
20
10
0
19-03
01-04
16-04
03-05
16-05
31-05
15-06
02-07
15-07
30-07
14-08
31-08

(c)

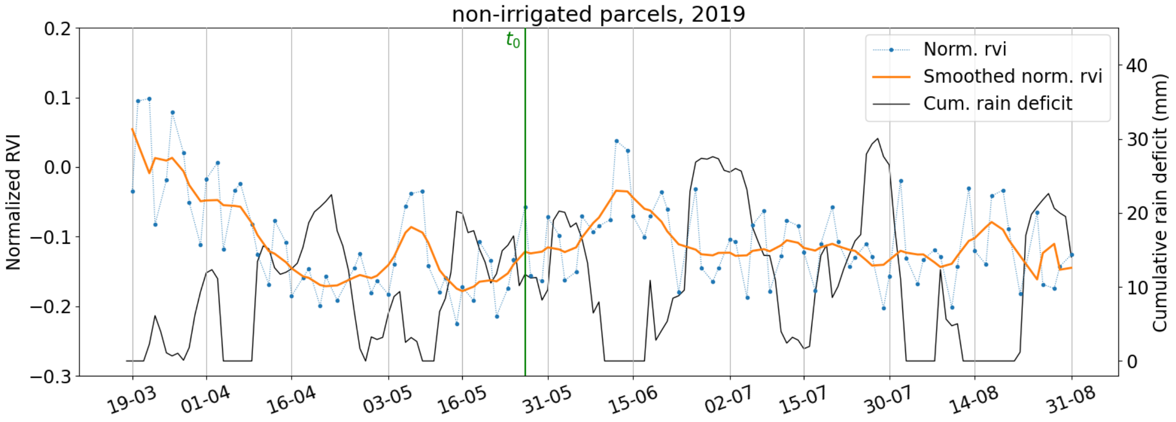
non-irrigated parcels, 2019
t_0
Norm. rvi
Smoothed norm. rvi
Cum. rain deficit
Normalized RVI
0.2
0.1
0.0
−0.1
−0.2
−0.3
Cumulative rain deficit (mm)
40
30
20
10
0
19-03
01-04
16-04
03-05
16-05
31-05
15-06
02-07
15-07
30-07
14-08
31-08

(d)

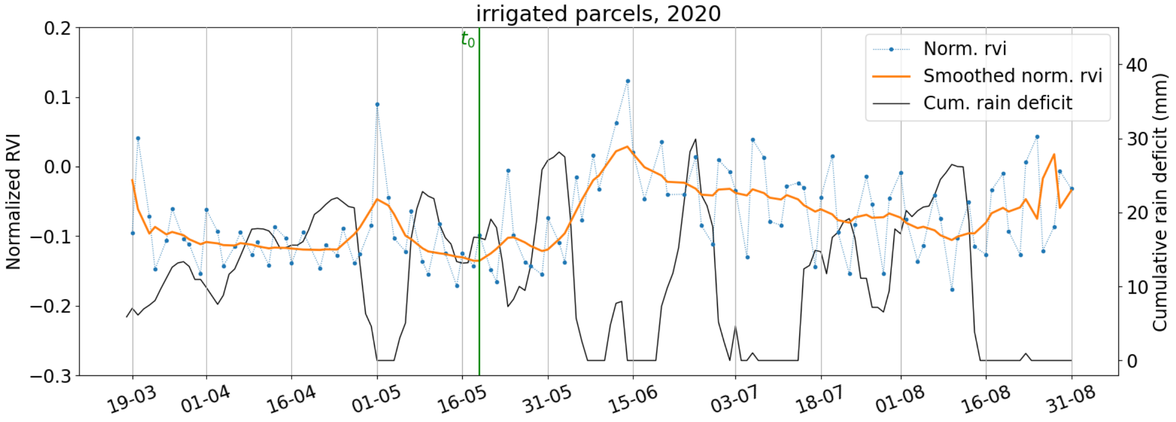
irrigated parcels, 2020
t_0
Norm. rvi
Smoothed norm. rvi
Cum. rain deficit
Normalized RVI
0.2
0.1
0.0
−0.1
−0.2
−0.3
Cumulative rain deficit (mm)
40
30
20
10
0
19-03
01-04
16-04
01-05
16-05
31-05
15-06
03-07
18-07
01-08
16-08
31-08

(e)

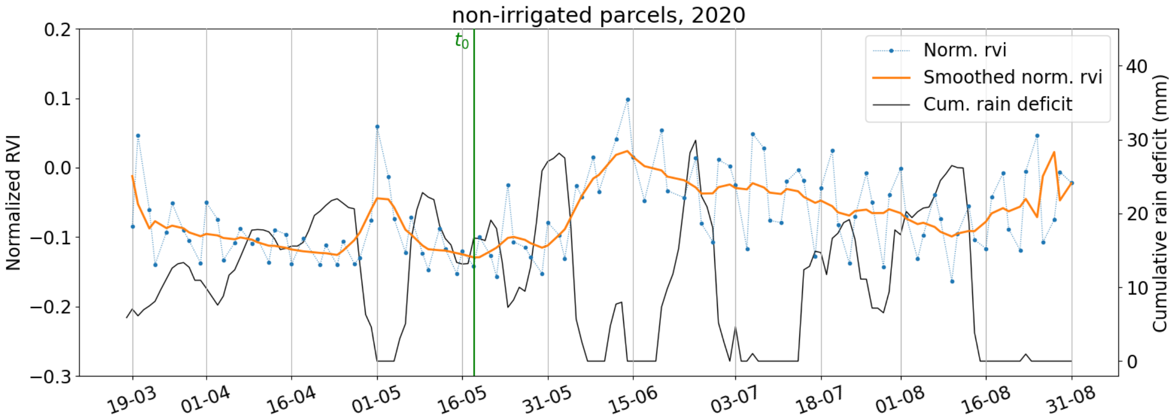

(f)

Figure 32: Average time series of parcels for the years 2018, 2019 and 2020, grouped by whether they are marked as irrigated by the validation data. The line marked t_0 *represents the median in each cluster of* t_0^{parcel} *according to the base fit function (*p^{crop}*, g linear,* t_0^{parcel} *variable, the other fit parameters constant).*

B.2 Average time series of corn parcels

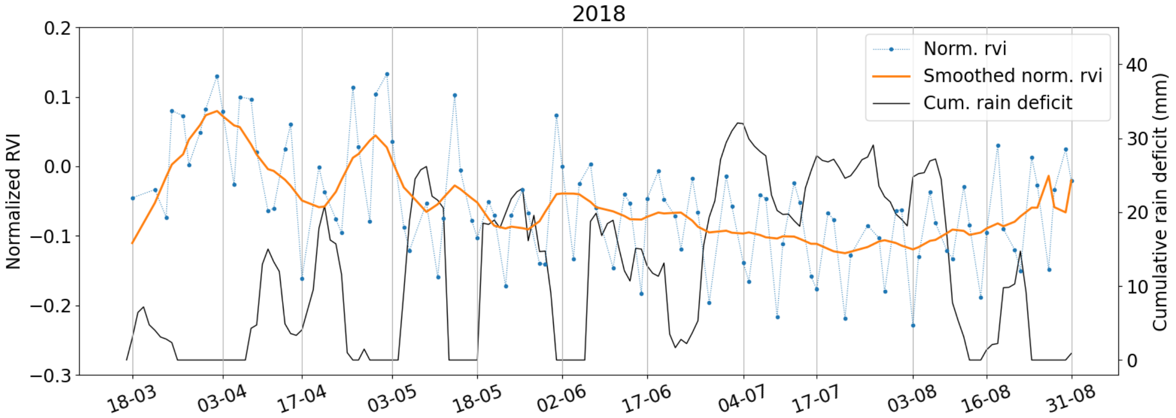

(a)

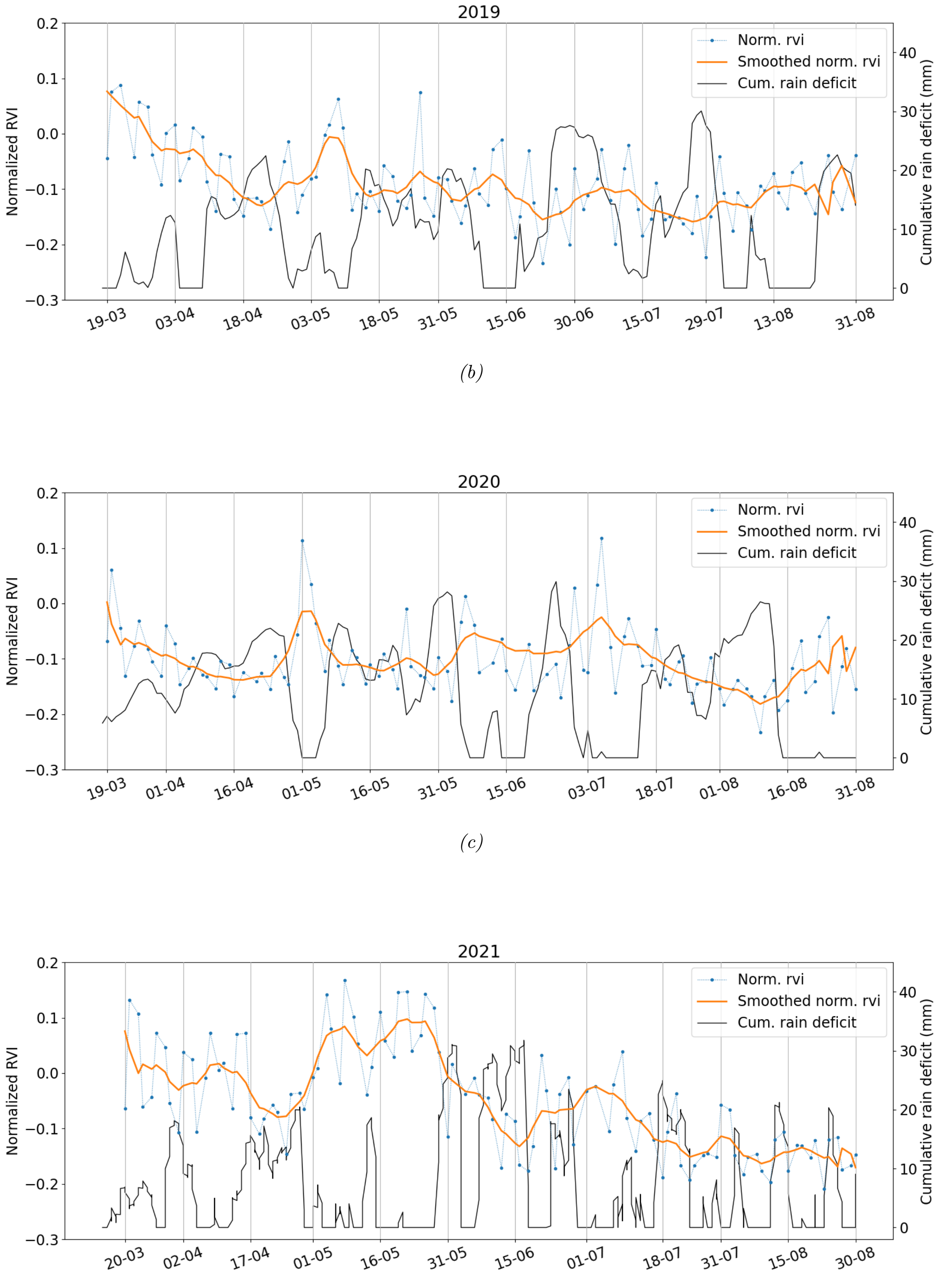

(b)

(c)

(d)

Figure 33: Average time series over all corn parcels in the validation region for each year.

C Additional clustering investigations

C.1 Analysis of clusters based on C_1^{crop} and C_3^{crop} in 2019 and 2021

C.1.1 2019

Figure 34 shows the average time series of the six clusters in C_1^{crop} and C_3^{crop} of 2019. These six clusters are defined in figure 19. The number of parcels in each cluster and correlation with irrigation is given in table 4 of section 7.1.

The most interesting feature of the clusters of 2019 is the considerable size of the cluster 4 and 5. These clusters are characterized by $C_1^{crop} < 10^{-6}$. This can be explained as follows. In figures 34e and 34f, we see that the median t_0^{parcel} is significantly higher than that of the other clusters. In fact, it lies behind the bump in RVI around the middle of June. After this point, the RVI remains approximately constant, which explains the low C_1^{crop}. Indeed, the RVI of the other years does not remain this constant during the last section of the growth phase. Hence, these years will not have a significant number of parcels similar to cluster 4 and 5 of 2019.

For the other clusters, it seems the distinction is largely made based on the position of t_0^{crop}. Cluster 1, with lower C_3^{crop} than cluster 0, avoids the bump at the beginning of April, as the steep slope lies within a region of non-zero (though not particularly high) rain deficit. Similarly, clusters 2 and 3, with even lower C_3^{crop}, avoid the increase in RVI right after the April bump, as that coincides with a period of high rain deficit. It seems that the clusters with low C_3^{crop} correlate with greater inhibition of RVI during the rain deficits in May and April. This would be consistent with our similar findings for 2018 and 2020. However, it is not supported by the correlation the irrigation validation data, as can be seen in table 4.

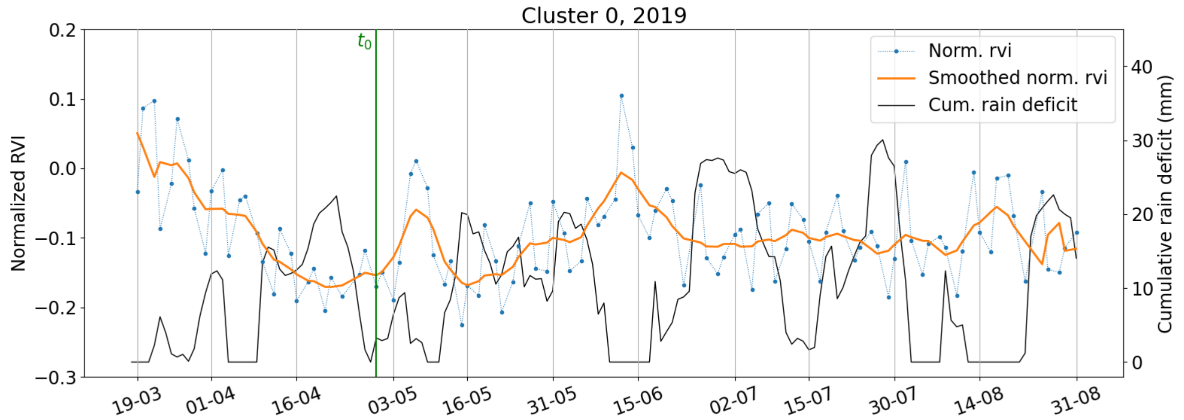

(a)

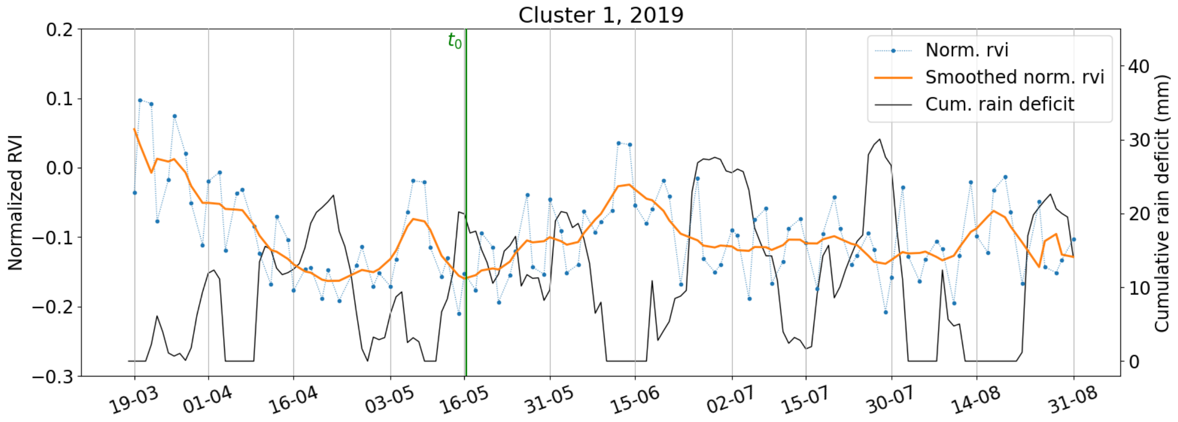
Cluster 1, 2019
t_0
Norm. rvi
Smoothed norm. rvi
Cum. rain deficit
Normalized RVI
Cumulative rain deficit (mm)
0.2
0.1
0.0
−0.1
−0.2
−0.3
0
10
20
30
40
19-03
01-04
16-04
03-05
16-05
31-05
15-06
02-07
15-07
30-07
14-08
31-08

(b)

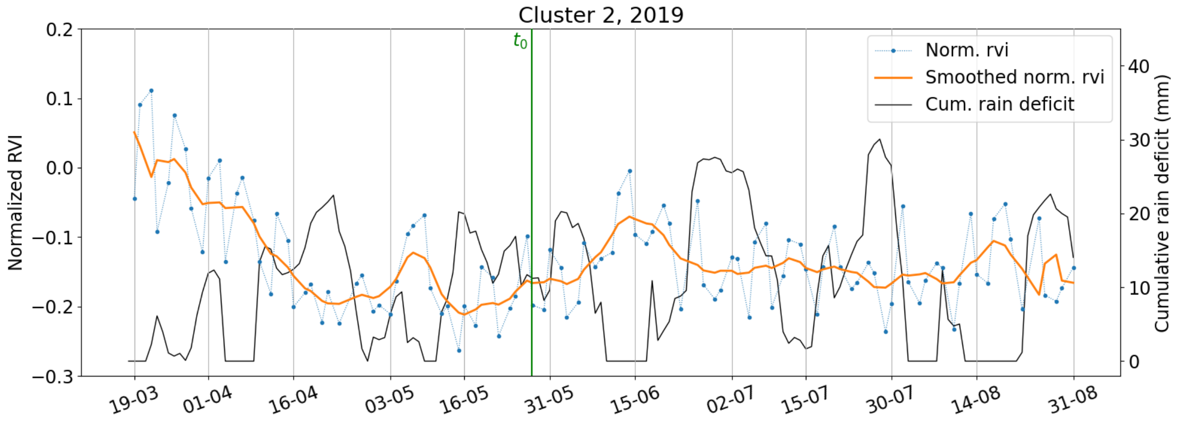
Cluster 2, 2019
t_0
Norm. rvi
Smoothed norm. rvi
Cum. rain deficit
Normalized RVI
Cumulative rain deficit (mm)
0.2
0.1
0.0
−0.1
−0.2
−0.3
0
10
20
30
40
19-03
01-04
16-04
03-05
16-05
31-05
15-06
02-07
15-07
30-07
14-08
31-08

(c)

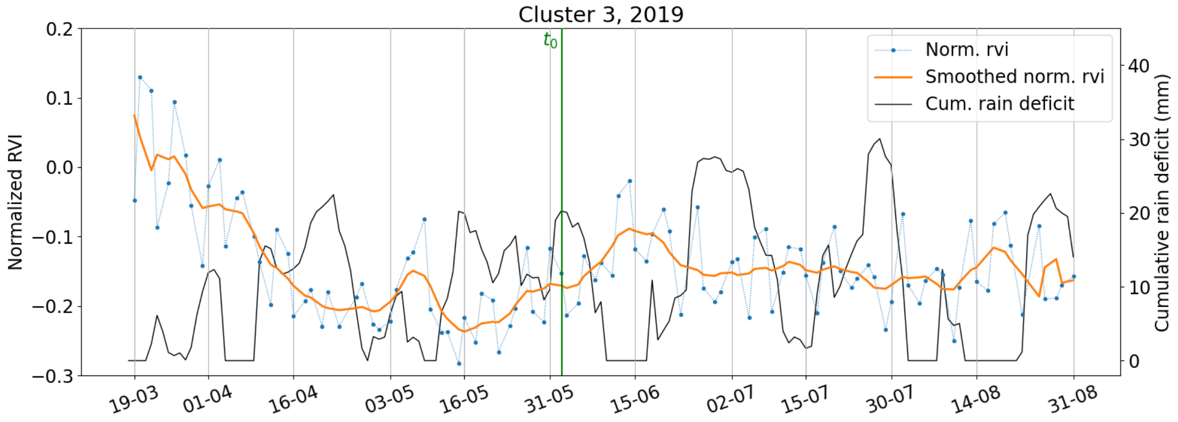
Cluster 3, 2019
t_0
Norm. rvi
Smoothed norm. rvi
Cum. rain deficit
Normalized RVI
Cumulative rain deficit (mm)
0.2
0.1
0.0
−0.1
−0.2
−0.3
0
10
20
30
40
19-03
01-04
16-04
03-05
16-05
31-05
15-06
02-07
15-07
30-07
14-08
31-08

(d)

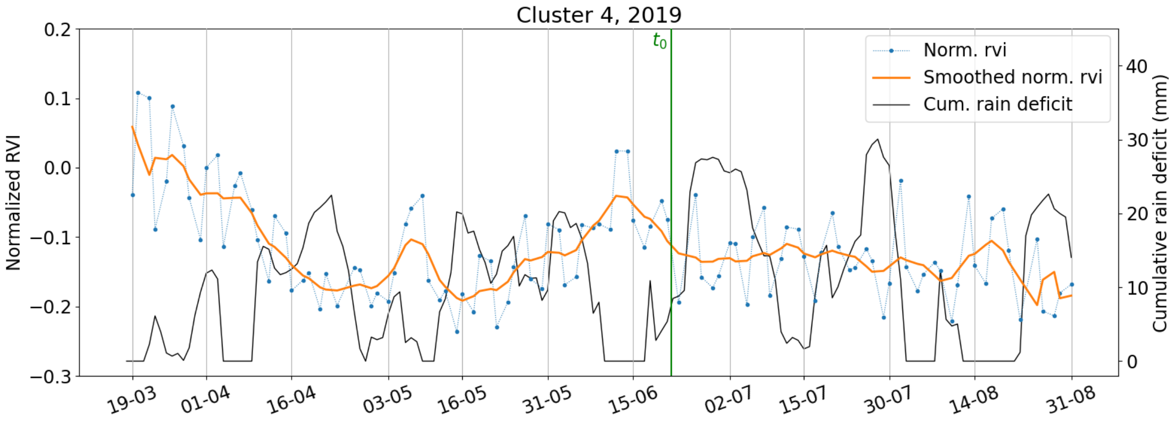

(e)

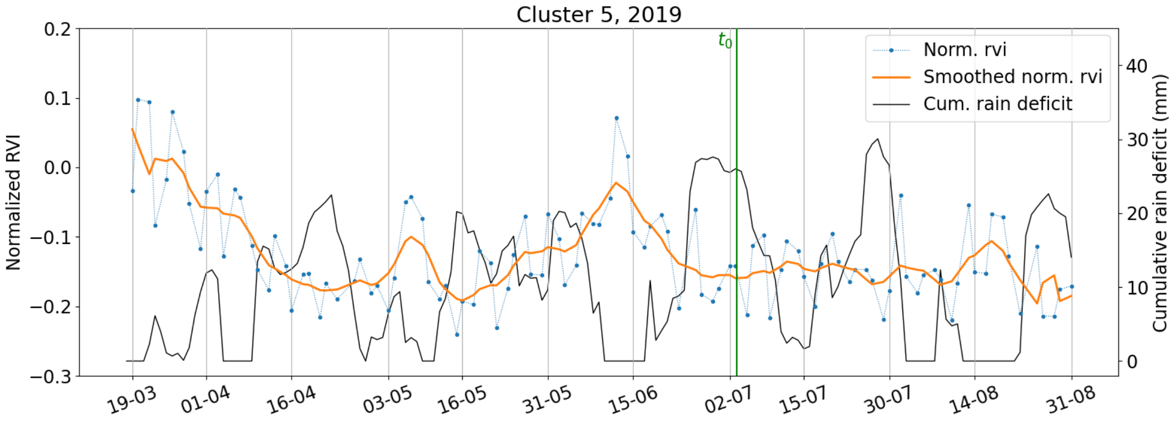

(f)

Figure 34: Average time series of parcels in all six clusters in C_1^{crop} and C_3^{crop} of 2019, see figure 16 for their definition. The line marked t_0 represents the median of t_0^{parcel} in each cluster.

C.1.2 2021

Figure 35 shows the average time series of the three significant clusters in C_1^{crop} and C_3^{crop} of 2021. These clusters are defined in figure 19. The number of parcels in each cluster and correlation with irrigation is given in table 4 of section 7.1. Note that cluster 3 is almost a factor 4 smaller than clusters 1 and 2.

t_0^{parcel} clearly seems to accumulate around the minima of of the time series. Yet, the deep valley around the 20 April seems to be largely avoided. This is likely because the RVI starts increasing there before the cumulative rain deficit goes down. The rest of the time series very nicely obeys that it only increases while precipitation deficit is low. Hence, a low C_3^{crop} can provide a good fit to this data. This is also the reason cluster 0 is so small in this year. The correlation with rain deficit is high, meaning that there will be very few parcels that are best modelled such a high C_3^{crop}.

This high correlation with precipitation deficit might actually be an indication that very little irrigation had taken place in 2021. This year was much wetter than the three previous years, so little irrigation was probably necessary. Hence, this result is in line with our expectations.

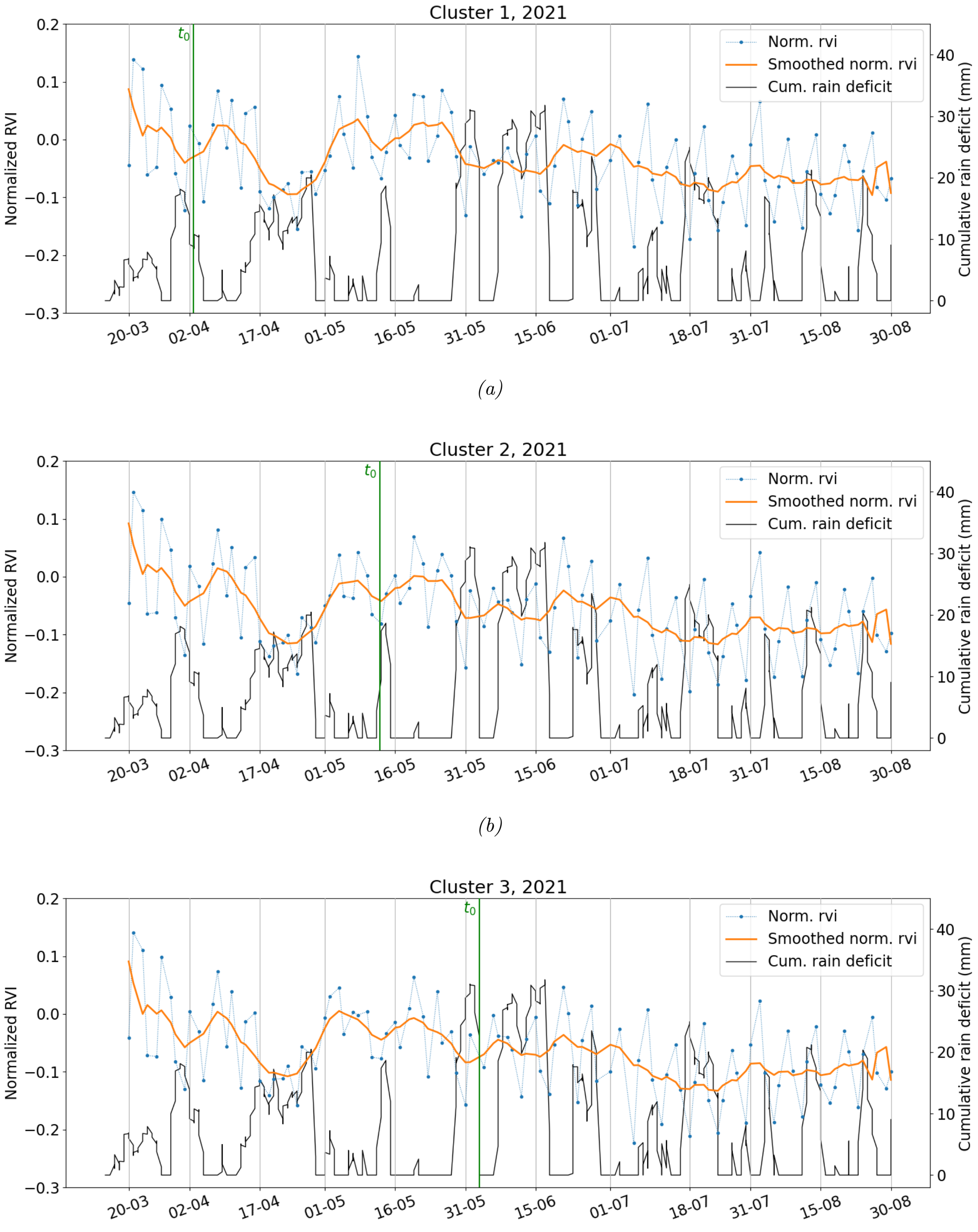

(a)

(b)

(c)

Figure 35: Average time series of parcels in the three significant clusters in C_1^{crop} *and* C_3^{crop} *of 2021, see figure 16 for their definition. The size of the clusters is given in table 4 The line marked* t_0 *represents the median of* t_0^{parcel} *in each cluster.*

C.2 clusters based on $t_0^{parcel} + \Delta t_1^{crop}$ and C_2^{crop} in 2018 and 2021

Figure 36 shows that the clustering of $t_0^{parcel} + \Delta t_1^{crop}$ is much less significant in especially 2018 than it was in 2019 and 2021 (see figure 21). Figure 37 shows the same definition for the clustering we used for 2019 and 2020. Clearly, this clustering makes much less sense for 2018 and 2021 than it does for the other two years. Especially in 2021, cluster 3 clearly consists of two groups in t_1^{parcel}, which could arguably be combined with the adjacent clusters. This further demonstrates what we already discovered in section 7.3: clusters in t_1^{parcel} vary each year. To be more precises, they mostly correlate with precipitation deficit, as the precipitation deficit dependent fluctuations in RVI have the most dominant influence over the model calibration.

The number of parcels in each cluster is given in 7. The irrigation rate of 2018 has two cluster with statistically significant (p-value < 0.05) deviation from the mean: cluster 2 (p-value $9.45 \cdot 10^{-3}$) and cluster 3 (p-value $1.57 \cdot 10^{-2}$). However, the clusters are rather small and therefore not all that useful.

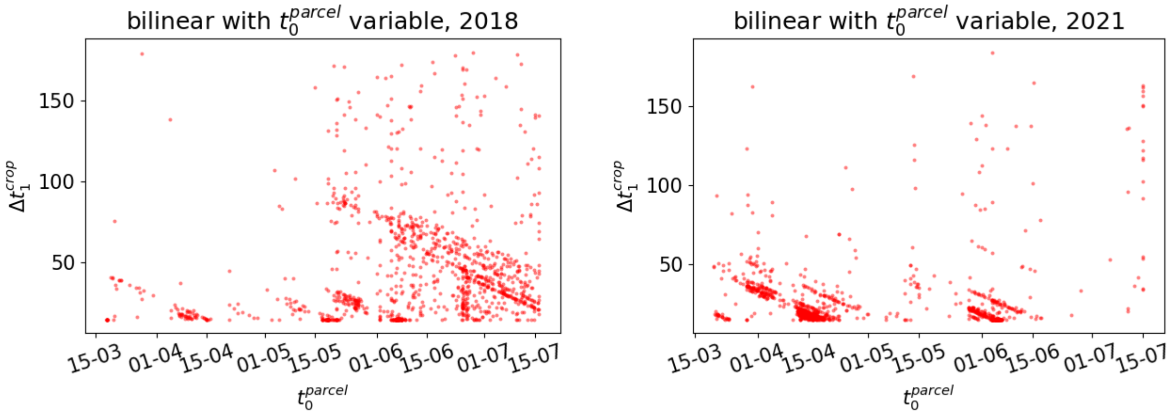

(a)

(b)

Figure 36: Scatter plots between parameters t_0^{parcel} and Δt_1^{crop} for the years 2018 and 2021. The model parameterization used to generate these images is defined by bilinear p^{crop} with t_0^{parcel} variable and all other parameters fixed. Especially for 2018, the diagonal lines indicating clustering of $t_0^{parcel} + \Delta t_1^{crop}$ are much more diverse than the ones for 2019 and 2020 in figure 21.

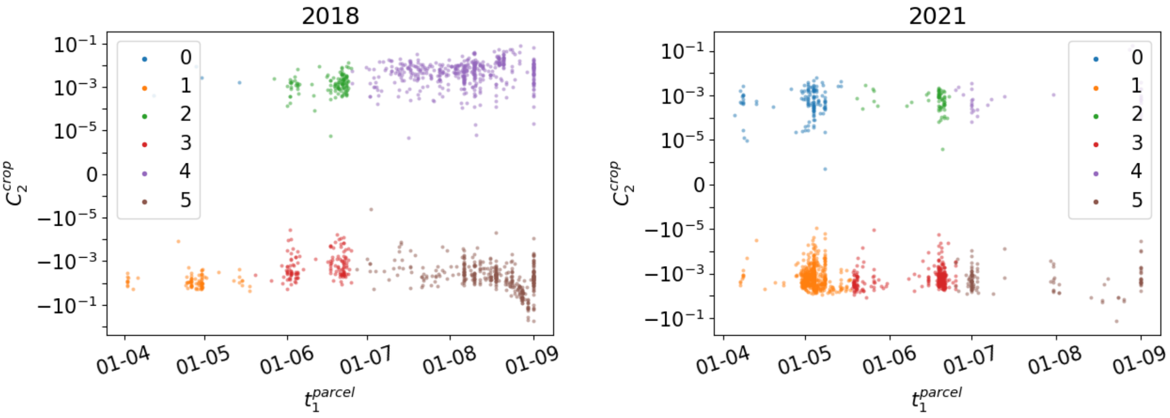

(a) *(b)*

Figure 37: Definition of clusters in the combination of C_2^{crop} and $t_1^{parcel} = t_0^{parcel} + \Delta t_1^{crop}$ for 2018 and 2021.

Table 7: The number of parcels and percentage of irrigated parcels (according to the validation data) in each of the clusters defined in figure 37. Note that there is no irrigation data for 2021.

	2018		2021
Cluster	# parcels	% irrigated	# parcels
0	4	0.0	127
1	87	19.54	497
2	116	35.34	64
3	135	18.52	274
4	450	26.89	35
5	375	24.8	113
all	1167	25.45	1111

C.3 Parameters with less meaningful clusters

Figure 38 shows the two scatter plots of the base case (p^{crop}, g linear, t_0^{parcel} variable) that were not investigated in section 7.1. Here, we see that t_0^{parcel} has no significant correlation with either of the other model parameters.

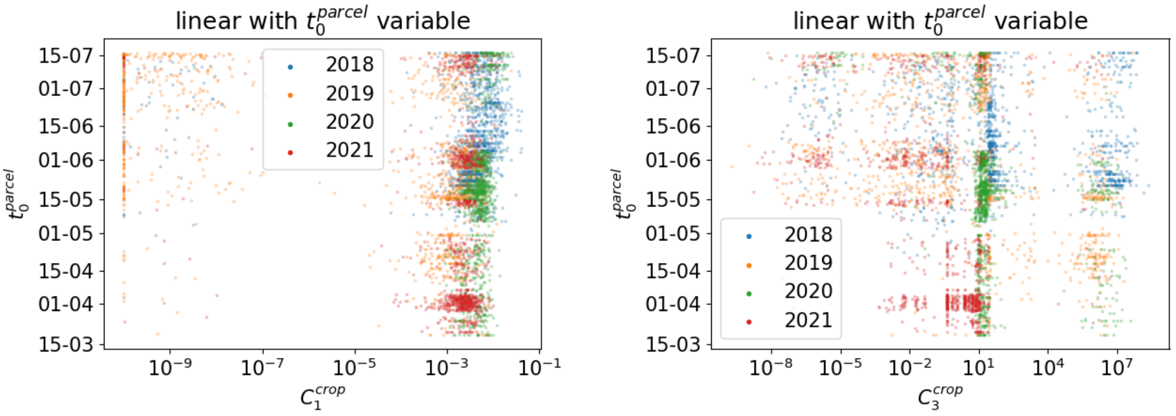

(a) *(b)*

Figure 38: Scatter plots of all combinations of the three parameters of the base fit function: p^{crop} and g linear with t_0^{parcel} variable and all other parameters fixed. The scatter plot between C_1^{crop} and C_3^{crop} is given in figure 16b.

Figure 39 shows scatter plots for linear p^{crop} and g with t_0^{parcel} and rd_{max}^{crop} variable and all other parameters fixed. These figures show some interesting features of calibration using rd_{max}^{crop}.

Firstly, comparing figure 39a to figure 16a, we see that the addition of rd_{max}^{crop} has made the gap the four clusters in $C_1^{crop} > 10^{-6}$ collapse into 1. The gap around 10^0 has disappeared, and both extremely high C_3^{crop} and extremely low C_3^{crop} no longer seems to occur. This makes some sense, as rd_{max}^{crop} offers an alternative method to handle measurements that correlate poorly with precipitation deficit. This allows values for C_3^{crop} around 10^0, which indicate very high correlation with precipitation deficit. This indicates that C_3^{crop} might be much better capable of modelling the correlation with rain deficit when rd_{max}^{crop} is part of the model as well. Hence, it can be interesting for future research to further investigate the usage of rd_{max}^{crop}, especially once the definition of v_0 has been fixed to allow proper modelling with h^{crop}.

Secondly, figure 39c shows some interesting arcs in $(C_3^{crop}, rd_{max}^{crop})$. These can be understood as follows: as rd_{max}^{crop} increases, the same behaviour is best modelled with a lower C_3^{crop}. Hence, these arcs all model a very similar behaviour. This seems to imply that the correlation with rain deficits is even more homogeneous than figure 39a would suggest. For instance, 2021 seems to be divisible in about three different behaviour types, along with a large cluster at $rd_{max}^{crop} \approx 0$.

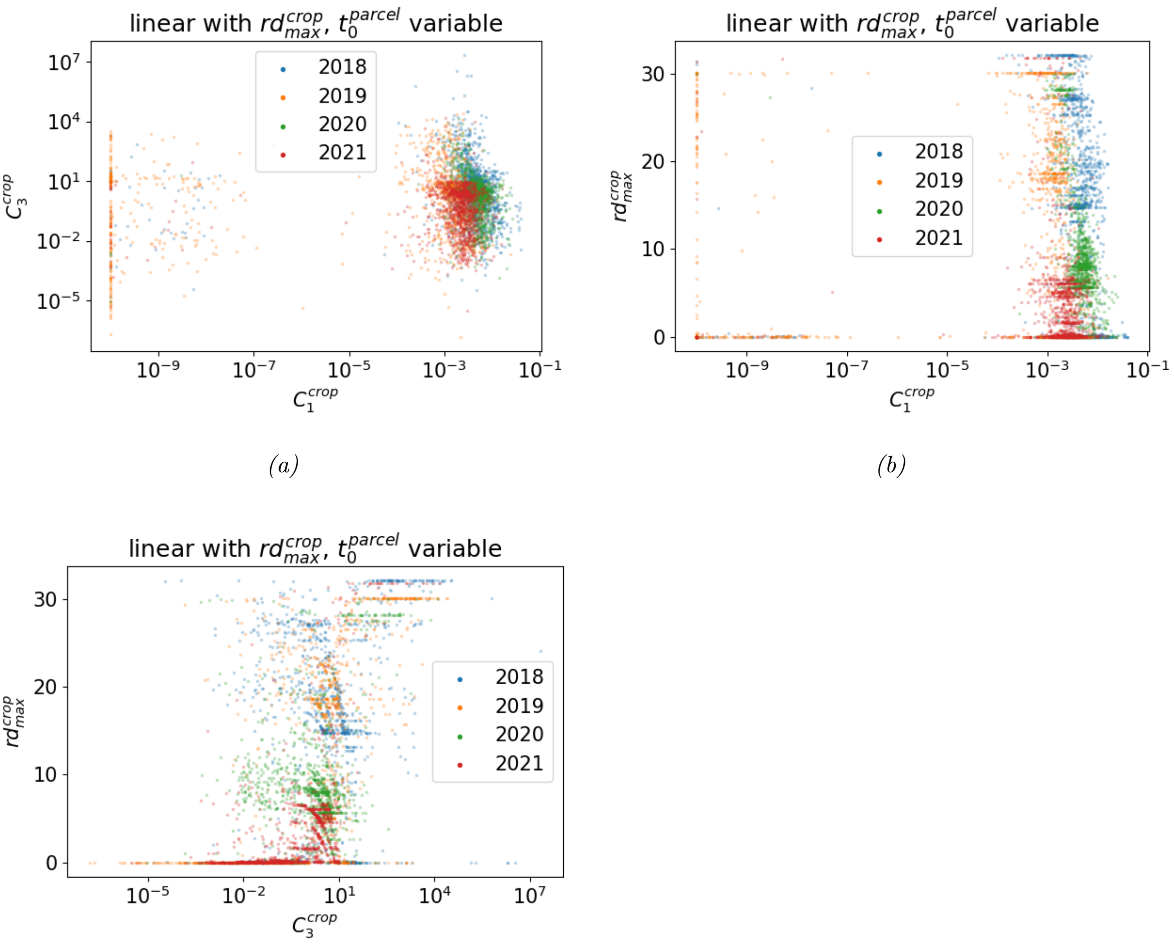

(a)

(b)

(c)

Figure 39: Scatter plots of all combinations of the three parameters C_1^{crop}, C_3^{crop} and rd_{max}^{crop} of the fit function defined by p^{crop} and g linear with t_0^{parcel} and rd_{max}^{crop} variable and all other parameters fixed.

Figure 40 shows scatter plots for linear p^{crop} and g with t_0^{parcel} and h_{min}^{crop} variable and all other parameters fixed. The thorough investigation of the behaviour of h_{min}^{crop} in section 7.2 revealed some interesting features of the RVI time series, as well as a statistically significant correlation with the irrigation validation data. Yet, it shows no correlation with C_1^{crop} in figure 40b. On the other hand, figure 40c shows some clear vertical lines in $(C_3^{crop}, h_{min}^{crop})$ for $h_{min}^{crop} < 1$, while C_3^{crop} has much greater spread $h_{min}^{crop} = 1$. This is to be expected, as h^{crop} depends on C_3^{crop} when $h_{min}^{crop} < 1$.

Interestingly, comparing figure 40a to figure 16a, the cluster for very small C_3^{crop} has disappeared. This seems to indicate that most of these parcels are calibrated by $h_{min}^{crop} < 1$. Yet, cluster 3 of 2019 (figure 34d) does not show the same behaviour as the $h_{min}^{crop} < 1$ cluster in figure 20b; i.e. it does not at all have a relatively high normalized RVI for most of the time series. One possibility is that h_{min}^{crop} is simply very close to 1 for these parcels, which is enough to push C_3^{crop} up to one of the higher clusters.

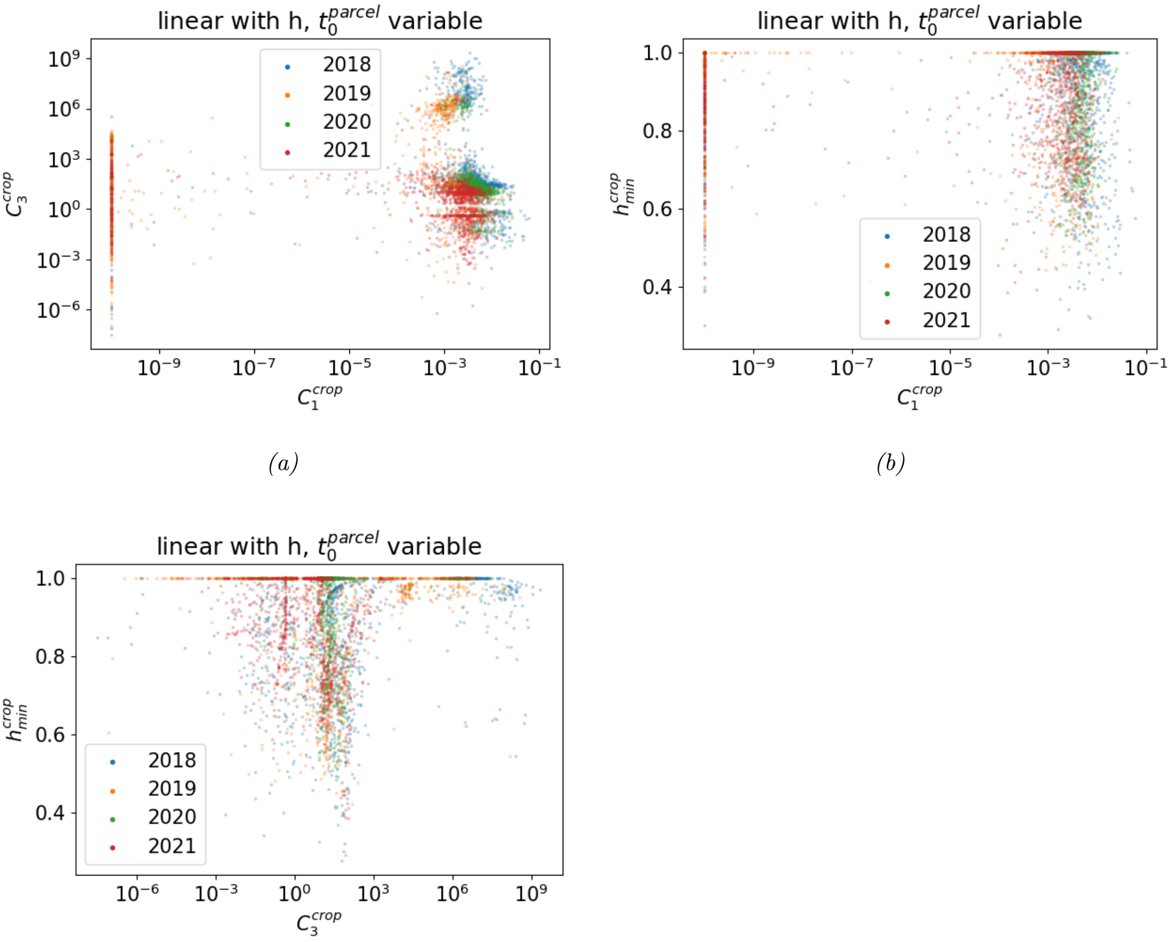

(a)

(b)

(c)

Figure 40: Scatter plots of all combinations of the three parameters C_1^{crop}, C_3^{crop} *and* h_{min}^{crop} *of the fit function defined by* p^{crop} *and* g *linear with* t_0^{parcel} *and* h_{min}^{crop} *variable and all other parameters fixed.*